Finite element simulation of an impinging liquid droplet on a hot solid substrate

Dissertation

zur Erlangung des akademischen Grades

doctor rerum naturalium
(Dr. rer. nat.)

von **M.Sc. Sangeetha Rajasekaran**
geb. am 01.12.1976 in Neyveli, India

genehmigt durch die Fakultät für Mathematik
der Otto-von-Guericke-Universität Magdeburg

Gutachter:
Prof. Dr. rer. nat. habil. Lutz Tobiska
Prof. Dr.-Ing. Jürgen Schmidt

Eingereicht am: 23.01.2014
Verteidigung am: 19.05.2014

Acknowledgements

I would like to thank my advisor, Professor Lutz Tobiska, for his invaluable guidance and continuous support, without his support and patience this thesis would not have been possible. Under his guidance I have also learnt much that will be of immense help to me in my future academic and professional life.

I am very thankful to Professor Jürgen Schmidt for his valuable suggestions and fruitful discussions on the modeling part of this research work. I also grateful to my colleagues at the department and at the Graduiertenkolleg for their help and fruitful discussions.

I would like to thank my family and friends for their encouragement and continuous support. This work has been financially supported by the German Research Foundation (DFG) through the Graduiertenkolleg 1554, and is greatfully acknowledged.

Sangeetha Rajasekaran

Institute for Analysis and Numerical Mathematics
Faculty of Mathematics
Otto-von-Guericke-University
Magdeburg Germany

Abstract

The main focus of this work is to develop an accurate and robust numerical scheme for simulation of a non-isothermal liquid droplet impinging on a horizontal hot substrate. Apart from other challenges associated with the modeling of free boundary problems, the moving contact line, Marangoni convection, time dependent liquid–solid interface make the model more complicate. The fluid flow in the droplet is described by the time dependent incompressible Navier-Stokes equations, whereas the temperature in the droplet and in the solid substrate is described by the energy equation.

The arbitrary Lagrangian–Eulerian (ALE) method is used to track the moving free surface and to handle the time-dependent domain. In this sharp interface ALE approach, the computational mesh resolves the free surface and the liquid–solid interface. Thus, the jumps in the material properties are handled easily. Further, the approximation of the curvature and the inclusion of the surface force is straight forward. In particular, we included the contact angle at the moving contact line in the weak formulation of the model using the Laplace-Beltrami operator technique for the curvature term. Further, this technique allowed us to consider the curvature term semi implicitly.

The coupled time dependent incompressible Navier-Stokes equations and the energy equations are spatially discretized by finite elements, whereas the fractional step ϑ scheme is used for the temporal discretization. Since the computed velocities are used to move the free surface and interface points, high accuracy is required. Further, mass should be conserved and spurious velocities – if there are some – should be suppressed. Therefore, we use second–order inf–sup stable finite element approximations avoiding spurious pressure oscillations. Continuous pressure approximations often generate spurious velocities. In order to suppress them discontinuous pressure approximations are a good choice. But to guarantee the inf–sup stability for discontinuous, piecewise linear pressure approximations on arbitrary shape regular families of meshes we have to enrich the space of continuous, piecewise quadratic functions by cubic bubble functions. The good mass conservation properties are lying on the fact that up to the

first integral moments the divergence is element-wise vanishing. The temperature is approximated by the standard continuous, piecewise quadratic finite element.

In the considered droplet deformation problem, the free surface vertices adjacent to the moving contact line may reach the solid surface during the droplet spreading (rolling motion). Further, the vertices on the liquid–solid interface can move in the tangential direction due to the Navier-slip boundary condition. This leads to non-matching grid along the liquid–solid interface if the mesh in the solid domain is fixed. The liquid–solid interface can be handled by either a non-matching or a matching grid. An efficient algorithm is implemented to handle the rolling motion automatically. In this approach, the displacement of the solid domain also has to be calculated due to the movement of the vertices on the liquid–solid interface. Thus, the solid domain becomes time-dependent and the mesh velocity will be non-zero in solid phase which will induce the domain velocity convection term in the energy equation of the solid phase. Further, a special algorithm for calculating the heat flow from the solid phase into the liquid phase without differentiating the numerical solution is presented.

The computational cost is drastically reduced by restricting the problem to a 3D-axisymmetric model. The 3D-axisymmetric weak form in the 2D-meridian domain is generated directly from the weak form in 3D-Cartesian coordinates. Introducing cylindrical coordinates, the volume, surface and line integrals in 3D are transformed into area integrals, line integrals and a functional in the contact point. In this way the space dimension is reduced by one. Note that this approach leads naturally to boundary conditions along the 'artificial rotational axis' which are already partially included in the weak form.

Finally, an array of numerical experiments is presented to study the influence of different dimensionless (Reynolds, Weber, Peclet, and Biot) numbers on the flow dynamics and the heat transfer. In particular, the influence of these numbers on the wetting diameter, dynamics contact angle, maximum wetting diameter and heat flow are studied. Further, the maximum mass fluctuation in all computations is calculated, and is less than 1 %. This shows the accuracy of the proposed numerical scheme.

Zusammenfassung

Ziel der Arbeit ist die Entwicklung eines genauen und robusten numerischen Verfahrens zur Simulation eines auf eine horizontale heiße Unterlage auftreffenden nicht-isothermen Flüssigkeitstropfens. Neben den bekannten Herausforderungen, die mit der Modellierung freier Randwertprobleme verbunden sind, werden die Modelle durch die bewegte Kontaktlinie, die Marangoni Konvektion und das zeitabhängige, flüssig-feste Interface komplizierter. Die Füssigkeitsströmung im Tropfen wird durch die zeitabhängigen Navier-Stokes Gleichungen, die Temperatur im Tropfen und in der festen Unterlage durch die Energiegleichung beschrieben.

Die freiwählbare Langrange-Eulersche (ALE) Methode wird zur Verfolgung der sich bewegenden freien Oberfläche und zur Behandlung des zeitabhängigen Gebietes verwendet. Bei diesem scharfen Interface ALE Zugang werden die freie Oberfläche und das flüssig-feste Interface durch das numerische Gitter aufgelöst. Somit können Sprünge in den Materialeigenschaften leicht berücksichtigt werden. Ferner sind die Approximation der Krümmung und die Einbeziehung der Oberflächenkraft unkompliziert. Insbesondere berücksichtigen wir in der schwachen Formulierung des Models den Kontaktwinkel an der sich bewegenden Kontaktlinie unter Verwendung der Laplace-Beltrami Operator Technik für den Krümmungsterm. Diese Technik erlaubt uns den Krümmungsterm semi-implizit zu betrachten.

Die gekoppelten, zeitabhängigen, inkompressiblen Navier-Stokes Gleichungen und die Energiegleichung werden räumlich durch finite Elemente und zeitlich durch das Teilschritt θ Verfahren diskretisiert. Da die berechneten Geschwindigkeiten verwendet werden, um die freie Oberfläche und die Grenzflächenpunkte zu bewegen, ist eine hohe Genauigkeit erforderlich. Ferner sollten Masse erhalten und parasitäre Strömungen - sofern es sie gibt - unterdrückt werden. Daher verwenden wir inf-sup stabile Elemente zweiter Ordnung, die keine künstlichen Druckoszillationen erzeugen. Stetige Druckapproximationen erzeugen oft künstliche Geschwindigkeiten. Um diese zu unterdrücken sind unstetige Druckapproximationen eine gute Wahl. Um jedoch die inf-sup Stabilität für unstetige, stückweise lineare Druckapproximationen auf beliebigen shape-regulären Gittern zu garantieren,

müssen wir den Raum der stetigen, stückweise quadratischen Funktionen durch kubische Blasenfunktionen anreichern. Die gute Masseerhaltung liegt in der Tatsache begründet, dass die Integral-Momente der Divergenz elementwise bis zur ersten Ordnung verschwinden. Die Temperatur wird durch die üblichen stetigen, stückweise quadratischen finiten Elemente approximiert.

Im betrachteten Tropfendeformationsproblem, können die zur bewegten Kontaktlinie benachbarten Knoten der freien Oberfäche während der Tropfenausbreitung die feste Unterlage erreichen (rollende Bewegung). Darüber hinaus können sich die Knoten auf dem flüssig-festem Interface aufgrund der Navier-Gleitrandbedingung in tangentieller Richtung bewegen. Dies führt auf nicht-zusammenpassende Gitter entlang des flüssig-festem Interface wenn das Gitter im Gebiet der festen Unterlage sich nicht ändert. Das flüssig-feste Interface kann entweder durch ein nicht-zusammenpassendes oder durch ein passendes Gitter behandelt werden. Ein effizienter Algorithmus wurde implementiert, um die rollende Bewegung automatisch zu handhaben. Bei diesem Ansatz sind aufgrund der Bewegung der Knoten auf dem flüssig-festem Interface auch die Verschiebungen im Gebiet der festen Unterlage zu berechnen. Somit wird das feste Gebiet zeitabhängig und die Gittergeschwindigkeit in der festen Phase ist verschieden von Null, was einen konvektiven Gebietsgeschwindigkeitsterm in der Energiegleichung der festen Phase erzeugt. Darüber hinaus wird ein spezieller Algorithmus zur Berechnung des Wärmetransports von der festen in die flüssige Phase ohne Differentiation der numerischen Lösung vorgestellt.

Die Rechenkosten werden durch eine 3d-axialsymmetrische Betrachtungsweise drastisch reduziert. Die 3d-axialsymmetrische schwache Form im 2d Querschnittsgebiet wird direkt aus der schwachen Form in 3d-kartesischen Koordinaten erzeugt. Durch Einführung von Zylinderkoordinaten, werden die Volumen-, Flächen- und Linienintegrale in 3d in Flächenintegrale, Linienintegrale und einem Funktional im Kontaktpunkt transformiert. Auf diese Weise wird die Raumdimension um Eins erniedrigt. Es sei vermerkt, dass dieser Ansatz natürlich auf Randbedingungen entlang der 'künstlichen Rotationsachse' führt, die bereits in der schwachen Form enthalten sind.

Abschließend, werden die Ergebnisse numerischer Tests vorgestellt, um den Einfluss unterschiedlicher dimensionsloser Zahlen (Reynolds, Weber, Peclet und Biot) auf die Strömungsdynamik und den Wärmeübergang zu studieren. Insbesondere wird der Einfluss dieser Zahlen auf den Benetzungsdurchmesser, die Dynamik des Kontaktwinkels, den maximalen Durchmesser der Benetzung und den Wärmetransport untersucht. Ferner wird

in allen Rechnungen das Maximum der Massenfluktuation berechnet, das kleiner als 1% ist. Dies zeigt die Genauigkeit des vorgeschlagenen numerischen Schemas.

Contents

Nomenclature

d_o	initial diameter of the droplet
g	gravitational constant
I	given time
L	characteristic length
M_F	mass fluctuation
$M_{F_{max}}$	maximum mass fluctuation
p	pressure
q	pressure test function
Q_h	total heat
r	radial coordinate ($\sqrt{x^2+y^2}$)
r_0	initial radius of the bubble/droplet
t	time
T	temperature
U	characteristic velocity
$W_{d_{max}}$	maximum wetting diameter

$\mathbf{u}$	liquid velocity vector
$\mathbf{v}$	vector test function
$\mathbf{w}$	domain velocity vector
$\mathbb{D}(\mathbf{u})$	velocity deformation tensor
$\mathbb{S}(\mathbf{u}, p)$	dimensionless stress tensor
$\mathbb{T}(\mathbf{u}, p)$	stress tensor
$\boldsymbol{\nu}$, $\boldsymbol{n}$	normal vector
$\boldsymbol{\tau}$	tangential vector

Bi	Biot number
Ca	capillary number
Fr	Froude number
Pe	Peclet number
Re	Reynolds number
We	Weber number
β_ϵ	slip number
θ	contact angle
ρ	density
μ	dynamics viscosity
$\mathcal{K}$	sum of the principle curvatures
σ	surface tension of the liquid
$\mathcal{A}$	ALE mapping
Ω	computational domain
Φ	meridian domain

1 Introduction

The understanding of the mechanisms involved in the cooling or temperature regulation of solid objects using sprays are of fundamental importance in a wide variety of industrial, medical and environmental applications such as ink-jet printing and thin film coating [54], micro/nano material fabrication [18, 74], microelectronics [29, 46], DNA/RNA micro-arrays deposition [64, 13], functioning of biological organisms [37], space studies [80], etc. In particular, spray cooling with water is one of the most effective cooling processes [46, 79].

Modeling of the heat transfer mechanism involved in the process of a liquid droplet impinging on a hot solid surface is very challenging, even for a clean impinging droplet on a smooth (atomically) flat surface. Tracking/capturing the moving free boundary/interface[36], incorporating the dynamic contact angle [23], handling the moving contact line [27], accurate curvature approximation [5, 24], precise inclusion of the Marangoni and surface forces [28], and handling the jumps in the material parameters are the main challenges in simulation of these processes. As a droplet nears a hot solid surface, heat is transferred from the solid to the liquid phase by conduction, convection and radiation. This energy is used to increase the temperature of the liquid or to vaporize the liquid from the base of the droplet. In the latter case a vapor layer will be nucleated between the solid and the liquid phase (Leidenfrost phenomenon). For a surface temperature below the Leidenfrost temperature we suppose that the direct liquid-wall contact and the kinetic of the droplet spreading dominate the heat transfer. Despite several advances made in the field of Computational Fluid Dynamics, modeling and simulation of these processes are still very challenging.

The aim of this research work is to develop an accurate and robust numerical model for studying the dynamics of a single non-isothermal liquid droplet impinging on a hot solid substrate with the intention of enhancing the spray cooling models later. In particular, we consider the heat transfer process in a single droplet during the spreading and recoiling from the moment of its impact till losing a direct contact with the solid, which is

below the Leidenfrost temperature.

Droplet impinging on a hot surface

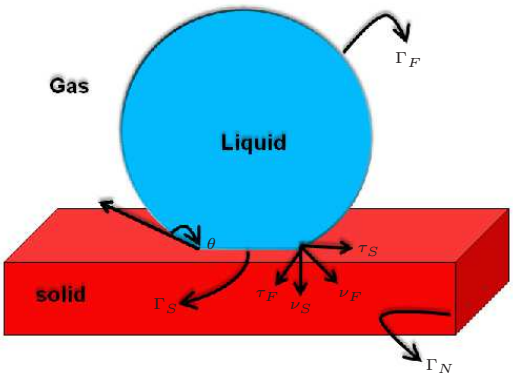

Figure 1.1: Impinging droplet on a hot solid surface.

We are interested in modeling of a single droplet impinging perpendicularly and spreading on a horizontal hot solid substrate. The main focus of this work is to develop an accurate and robust sharp interface numerical scheme to simulate this entire process. Since the fluid flow is mainly driven by the surface energy (especially at the later stage of droplet deformation), the moving boundary has to be tracked accurately in order to approximate the curvature and to incorporate the Marangoni effects precisely. Therefore, a sharp interface tracking approach will be used to track the free surface. Further, appropriate numerical methods have to be used to avoid spurious velocities. In our study, we assume that the material properties of the liquid phase and the solid phase are constants and independent of temperature in respective phases. Further, we assume that the temperature of the solid phase is less than the Leidenfrost temperature.

The fluid flow will be described by the time dependent incompressible Navier–Stokes equations. The heat transport from the solid substrate into the liquid droplet and the temperature distribution in both phases are modeled by the energy equation in liquid and solid phases. The main challenge in solving the energy equation is to incorporate the continuity condition on the liquid-solid interface. We handle it by rewriting the energy equations in both phases into one field formulation. Further, the considered model impinging droplet is axisymmetric, we rewrite the model equations

into 3D-axisymmetric form. This allows to reduce the computational cost considerably.

Dynamic contact angle

The contact angle (θ) in the impinging droplet determines the wetting behavior of the liquid droplet on a given solid substrate. For instance, the wetting of a water droplet on the glass surface is more than the wetting of the same droplet on the wax surface. Since the only parameter that determines this phenomenon is the contact angle, it has to be incorporate into the model precisely. Further, the surface roughness (if exists) can be accounted through the contact angle. The inclusion of the contact angle in simulations has derived the attention of lots of researchers that results in numerous publications. Dynamic contact angle, advancing contact angle, receding contact angle, equilibrium contact angle are the variants that have been discussed in the literature. Recently, it is has been shown that the equilibrium contact angle is the preferred one for the sharp interface methods [23]. In our model, we use the equilibrium contact angle.

Moving contact line

The use of the classical no-slip boundary condition on the liquid-solid interface of the considered problem induce the non-integrable singularity at the moving contact line, where the liquid, solid and gas phases intersect [41, 68, 77]. Several types of boundary conditions have been proposed in the literature, for example, free slip, stick-slip, partially slip, etc. However, the slip with friction (Navier-slip) boundary condition has been widely accepted to avoid the non-integrable singularity at the moving contact line. The Navier-slip boundary condition has also been used for high speed flows, see for example, [44]. The main challenge in using the Navier-slip boundary condition is the choice of the slip coefficient.

Marangoni Convection

One of the main process in the non-isothermal liquid droplet impinging simulations is the Marangoni convection. The changes in the local surface temperature T_F along the free surface induce variations in the surface tension, and thus the fluid moves away from the region of low surface tension to the region of high surface tension. This effect is called Marangoni convection. Since the flow is mainly driven by the surface force, Marangoni

phenomenon has to be incorporated into the model very accurately. In our model, we assume that the temperature-dependent surface tension $\sigma(T_F)$ follows a simple linear law

$$\sigma(T_F) = \sigma_{ref} - \mathcal{C}_1(T_F - T_{ref})$$

where T_{ref} is some reference temperature, σ_{ref} is the surface tension coefficient at the reference temperature and $\mathcal{C}_1 > 0$ is the negative rate of change of surface tension with temperature.

Moving free surface and interface

The Volume-of-Fluid [40, 59, 61, 62, 78], Level set [35, 53, 65, 71, 72], Immersed Boundary/Front Tracking [56, 57, 66, 73, 76] and the arbitrary Lagrangian Eulerian [12, 25, 26, 39, 52, 51] technique are the most commonly used methods for tracking/capturing the moving interfaces/boundaries. Each of these methods has its own advantages and disadvantages. Although several interface capturing/tracking methods have been proposed in the literature, only a few numerical studies are related to the analysis of the thermodynamic behavior. In the early study [21], MAC-type solution technique has been used for the computations of a water droplet impinging on a flat surface above the Leidenfrost temperature. However, the unsteady heat transfer computation has been neglected. A considerable number of numerical studies using the Volume-of-Fluid method have been reported in the literature for droplets impinging on a hot surface [6, 31, 38, 55, 60, 69, 70]. Also, numerical studies using the Level set method [81, 82] and the Immersed Boundary method [19, 20] have been reported in the literature. All these methods can be classified as fixed grid (Eulerian) methods. Computations using the Lagrangian approach for a liquid droplet impinging on a hot solid substrate have been presented in [83].

In this work, the arbitrary Lagrangian Eulerian (ALE) approach that avoids the fast mesh distortion is used. The ALE approach, is quite popular in fluid structure interaction problems. Since the free surface/interface is resolved by the mesh, the surface force and the different material properties in different (liquid and solid) phases can be incorporated very accurately in the proposed scheme. Further, the Laplace-Beltrami operator technique for approximating the local curvature which avoids the explicit computation of the curvature is used.

The heat transfer in the moving droplet and in the fixed solid surface is described by the energy equation. Here we study the heat transfer in the

droplet and the influence of the heat transfer on the fluid flow. Here we illustrate that the numerical scheme captures the behaviour of heat transfer effects on the flow dynamics. In our model, the surface tension is considered as a function of temperature. We assume that the density, viscosity and thermal conductivity are constants in the liquid. Furthermore, the basic assumption of our model is that the density, viscosity and the thermal conductivity in the gas phase are negligible compared with the liquid phase. Further the Marangoni convection is included in the model. In this initial study, the temperature of the solid surface is assumed to be well below the boiling point temperature, and thus the Leidenfrost effect does not occur. The temperature control on spreading by creating counteract flows that slow down the spreading.

Structure of the thesis

The mathematical model for the considered model problem is described in Chapter 2. Further, the variational formulation of the governing equations are derived in this Chapter. In particular, a one field formulation for the energy equation in the liquid and solid phases is derived. Also, the arbitrary Lagrangian–Eulerian approach for the free surface tracking is presented in Chapter 2.

The spatial and temporal discretizations of the considered partial differential equations are provided in Chapter 3. A detailed description of the finite element method and its application to the incompressible Navier–Stokes equations are given in this Chapter. Also, the 3D-axisymmetric form is derived for the variational form of the considered equations.

In Chapter 4, the numerical methods to handle moving meshes, in particular, the mesh handling at the liquid–solid interface are explained. Further, an efficient and accurate scheme for calculating the heat flux across the liquid–solid interface is provided in this Chapter.

Finally, an array of numerical experiments to study the influence of different dimensionless numbers are presented in Chapter 5. After that a summary of this research is presented at the end of the thesis.

2 Modeling of an impinging droplet on a hot surface

A mathematical model for an impinging droplet on a horizontal hot surface is presented in this chapter. The model consists of a system of coupled time-dependent Navier–Stokes and energy equations in a time dependent domain. The fluid flow in the droplet is described by the Navier–Stokes equations, whereas the heat transfer in the moving droplet and in the fixed solid surface is described by the energy equation. We first derive the corresponding variational forms of the coupled Navier-Stokes and energy equations in a dimensionless form. Then, the Arbitrary Lagrangian Eulerian (ALE) approach to handle time-dependent domains is presented for the considered problem. After that the Laplace–Beltrami operator technique to approximate the curvature in the force balancing condition on the free surface is presented. Further, the inclusion of the contact angle at the moving contact line, where the free surface and the liquid-solid interface intersect, is described.

2.1 Governing equations

2.1.1 Fluid flow in the droplet

In this study we assume that the fluid is incompressible and the material properties such as the density and viscosity are constant in the liquid phase. The governing equations for the fluid flow describing the sequence of spreading and recoiling of an impinging droplet in the given time interval (0, I) are the time dependent incompressible Navier–Stokes equations

$$\begin{aligned} \frac{\partial \mathbf{u}}{\partial t} + (\mathbf{u}\cdot\nabla)\mathbf{u} - \frac{1}{\rho}\nabla\cdot(\mathbb{T}(\mathbf{u},p)) &= g\mathbf{e} \quad \text{in} \quad \Omega_F(t)\times(0,\mathrm{I}), \\ \nabla\cdot\mathbf{u} &= 0 \quad \text{in} \quad \Omega_F(t)\times(0,\mathrm{I}), \\ \mathbf{u}(.,0) &= \mathbf{u}_0 \quad \text{in} \quad \Omega_F(0), \end{aligned} \tag{2.1}$$

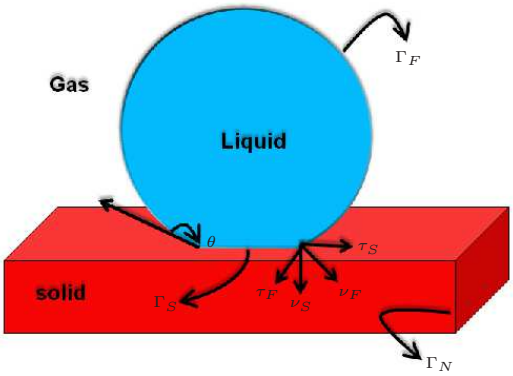

Figure 2.1: Computational model for an impinging droplet on a hot solid surface.

with the boundary conditions given below. The time-dependent domain of the deforming droplet is denoted by $\Omega_F(t)$. The boundary of the droplet $\partial\Omega_F = \Gamma_F(t) \cup \Gamma_S(t)$, where $\Gamma_F(t)$ and $\Gamma_S(t)$ are the free surface and liquid-solid interface of the droplet, respectively. Here,

$$\Omega_F(t) \times (0, \mathrm{I}) = \{(x,t) \in \mathbb{R}^3 \times \mathbb{R} : x \in \Omega_F(t), t \in (0, \mathrm{I})\}.$$

Similarly, we write $\Gamma_F(t) \times (0, \mathrm{I}) = \{(x,t) \in \mathbb{R}^3 \times \mathbb{R} : x \in \Gamma_F(t), t \in (0, \mathrm{I})\}$. Further, $\mathbf{u}$ is the velocity, p is the pressure, ρ is the density, g is the gravitational constant, t is the time, $\mathbf{e}$ is an unit vector in the opposite direction of the gravitational force and $\mathbf{u}_0$ is a given initial velocity. The stress tensor $\mathbb{T}(\mathbf{u}, p)$ for a Newtonian incompressible fluid is given by

$$\mathbb{T}(\mathbf{u}, p) := 2\mu\mathbb{D}(u) - p\mathbb{I}, \quad \mathbb{D}(u)_{i,j} = \frac{1}{2}\left(\frac{\partial u_i}{\partial x_j} + \frac{\partial u_j}{\partial x_i}\right), \quad i, j = 1, ..., 3,$$

where μ denotes the dynamic viscosity, $\mathbb{D}(u)$ the velocity deformation tensor and $\mathbb{I}$ is the identity tensor. The kinematic and force balancing conditions on the free surface are given by

$$\begin{aligned} \mathbf{u} \cdot \boldsymbol{\nu}_F &= \mathbf{w} \cdot \boldsymbol{\nu}_F && \text{on} \quad \Gamma_F(t) \times (0, \mathrm{I}), \\ \boldsymbol{\nu}_F \cdot \mathbb{T}(\mathbf{u}, p) \cdot \boldsymbol{\nu}_F &= \sigma(T_F)\mathcal{K} && \text{on} \quad \Gamma_F(t) \times (0, \mathrm{I}), \\ \boldsymbol{\tau}_{i,F} \cdot \mathbb{T}(\mathbf{u}, p) \cdot \boldsymbol{\nu}_F &= \boldsymbol{\tau}_{i,F} \cdot \nabla\sigma(T_F) && \text{on} \quad \Gamma_F(t) \times (0, \mathrm{I}). \end{aligned}$$

Here, $\boldsymbol{\nu}_F$ and $\boldsymbol{\tau}_{i,F}$, i=1,2 denote the unit outward normal and tangential vectors on the free surface, $\mathbf{w}$ is the velocity of the computational domain $\Omega_F(t)$, T_F is the temperature on $\Gamma_F(t)$. Further, for simplicity we assume

that the surface tension $\sigma(T_F)$ to be given by a simple linear law

$$\sigma(T_F) = \sigma_{ref} - \mathcal{C}_1(T_F - T_{ref}) \tag{2.2}$$

where T_{ref} is the reference temperature, σ_{ref} is the surface tension coefficient at the reference temperature and $\mathcal{C}_1 > 0$ is the negative of rate of change of surface tension with temperature. The changes in the local surface temperature T_F on the free surface induce variations in the surface tension. Due to these variations in the surface tension, the fluid moves away from the region of low surface tension to the region of high surface tension. This effect is called Marangoni convection. Note that for a large T_F the surface tension would become negative. In order to avoid this unphysical behavior in the numerical tests we check whether the computed surface tension values are in the range of validity of the law (2.2).

Next, the conventional no-slip boundary condition cannot be use on the solid surface for moving contact line problems. Imposing the no-slip boundary condition at the moving contact line, where the free surface and the liquid-solid interface meet, leads to an non-integrable force singularity at the contact line [2, 17, 41, 42]. Therefore, we use the Navier-slip boundary condition [9, 27, 45, 77],

$$\begin{aligned} \mathbf{u} \cdot \boldsymbol{\nu}_S &= 0 \qquad \text{on} \quad \Gamma_S(t) \times (0, \mathrm{I}), \\ \mathbf{u} \cdot \boldsymbol{\tau}_{i,S} + \epsilon_\mu(\boldsymbol{\tau}_{i,S} \cdot \mathbb{T}(\mathbf{u}, p) \cdot \boldsymbol{\nu}_S) &= 0 \qquad \text{on} \quad \Gamma_S(t) \times (0, \mathrm{I}). \end{aligned}$$

Here, $\boldsymbol{\nu}_S$ and $\boldsymbol{\tau}_{i,S}$, i=1,2 denote the outward unit normal and tangential vectors on the liquid-solid interface. Further, ϵ_μ is the slip coefficient [27, 47].

2.1.2 Heat transfer in the liquid and solid phases

The heat transfer in the moving droplet and in the fixed solid surface is described by the energy equation. In this study, we assume that the material properties such as the densities, thermal conductivities and specific heats are constant in the liquid and solid phases, respectively. The solid phase is denoted by Ω_S and their Neuman boundary part $\Gamma_N(t) := \partial\Omega_S \setminus \Gamma_S(t)$. Note that, $\Gamma_N(t)$ becomes time-dependent due to $\Gamma_F(t)$ even though the solid phase Ω_S is fixed.
The heat transfer in the liquid phase is described by the energy equation

$$\frac{\partial T_F}{\partial t} + \mathbf{u} \cdot \nabla T_F = \frac{\lambda_F}{c_p^F \rho} \Delta T_F \qquad \text{in} \quad \Omega_F(t) \times (0, \mathrm{I}), \tag{2.3}$$

with the initial condition

$$T_F(x,0) = T_{F,0} \qquad \text{in} \quad \Omega_F(0).$$

Here, λ_F is the thermal conductivity in $\Omega_F(t)$, ρ is the density of the fluid and c_p^F is the specific heat of the fluid.
The governing equation for the heat transfer in the solid phase is given by

$$\frac{\partial T_S}{\partial t} = \frac{\lambda_S}{c_p^s \rho_s} \Delta T_S \qquad \text{in} \quad \Omega_S \times (0, \mathrm{I}), \tag{2.4}$$

with the initial condition

$$T_S(x,0) = T_{S,0} \qquad \text{in} \quad \Omega_S(0).$$

Here, T_S is the temperature in $\Omega_S(t)$, ρ_s and c_p^s denote the temperature, density and the specific heat of the solid respectively. The boundary condition for the temperature on the free surface is given by

$$-\lambda_F \frac{\partial T_F}{\partial \boldsymbol{\nu}_F} = \alpha_F (T_F - T_\infty) \quad \text{on} \quad \Gamma_F(t) \times (0, \mathrm{I}),$$

where, T_∞ is the temperature of the surrounding gas, α_F is the convection heat transfer coefficient on the liquid-gas interface. On the liquid-solid interface the temperature and the heat flux are assumed to be continuous, and we impose the following transition conditions

$$\begin{aligned} \lambda_F \frac{\partial T_F}{\partial \boldsymbol{\nu}_F} &= -\lambda_S \frac{\partial T_S}{\partial \boldsymbol{\nu}_S} \qquad \text{on} \quad \Gamma_S(t) \times (0, \mathrm{I}), \\ T_F &= T_S \qquad \text{on} \quad \Gamma_S(t) \times (0, \mathrm{I}). \end{aligned}$$

Finally on $\Gamma_N(t)$, we impose the adiabatic boundary condition

$$\lambda_S \frac{\partial T_S}{\partial n} = 0 \quad \text{on} \quad \Gamma_N(t) \times (0, \mathrm{I}),$$

that is, no heat flux on the boundary $\Gamma_N(t)$. Here, n is the outward normal on $\Gamma_N(t)$.

2.2 Variational form

2.2.1 Dimensionless form of the Navier-Stokes equations

In this section we derive the dimensionless variational form of the Navier-Stokes equations. We introduce the scaling factors L and U as characteristic

length and velocity, respectively. Furthermore, we define the dimensionless variables as

$$\tilde{x} = \frac{x}{L}, \quad \tilde{\mathbf{u}} = \frac{\mathbf{u}}{U}, \quad \tilde{\mathbf{w}} = \frac{\mathbf{w}}{U}, \quad \tilde{t} = \frac{tU}{L},$$
$$\tilde{I} = \frac{IU}{L}, \quad \tilde{p} = \frac{p}{\rho U^2}, \quad \tilde{T_F} = \frac{T_F - T_\infty}{T_{ref} - T_\infty},$$

and the dimensionless numbers (Reynolds, Weber, Froude and slip, respectively) are defined by

$$Re = \frac{\rho U L}{\mu}, \quad We = \frac{\rho U^2 L}{\sigma_{ref}}, \quad Fr = \frac{U^2}{Lg}, \quad \beta_\epsilon = \epsilon_\mu \rho_s U.$$

Using these dimensionless variables in the stress tensor $\mathbb{T}(\mathbf{u}, p)$, we introduce a dimensionless stress tensor $\mathbb{S}(\mathbf{u}, p)$ such that

$$\begin{aligned}
\mathbb{T}(u,p) &= \frac{2\mu U}{L}\mathbb{D}(\tilde{\mathbf{u}}) - \rho U^2 \tilde{p}\mathbb{I} \\
&= \rho U^2 \left(\frac{2\mu}{\rho U L}\mathbb{D}(\tilde{\mathbf{u}}) - \tilde{p}\mathbb{I} \right) \\
&= \rho U^2 \left(\frac{2}{Re}\mathbb{D}(\tilde{\mathbf{u}}) - \tilde{p}\mathbb{I} \right) \\
&= \rho U^2 \mathbb{S}(\tilde{\mathbf{u}}, \tilde{p}).
\end{aligned}$$

Using the same variable transformation in equation (2.1), we get

$$\frac{U^2}{L}\frac{\partial \tilde{\mathbf{u}}}{\partial \tilde{t}} + \frac{U^2}{L}(\tilde{\mathbf{u}} \cdot \nabla)\tilde{\mathbf{u}} - \frac{\rho U^2}{\rho L}\nabla \cdot \mathbb{S}(\tilde{\mathbf{u}}, \tilde{p}) = g\mathbf{e}.$$

Multiplying this equation by L/U^2 and omitting the tilde afterwards, we obtain the dimensionless form of the Navier-Stokes equations as

$$\begin{aligned}
\frac{\partial \mathbf{u}}{\partial t} + (\mathbf{u} \cdot \nabla)\mathbf{u} - \nabla \cdot \mathbb{S}(\mathbf{u}, p) &= \frac{1}{Fr}\mathbf{e} \quad \text{in} \quad \Omega_F(t) \times (0, \mathrm{I}), \\
\nabla \cdot \mathbf{u} &= 0 \qquad \text{in} \quad \Omega_F(t) \times (0, \mathrm{I}).
\end{aligned} \tag{2.5}$$

The boundary conditions are also transformed into a dimensionless form:

$$\begin{aligned}
\mathbf{u} \cdot \boldsymbol{\nu}_F &= \mathbf{w} \cdot \boldsymbol{\nu}_F \quad \text{on} \quad \Gamma_F(t) \times (0, \mathrm{I}), \\
\mathbf{u} \cdot \boldsymbol{\nu}_S &= 0 \qquad \text{on} \quad \Gamma_S(t) \times (0, \mathrm{I}), \\
\mathbf{u} \cdot \boldsymbol{\tau}_{i,S} + \beta_\epsilon(\boldsymbol{\tau}_{i,S} \cdot \mathbb{S}(\mathbf{u}, p) \cdot \boldsymbol{\nu}_S) &= 0 \qquad \text{on} \quad \Gamma_S(t) \times (0, \mathrm{I}),
\end{aligned}$$

for i=1,2. Rewriting the fluid's normal stress boundary condition on the free surface into a dimensionless form, we get

$$\boldsymbol{\nu}_F \cdot \mathbb{S}(\tilde{\mathbf{u}}, \tilde{p}) \cdot \boldsymbol{\nu}_F = \frac{1}{\rho U^2 L} \left(\sigma_{ref} - \frac{\tilde{\mathcal{C}}_1}{T_{ref} - T_\infty} ((T_{ref} - T_\infty)\tilde{T_F} + T_\infty - T_{ref}) \right) \mathcal{K}.$$

Note that the relation $\mathcal{C}_1 = \dfrac{\partial \sigma}{\partial T}$ has been used. Omitting the tilde we get,

$$\boldsymbol{\nu}_F \cdot \mathbb{S}(u, p) \cdot \boldsymbol{\nu}_F = \frac{1}{We} \left(1 - \frac{\mathcal{C}_1}{\sigma_{ref}} (T_F - 1) \right) \mathcal{K} \qquad \text{on} \quad \Gamma_F(t) \times (0, \mathrm{I}). \tag{2.6}$$

Here, We is the Weber number with the surface tension coefficient σ_{ref}. Similarly, rewriting the fluid's shear stress boundary condition on the free surface into a dimensionless form, we get

$$\boldsymbol{\tau}_{i,F} \cdot \mathbb{S}(\tilde{\mathbf{u}}, \tilde{p}) \cdot \boldsymbol{\nu}_F = -\frac{\tilde{\mathcal{C}}_1}{\rho U^2 L} \boldsymbol{\tau}_{i,F} \cdot \nabla \tilde{T_F}.$$

Omitting the tilde we get,

$$\boldsymbol{\tau}_{i,F} \cdot \mathbb{S}(u, p) \cdot \boldsymbol{\nu}_F = -\frac{\mathcal{C}_1}{\sigma_{ref} We} \boldsymbol{\tau}_{i,F} \cdot \nabla T_F \quad \text{on} \quad \Gamma_F(t) \times (0, \mathrm{I}).$$

2.2.2 Weak form of the Navier–Stokes equations

Let Ω be an bounded open subset in $\mathbb{R}^3$. Further $L^2(\Omega)$ consists of all functions f which are squared integrable over Ω in the sense of Lebesque. The inner product and the norm in $L^2(\Omega)$ are defined as

$$(f, g) = \int_\Omega f g \, dx, \quad \|g\| = \left(\int_\Omega g^2 \, dx \right)^{1/2} \qquad \forall \; f, g \in L^2(\Omega).$$

Next, we introduce the Sobolev space

$$H^1(\Omega) = \left\{ g \in L^2(\Omega) : \nabla g \in L^2(\Omega)^3 \right\}.$$

We now derive the weak form of the dimensionless equation (2.5). Let $H^1(\Omega_F(t))$ be the usual Sobolev space. We define $Q = L^2(\Omega_F(t))$ as a

pressure space and

$$V := \{\mathbf{v} \in H^1(\Omega_F(t))^3 : \mathbf{v} \cdot \boldsymbol{\nu}_S = 0 \quad \text{on} \quad \Gamma_S(t)\} \tag{2.7}$$

as a velocity space for (2.5). As a consequence the no penetration boundary condition $\mathbf{u} \cdot \boldsymbol{\nu}_S = 0$ on liquid-solid interface $\Gamma_S(t)$ will be satisfied in both the ansatz and test spaces. We now multiply the momentum and mass balance equations (2.5) by test functions $\mathbf{v} \in V$ and $q \in Q$ respectively, and integrate over $\Omega_F(t)$. By applying the Gaussian theorem for the stress tensor, we get

$$\begin{aligned}
&-\int_{\Omega_F} \nabla \cdot \mathbb{S}(\mathbf{u}, p) \cdot \mathbf{v} \; dx \\
&= \int_{\Omega_F} \mathbb{S}(\mathbf{u}, p) : \nabla \mathbf{v} \; dx - \int_{\partial\Omega_F} \mathbf{v} \cdot \mathbb{S}(\mathbf{u}, p) \cdot \boldsymbol{\nu} \; d\gamma \\
&= \int_{\Omega_F} \frac{1}{2}\mathbb{S}(\mathbf{u}, p) : \nabla \mathbf{v} \; dx + \int_{\Omega_F} \frac{1}{2}\mathbb{S}^T(\mathbf{u}, p) : \nabla \mathbf{v} \; dx - \int_{\partial\Omega_F} \mathbf{v} \cdot \mathbb{S}(\mathbf{u}, p) \cdot \boldsymbol{\nu} \; d\gamma \\
&= \int_{\Omega_F} \mathbb{S}(\mathbf{u}, p) : \mathbb{D}(\mathbf{v}) \; dx - \int_{\partial\Omega_F} \mathbf{v} \cdot \mathbb{S}(\mathbf{u}, p) \cdot \boldsymbol{\nu} \; d\gamma \\
&= \frac{2}{Re} \int_{\Omega_F} \mathbb{D}(\mathbf{u}) : \mathbb{D}(\mathbf{v}) \; dx - \int_{\Omega_F} p \nabla \cdot \mathbf{v} \; dx - \int_{\partial\Omega_F} \mathbf{v} \cdot \mathbb{S}(\mathbf{u}, p) \cdot \boldsymbol{\nu} \; d\gamma.
\end{aligned}$$

To include the free surface and liquid-solid boundary conditions in the weak form, we split the boundary integral term as an integral over Γ_S and over Γ_F

$$-\int_{\partial\Omega_F} \mathbf{v} \cdot \mathbb{S}(\mathbf{u}, p) \cdot \boldsymbol{\nu} \; d\gamma = -\int_{\Gamma_S} \mathbf{v} \cdot \mathbb{S}(\mathbf{u}, p) \cdot \boldsymbol{\nu}_S \; d\gamma_S - \int_{\Gamma_F} \mathbf{v} \cdot \mathbb{S}(\mathbf{u}, p) \cdot \boldsymbol{\nu}_F \; d\gamma_F. \tag{2.8}$$

Using the orthonormal decomposition, we split the test function $\mathbf{v}$ in the liquid-solid integral part of equation (2.8) as

$$\mathbf{v} = (\mathbf{v} \cdot \boldsymbol{\nu}_S)\boldsymbol{\nu}_S + \sum_{i=1}^{2} (\mathbf{v} \cdot \boldsymbol{\tau}_{i,S})\boldsymbol{\tau}_{i,S}.$$

Then, using the definition (2.7) and the slip with friction boundary condition, the liquid-solid integral term can be written as

$$
\begin{aligned}
&- \int_{\Gamma_S} \mathbf{v} \cdot \mathbb{S}(\mathbf{u}, p) \cdot \boldsymbol{\nu}_S \, d\gamma_S \\
&\qquad = - \int_{\Gamma_S} \sum_{i=1}^{2} (\mathbf{v} \cdot \boldsymbol{\tau}_{i,S}) \boldsymbol{\tau}_{i,S} \cdot \mathbb{S}(\mathbf{u}, p) \cdot \boldsymbol{\nu}_S \, d\gamma_S \\
&\qquad\qquad - \int_{\Gamma_S} (\mathbf{v} \cdot \boldsymbol{\nu}_S) \cdot \boldsymbol{\nu}_S \cdot \mathbb{S}(\mathbf{u}, p) \cdot \boldsymbol{\nu}_S \, d\gamma_S \\
&\qquad = \frac{1}{\beta_\epsilon} \int_{\Gamma_S} \sum_{i=1}^{2} (\mathbf{u} \cdot \boldsymbol{\tau}_{i,S})(\mathbf{v} \cdot \boldsymbol{\tau}_{i,S}) \, d\gamma_S. \qquad (2.9)
\end{aligned}
$$

Since we impose the no penetration condition in the definition of the space (2.7), the normal stress integral term vanishes in the above equation. Similarly, we split the test function $\mathbf{v}$ in the liquid-gas term of the equation (2.8) and using corresponding boundary conditions, we get

$$
\begin{aligned}
&- \int_{\Gamma_F} \mathbf{v} \cdot \mathbb{S}(\mathbf{u}, p) \cdot \boldsymbol{\nu}_F \, d\gamma_F \\
&\qquad = - \int_{\Gamma_F} \sum_{i=1}^{2} (\mathbf{v} \cdot \boldsymbol{\tau}_{i,F}) \boldsymbol{\tau}_{i,F} \cdot \mathbb{S}(\mathbf{u}, p) \cdot \boldsymbol{\nu}_F \, d\gamma_F \\
&\qquad\qquad - \int_{\Gamma_F} (\mathbf{v} \cdot \boldsymbol{\nu}_F) \cdot \boldsymbol{\nu}_F \cdot \mathbb{S}(\mathbf{u}, p) \cdot \boldsymbol{\nu}_F \, d\gamma_F \\
&\qquad = \frac{\mathcal{C}_1}{\sigma_{ref} We} \int_{\Gamma_F} \sum_{i=1}^{2} (\mathbf{v} \cdot \boldsymbol{\tau}_{i,F})(\boldsymbol{\tau}_{i,F} \cdot \nabla T_F) \, d\gamma_F \\
&\qquad\qquad - \frac{1}{We} \int_{\Gamma_F} \left(1 - \frac{\mathcal{C}_1}{\sigma_{ref}} (T_F - 1)\right) (\mathbf{v} \cdot \boldsymbol{\nu}_F) \, \mathcal{K} \, d\gamma_F \\
&\qquad = \frac{\mathcal{C}_1}{\sigma_{ref} We} \int_{\Gamma_F} \sum_{i=1}^{2} (\mathbf{v} \cdot \boldsymbol{\tau}_{i,F})(\boldsymbol{\tau}_{i,F} \cdot \nabla T_F) \, d\gamma_F \\
&\qquad\qquad - \frac{1}{We} \int_{\Gamma_F} M_{T_F} (\mathbf{v} \cdot \boldsymbol{\nu}_F) \, \mathcal{K} \, d\gamma_F, \qquad (2.10)
\end{aligned}
$$

where $M_{T_F} = \left(1 - \frac{\mathcal{C}_1}{\sigma_{ref}} (T_F - 1)\right)$. Using the derivations (2.9) and (2.10), the weak form of the Navier-Stokes equation (2.5) with boundary condition reads:

For given $\mathbf{u}(0)$, find $(\mathbf{u}, p) \in V \times Q$ such that

$$\left(\frac{\partial \mathbf{u}}{\partial t}, \mathbf{v}\right)_{\Omega_F} + a(\mathbf{u}; \mathbf{u}, \mathbf{v}) - b(p, \mathbf{v}) + b(q, \mathbf{u}) = f(\mathcal{K}, \mathbf{v}),$$

for all $\mathbf{v} \in V$ and $q \in Q$. Here, the subscript Ω_F in $\left(\frac{\partial \mathbf{u}}{\partial t}, \mathbf{v}\right)_{\Omega_F}$ denotes that the inner product is taken in $L^2(\Omega_F)$. The forms a, b and f are given by

$$\begin{aligned} a(\hat{\mathbf{u}}; \mathbf{u}, \mathbf{v}) &= \frac{2}{Re}\int_{\Omega_F} \mathbb{D}(\mathbf{u}) : \mathbb{D}(\mathbf{v})\ dx + \int_{\Omega_F} (\hat{\mathbf{u}} \cdot \nabla)\mathbf{u} \cdot \mathbf{v}\ dx, \\ &\quad + \frac{1}{\beta_\epsilon}\int_{\Gamma_S} (\mathbf{u} \cdot \boldsymbol{\tau}_{i,S})(\mathbf{v} \cdot \boldsymbol{\tau}_{i,S})\ d\gamma_S, \\ b(q, \mathbf{v}) &= \int_{\Omega_F} q \nabla \cdot \mathbf{v}\ dx, \\ f(\mathcal{K}, \mathbf{v}) &= \frac{1}{Fr}\int_{\Omega_F} \mathbf{e} \cdot \mathbf{v}\ dx - \frac{1}{We}\int_{\Gamma_F} M_{T_F}(\mathbf{v} \cdot \boldsymbol{\nu}_F)\ \mathcal{K}\ d\gamma_F \\ &\quad - \frac{\mathcal{C}_1}{\sigma_{ref} We}\int_{\Gamma_F} (\mathbf{v} \cdot \boldsymbol{\tau}_{i,F})(\boldsymbol{\tau}_{i,F} \cdot \nabla T_F)\ d\gamma_F. \end{aligned} \tag{2.11}$$

2.2.3 Dimensionless form of the energy equations

To write the energy equations in dimensionless form, we define the dimensionless temperature in the solid phase as

$$\tilde{T_S} = \frac{T_S - T_\infty}{T_{ref} - T_\infty}.$$

Using the dimensionless variable in (2.3) and omitting the tilde afterwards, we get

$$\begin{aligned} &\frac{U(T_{ref} - T_\infty)}{L}\left(\frac{\partial T_F}{\partial t} + (\mathbf{u}_F \cdot \nabla T_F)\right) \\ &\qquad - \frac{(T_{ref} - T_\infty)}{L^2}\frac{\lambda_F}{c_p^F \rho}\Delta T_F = 0 \qquad \text{in} \quad \Omega_F(t) \times (0, \mathrm{I}). \end{aligned}$$

Multiplying this equation by $L/U(T_{ref} - T_\infty)$, we get the dimensionless form of the energy equation as

$$\frac{\partial T_F}{\partial t} + \mathbf{u}_F \cdot \nabla T_F - \frac{1}{Pe_F}\Delta T_F = 0 \qquad \text{in} \quad \Omega_F(t) \times (0, \mathrm{I}), \tag{2.12}$$

with the initial condition

$$T_F(x, 0) = \frac{T_{F,0} - T_\infty}{T_{ref} - T_\infty} \quad \text{in} \quad \Omega_F(0).$$

Also using the dimensionless variables in the equation (2.4), we get

$$\frac{\partial T_S}{\partial t} - \frac{1}{Pe_S}\Delta T_S = 0 \qquad \text{in} \quad \Omega_S(t) \times (0, \mathrm{I}), \tag{2.13}$$

with the initial condition

$$T_S(x, 0) = \frac{T_{S,0} - T_\infty}{T_{ref} - T_\infty} \quad \text{in} \quad \Omega_S(0).$$

Further the thermal boundary conditions and the transition conditions are also transformed into a dimensionless form

$$-\frac{\partial T_F}{\partial \boldsymbol{\nu}_F} = BiT_F \qquad \text{on } \Gamma_F(t) \times (0, \mathrm{I}), \tag{2.14}$$

$$\frac{\partial T_F}{\partial \boldsymbol{\nu}_F} = -\frac{\lambda_S}{\lambda_F}\frac{\partial T_S}{\partial \boldsymbol{\nu}_S} \qquad \text{on } \Gamma_S(t) \times (0, \mathrm{I}), \tag{2.15}$$

$$T_F = T_S \qquad \text{on } \Gamma_S(t) \times (0, \mathrm{I}), \tag{2.16}$$

$$\frac{\partial T_S}{\partial \boldsymbol{n}} = 0 \qquad \text{on } \Gamma_N(t) \times (0, \mathrm{I}). \tag{2.17}$$

In the above equations, Pe_F, Pe_S and Bi denote the dimensionless Peclet numbers in the fluid and solid, respectively, and Biot number, given by

$$Pe_F = \frac{LUc_p^F\rho}{\lambda_F}, \quad Pe_S = \frac{LUc_p^S\rho_S}{\lambda_S}, \quad Bi = \frac{\alpha_F L}{\lambda_F}.$$

2.2.4 Weak form of the energy equation

The weak form of the energy equation (2.12) is obtained by multiplying it with a test function $\psi_f \in H^1(\Omega_F)$, and integration by parts. After incorporating the boundary conditions (2.14) and using the transition condition

(2.15) to get

$$\begin{aligned}\int_{\Omega_F} \frac{\partial T_F}{\partial t}\psi_f \, dx + \int_{\Omega_F} (\mathbf{u}_F \cdot \nabla) T_F \, \psi_f \, dx + \frac{1}{Pe_F}\int_{\Omega_F} \nabla T_F \cdot \nabla \psi_f \, dx \\ + \int_{\Gamma_F} \frac{Bi}{Pe_F} \, T_F \, \psi_f \, d\gamma_F = -\frac{1}{Pe_F}\frac{\lambda_S}{\lambda_F}\int_{\Gamma_S} \frac{\partial T_S}{\partial \boldsymbol{\nu}_S}\psi_F \, d\gamma_F.\end{aligned} \tag{2.18}$$

Similarly the weak form of the energy equation (2.13) is obtained by multiplying it with a test function $\psi_s \in H^1(\Omega_S)$, and integration by parts. After incorporating the boundary conditions on Γ_S, we get,

$$\int_{\Omega_S} \frac{\partial T_S}{\partial t}\psi_S \, dx + \frac{1}{Pe_S}\int_{\Omega_S} \nabla T_S \cdot \nabla \psi_S \, dx = \frac{1}{Pe_S}\int_{\Gamma_S} \frac{\partial T_S}{\partial \nu_S} \, \psi_S \, d\gamma_S. \tag{2.19}$$

In order to write the energy equations (2.18) and (2.19) in a one-field formulation as a single equation in the domain $\Omega(t) := \Omega_F(t) \cup \Omega_S \cup \Gamma_S(t)$, we define

$$\mathbf{u}_T(x,t) = \begin{cases} \mathbf{u}(x,t) & if \quad x \in \Omega_F(t) \\ 0 & if \quad x \in \Omega_S \end{cases}, \quad T(x,t) = \begin{cases} T_F(x,t) & if \quad x \in \Omega_F(t) \\ T_S(x,t) & if \quad x \in \Omega_S \end{cases},$$

$$Pe(x) = \begin{cases} Pe_F & if \quad x \in \Omega_F(t) \\ \dfrac{\lambda_F}{\lambda_S} Pe_F & if \quad x \in \Omega_S \end{cases}, \quad T_0(x) = \begin{cases} T_{F,0}(x) & if \quad x \in \Omega_F(t) \\ T_{S,0}(x) & if \quad x \in \Omega_S \end{cases}.$$

Moreover, let $g(x) = 1$ in $\Omega_F(t)$ and $g(x) = \lambda_S Pe_S/(\lambda_F Pe_F)$ in Ω_S. Then, multiplying (2.19) with $\lambda_S Pe_S/(\lambda_F Pe_F)$ and adding to (2.18) we end up with the weak one-field formulation of the energy equation:

For given $\Omega(0)$, $\mathbf{u}_T$ and T_0, find $T \in H^1(\Omega)$ such that for all $\psi \in H^1(\Omega)$

$$\left(g\frac{\partial T}{\partial t}, \psi\right)_\Omega + a_T(\mathbf{u}_T, T, \psi) + b_T(T, \psi) = 0. \tag{2.20}$$

The forms a_T and b_T are given by

$$\begin{aligned} a_T(\mathbf{u}_T, T, \psi) &= \int_\Omega \frac{1}{Pe} \, \nabla T \cdot \nabla \psi \, dx + \int_\Omega (\mathbf{u} \cdot \nabla) T \, \psi \, dx, \\ b_T(T, \psi) &= Bi \int_{\Gamma_F} \frac{1}{Pe} \, T \, \psi \, dx. \end{aligned}$$

2.3 Arbitrary Lagrangian Eulerian (ALE) approach

The computational domain of the droplet $\Omega_F(t)$ is time-dependent, that is the boundary of $\Omega_F(t)$ deforms over time. Thus, a special numerical method is needed in order to handle $\Omega_F(t)$ in our numerical scheme. One of the main challenges in computation of flows with moving boundaries is the tracking/capturing of the deforming free surface and/or interface. Based on the treatment of the computational domain, the interface tracking/capturing methods can be classified into two main categories: (i) Eulerian methods (ii) Lagrangian methods. In the Eulerian methods the computational domain is fixed and the fluid flows through the domain. Some of the popular Eulerian interface tracking/capturing methods are the Volume-of-fluid [30, 58, 78], Level set [34, 53, 65, 72], Front tracking [50, 73, 76] and Phase field [43] methods. In all these Eulerian methods, except the Front tracking method, a scalar equation has to be solved in order to capture the interface. In contrary, the interface is represented by a surface mesh in the Front tracking method, and it is moved by the fluid velocity interpolated from the background mesh. Due to the approximation error induced by the scalar equation, accurate calculation of the discrete curvature is very difficult in the Eulerian methods. Since the free surface/interface is not resolved by the computational mesh, incorporating the surface force into the computations requires a special technique such as continuum surface force (CSF) [5]. Even with these additional efforts applied to the Eulerian methods, conserving mass of the fluid is very difficult and often spurious velocities arise [24].
The considered impinging droplet problem is on the micro scale and assumed that there are no topological change in $\Omega_F(t)$. Thus, we prefer the more accurate Arbitrary Lagrangian Eulerian (ALE) approach to track the free surface of the droplet. In the ALE approach, the free surface is resolved by the computation mesh. Further, by an appropriate choice of the pressure space, the spurious velocities can be suppressed in free surface resolved mesh [24].

To rewrite the variational form of the coupled Navier-Stokes and energy equations, we first define a family of ALE mappings

$$\mathcal{A}_t : \hat{\Omega}_F \to \Omega_F(t), \qquad \mathcal{A}_t(\mathbf{Y}) = \mathbf{X}(\mathbf{Y}, t), \qquad t \in (0, T).$$

We assume that the ALE mapping

$$t \to \mathbf{X}(\mathbf{Y}, t), \qquad \mathbf{Y} \in \hat{\Omega}_F$$

is differentiable almost everywhere in the time interval $(0, T)$. For any function $\mathbf{v} \in C^0(\Omega_F)$, we define their corresponding function $\hat{\mathbf{v}} \in C^0(\hat{\Omega}_F)$ as follows:

$$\hat{v} := v \circ \mathcal{A}_t, \qquad \text{with} \qquad \hat{v}(\mathbf{Y}, t) = v(\mathcal{A}_t(\mathbf{Y}), t).$$

Further, the time derivative of $\mathbf{v} \in C^0(\Omega_F)$ on the reference frame

$$\frac{\partial v}{\partial t}\Big|_{\hat{\Omega}_F} : \Omega_F(t) \times (0, \mathrm{I}) \to \mathbb{R}$$

is defined as

$$\frac{\partial v}{\partial t}\Big|_{\hat{\Omega}_F}(\mathbf{X}, t) = \frac{\partial \hat{v}}{\partial t}(\mathbf{Y}, t), \qquad \mathbf{Y} = \mathcal{A}_t^{-1}(\mathbf{X}).$$

Now, applying the chain rule to the time derivative of $v \circ \mathcal{A}_t$ on the reference frame we get

$$\frac{\partial v}{\partial t}\Big|_{\hat{\Omega}_F} = \frac{\partial v}{\partial t}\Big|_{\mathbf{X}} + \frac{\partial \mathbf{X}}{\partial t}\Big|_{\hat{\Omega}_F} \cdot \nabla_{\mathbf{X}} v = \frac{\partial v}{\partial t}\Big|_{\mathbf{X}} + \mathbf{w} \cdot \nabla_{\mathbf{X}} v. \tag{2.21}$$

Here, $\mathbf{w}$ is the domain velocity defined by

$$\mathbf{w}(\mathbf{Y}, t) = \frac{\partial \mathbf{Y}}{\partial t}\Big|_{\hat{\Omega}_F}, \quad \mathbf{Y} \in \hat{\Omega},$$

where $\hat{\Omega}$ is a reference domain of $\Omega(t)$. In computations, the initial domain or the previous time-step domain can be taken as the reference domain. Thus, to rewrite any equation into the ALE form, the time derivative has to be replaced with the time derivative on the reference frame and a convective mesh velocity term has to be added. Now, using (2.21) the variational form of the Navier-Stokes equations (2.11) in the ALE frame reads:

For given $\Omega(0)$, $\mathbf{u}(0)$, find $(\mathbf{u}, p) \in V \times Q$ such that

$$\left(\frac{\partial \mathbf{u}}{\partial t}, \mathbf{v}\right)_{\hat{\Omega}_F} + a(\mathbf{u} - \mathbf{w}; \mathbf{u}, \mathbf{v}) - b(p, \mathbf{v}) + b(q, \mathbf{u}) = f(\mathcal{K}, \mathbf{v}), \tag{2.22}$$

for all $\mathbf{v} \in V$ and $q \in Q$. Further $\hat{\Omega}_F$ is a reference domain of $\Omega_F(t)$. Now, for the energy equation, we define the mesh velocity as

$$\mathbf{w}_T(x, t) = \begin{cases} \mathbf{w} & if \quad x \in \Omega_F \\ \mathbf{w}_S & if \quad x \in \Omega_S \end{cases}$$

where, $\mathbf{w}_S$ is the mesh velocity in Ω_S. The variational form of the energy equation (2.20) in the ALE frame reads:

For given $\mathbf{u}_T$, $\mathbf{w}_T$, $T(0)$, find $T \in H^1(\Omega)$ such that for all $\phi \in H^1(\Omega)$ such that

$$\left(g\frac{\partial T}{\partial t}, \psi\right)_{\hat{\Omega}} + a_T(\mathbf{u}_T - \mathbf{w}_T, T, \psi) + b_T(T, \psi) = 0. \tag{2.23}$$

for all $\psi \in H^1(\Omega)$. Here, $\hat{\Omega}$ is a reference domain of $\Omega(t)$.

Curvature approximation and the contact angle inclusion

Apart from the impinging velocity, one of the main driven force in the deformation of droplet is the surface force. Accurate calculation of the curvature and the precise inclusion of the surface force into the model are challenging in computations of free surface flows.The surface force in the considered impinging droplet contains the temperature dependent surface coefficient and the curvature. Hence, the approximations of the temperature and the curvature have to be very accurate in order to avoid unphysical flows in the droplet [24]. The discrete solution of the energy equation will be discussed later. Here, we present an efficient and accurate technique to approximate the curvature.

The curvature of a manifold can easily be calculated provided that the parametrization of the manifold is given. However, we have only the discrete representation (mesh edges/faces) of the free surface. One of the popular technique to approximate the curvature in the context of finite element methods is the Laplace-Beltrami operator technique [1, 14, 15]. The main advantages of this technique are

- the curvature can be approximated using the finite element basis functions,

- the need of only first derivatives of the basis functions,

- the curvature term can be treated semi-implicitly giving additional stability,

- the contact angle at the moving contact line can be incorporated directly.

Let $U \subset \mathbb{R}^3$ be an open set and $\Gamma_F \subset U$. Now for a scalar function f given on u, we define the tangential gradient

$$\underline{\nabla} f := \nabla f - (\nabla f \cdot \boldsymbol{\nu}_F)\boldsymbol{\nu}_F, \tag{2.24}$$

where $\boldsymbol{\nu}_F$ is the unit normal vector on the free surface $\Gamma_F(t)$. Further, the tangential gradient is denoted componentwise by

$$(\underline{\nabla} f)_i := \delta_i f = \partial_i f - (\boldsymbol{\nu}_F \cdot \nabla f)\nu_{F,i}, \quad i = 1, 2, 3.$$

In the above definitions, we assumed that the values of f are given in a certain neighborhood of $\Gamma_F(t)$. However, it is well-known that the restriction of $\underline{\nabla} f$ on $\Gamma_F(t)$ depends only on the values of f on $\Gamma_F(t)$ [16] (lemma 2.4). Now, the Laplace-Beltrami operator is denoted by

$$\underline{\Delta} f := \sum_{i=1}^{3} \delta_i(\delta_i f). \tag{2.25}$$

For vector-valued functions, the tangential gradient and the Laplace-Beltrami operator are applied in a componentwise manner.

Theorem: (Theorem 2.14 in [16])Assume that Γ_F is a hypersurface in $\mathbb{R}^3$ with smooth boundary ζ_t, $g \in C^1(\overline{\Gamma})$. and $\phi \in C^1(\overline{\Gamma})$. Then,

$$\int_{\Gamma_F} g\ \underline{\Delta}\phi\ ds = -\int_{\Gamma_F} \underline{\nabla} g \cdot \underline{\nabla}\phi\ ds + \int_{\zeta_t} (\boldsymbol{\nu}_\zeta \cdot \underline{\nabla}\phi)\ g\ d\zeta.$$

Note that ζ_t is the contact line (boundary of the free surface). $\boldsymbol{\nu}_\zeta$ is the outward unit normal vector at the contact line with respect to the liquid-gas interface Γ_F.
Using the above theorem, we replace the curvature term $\mathcal{K}\nu_F$ in (2.10) by the Laplace-Beltrami operator (2.25), and applying integration by parts to get

$$
\begin{aligned}
&-\frac{1}{We}\int_{\Gamma_F} M_{T_F}\ \mathbf{v}\cdot\boldsymbol{\nu}_F\mathcal{K}\,d\gamma_F \\
&= -\frac{1}{We}\int_{\Gamma_F} M_{T_F}\ \underline{\Delta} id_{\Gamma_F}\cdot\mathbf{v}\,d\gamma_F \\
&= \frac{1}{We}\int_{\Gamma_F} \underline{\nabla} id_{\Gamma_F} : \underline{\nabla}(M_{T_F}\mathbf{v})\,d\gamma_F - \frac{1}{We}\int_{\zeta_t}(\boldsymbol{\nu}_\zeta\cdot\underline{\nabla} id_{\Gamma_F})\cdot M_{T_F}\mathbf{v}\ d\zeta \\
&= \frac{1}{We}\int_{\Gamma_{F_t}} \underline{\nabla} id_{\Gamma_{F_t}} : [M_{T_F}\underline{\nabla}\mathbf{v} + \mathbf{v}\otimes\underline{\nabla} M_{T_F}]\,d\gamma_F - \frac{1}{We}\int_{\zeta_t}\boldsymbol{\nu}_\zeta\cdot M_{T_F}\mathbf{v}\ d\zeta,
\end{aligned}
\tag{2.26}
$$

Here, we used $\boldsymbol{\nu}_\zeta\cdot\boldsymbol{\nu}_{F_t}=0$ such that $\boldsymbol{\nu}_\zeta\cdot\underline{\nabla} id_{\Gamma_{F_t}}=\boldsymbol{\nu}_\zeta$. Note, that the last term in (2.26), which does not appear for closed surfaces Γ_F, is an integral over the contact line ζ_t and $\boldsymbol{\nu}_\zeta$ is the co-normal vector at the contact line which is normal to ζ_t and tangent to Γ_{F_t}. Let $\boldsymbol{\tau}_S$ be the scaled projection of $\boldsymbol{\nu}_F$ onto the plane Γ_S such that $|\boldsymbol{\tau}_S|=1$ that means

$$
\boldsymbol{\tau}_S := \frac{\boldsymbol{\nu}_F-(\boldsymbol{\nu}_F\cdot\boldsymbol{\nu}_S)\boldsymbol{\nu}_S}{|\boldsymbol{\nu}_F-(\boldsymbol{\nu}_F\cdot\boldsymbol{\nu}_S)\boldsymbol{\nu}_S|}.
$$

Then, $\boldsymbol{\nu}_\zeta\cdot\boldsymbol{\tau}_S=\cos(\theta)$ where θ is the contact angle at the moving contact line. In order to incorporate the contact angle into the model, we decompose the test function $\mathbf{v}$ into

$$
\mathbf{v}=(\mathbf{v}\cdot\boldsymbol{\nu}_S)\boldsymbol{\nu}_S+(\mathbf{v}\cdot\boldsymbol{\tau}_S)\boldsymbol{\tau}_S+(\mathbf{v}\cdot\boldsymbol{\tau}_S^\perp)\boldsymbol{\tau}_S^\perp.
$$

where $\boldsymbol{\tau}_S^\perp$ is a unit vector perpendicular to $\boldsymbol{\nu}_S$ and $\boldsymbol{\tau}_S$. Now, computing the inner product $\boldsymbol{\nu}_\zeta\cdot\mathbf{v}$ in the last term of (2.26) we use $\mathbf{v}\cdot\boldsymbol{\nu}_S=0$ on Γ_S for all $\mathbf{v}\in V$ and the orthogonality $\boldsymbol{\nu}_\zeta\cdot\boldsymbol{\tau}_S^\perp=0$ of the co-normal to get

$$
\begin{aligned}
\int_\zeta \boldsymbol{\nu}_\zeta\cdot M_{T_F}\mathbf{v}\ d\zeta &= \int_\zeta(\boldsymbol{\nu}_\zeta\cdot\boldsymbol{\tau}_S)(\mathbf{v}\cdot\boldsymbol{\tau}_S)M_{T_F}\ d\zeta \\
&= \int_\zeta \cos(\theta)\ M_{T_F}\mathbf{v}\cdot\boldsymbol{\tau}_S\ d\zeta.
\end{aligned}
\tag{2.27}
$$

In our model, we use the equilibrium contact angle as in [23].

3 Spatial and temporal discretization

3.1 Finite element spaces

In computations, we use conforming finite element spaces for the temperature, velocity and pressure spaces, that is, subspaces of $H^1(\Omega)$, $H^1(\Omega_F)^d$, and $L^2(\Omega_F)$. Therefore, to guarantee that the discrete velocity space satisfies $V_h \subset H^1(\Omega)^d$, we need continuous $V_h \subset H^1(\Omega)$. For the pressure approximation, we use a discontinuous space $Q_h \subset L^2(\Omega_F)$. Unlike continuous finite element spaces, discontinuous finite element spaces have no continuity condition across the cell boundaries. To construct a finite element space we need to define their local basis function space together with its local nodal functionals. Our definition of the basis function and their nodal functionals are based on the definitions given in [8]. We restrict our definition of finite elements to the two-dimensional (2D) case, since the computations are performed in 3D-axisymmetric configurations.

3.1.1 Finite element

Let

(i) $K \subseteq \mathbb{R}^d,\ d = 2$ be a domain with piecewise smooth boundary,

(ii) P_K be a finite dimensional space of functions on K, with m = dim P_K,

(iii) $\mathcal{N} = \{N_1, N_2, ..., N_m\}$ be a set of linear functionals $N_i, i = 1, 2, ..., m$ which are defined over sufficiently smooth functions, in particular over P_K.

Then $(K, P_K, \mathcal{N})$ is called a finite element. It is implicitly assumed that the set of linear functional $\mathcal{N}$ is P_K-unisolvent in the sense that for any given real numbers $\alpha_i,\ i = 1, 2, ..., m$ there exist a unique function $v \in P_K$ such that

$$N_i(v) = \alpha_i, \quad 1 \leq i \leq m.$$

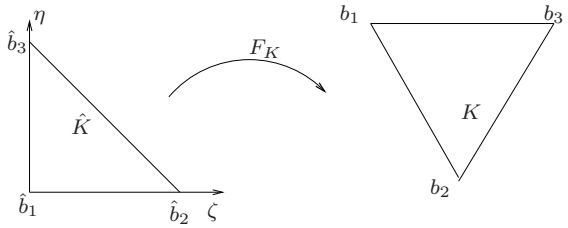

Figure 3.1: Affine transformation from the reference cell onto the original cell.

In particular, there exist m functions $\phi_i \in V,\ i = 1, 2, ..., m$, which satisfy

$$N_j(\phi_i) = \delta_{ij}, \quad 1 \leq i, j \leq m, \tag{3.1}$$

where δ_{ij} is the Kronecker delta. The linear functionals $N_i,\ i = 1, 2, ..., m$, are called nodal functionals and the functions $\phi_i,\ i = 1, 2, ..., m$, are called local basis or shape functions.

3.1.2 Triangulation of two-dimensional (2D) domains

We triangulate the 2D domain using triangles. Let $\mathcal{T}_h$ be the triangulation of the Polygon $\Omega \subset \mathbb{R}^2$ into triangular cells K. Assume the usual regularity conditions:

- $\overline{\Omega} = \bigcup K,\ K \in \mathcal{T}_h$.
- Any two cells K, K' intersects only at common edges or vertices.
- Cells of the triangulation $\mathcal{T}_h$ resolves the boundary $\partial\Omega$, which follows from $\overline{\Omega} = \bigcup K$.

Further, we assume that each cell $K \in \mathcal{T}_h$ is associated with an element-size $h_K := diam(K)$, and we denote $h := max_{K \in \mathcal{T}_h} h_K$. In our implementation, we use mapped finite elements, that is, we compute all basis function values on the reference cell $\hat{K}$ and transform it to the original cells. The reference transformation of the local basis functions and its derivative will be an affine or isoparametric mapping. Next, we present the affine transformation for triangles.

3.1.3 Affine transformation

Let (0, 0), (1,0) and (0,1) be the vertices $\hat{b}_i,\ i = 1, 2, 3$ of the reference triangle $\hat{K}$. Further, let $\lambda_i := \lambda_{i,\hat{K}}(\hat{X}),\ 1 \leq i \leq 3$ be the barycentric coordinates of the reference triangle. Similarly, the vertices $(x_i, y_i),\ i =$

$1, 2, 3$ of the original cell are denoted by b_i, $i = 1, 2, 3$. Let $X = (x,\ y)$ be the Cartesian coordinate in the original cell K, and using the barycentric coordinates it can be expressed as

$$\begin{aligned}\begin{pmatrix} x \\ y \end{pmatrix} &= \sum_{i=1}^{3} b_i \lambda_i \\ &= b_1(1-\hat{x}-\hat{y}) + b_2\hat{x} + b_3\hat{y} \\ &= b_1 + (b_2 - b_1)\hat{x} + (b_3 - b_1)\hat{y} \\ &= \begin{pmatrix} x_2 - x_1 & x_3 - x_1 \\ y_2 - y_1 & y_3 - y_1 \end{pmatrix} \begin{pmatrix} \hat{x} \\ \hat{y} \end{pmatrix} + \begin{pmatrix} x_1 \\ y_1 \end{pmatrix} = B_K \begin{pmatrix} \hat{x} \\ \hat{y} \end{pmatrix} + b_1.\end{aligned}$$

Thus, we have $X = F_K(\hat{X}) = B_K\hat{X} + b_1$.

Affine equivalent finite element spaces

Let $\mathcal{T}_h$ be the triangulation of Ω, and P_K, $\mathcal{N}$ be as in the section 3.1.1. Further, let $(\hat{K}, \hat{P}, \hat{\mathcal{N}})$ be a reference finite element. Then, the finite element $(K, P_K, \mathcal{N})$ on the original cell K is said to be affine equivalent to the reference finite element, if for each K there exist an affine bijective mapping $F_K : \hat{K} \to K$ such that

$$\begin{aligned} K &= F_K(\hat{K}) \\ P_K &:= \{\phi = \hat{\phi} \circ F_K^{-1} \quad \forall \quad \hat{\phi} \in \hat{P}\}.\end{aligned}$$

For any function $u(X)$ we denote $u(X) = u(F_k(\hat{X})) = \hat{u}(\hat{X})$. Further, the derivatives of the function, $\partial u/\partial x$ and $\partial u/\partial y$ on the original cell can be obtained in terms of $\partial\hat{u}/\partial\hat{x}$ and $\partial\hat{u}/\partial\hat{y}$ as follows:

$$\begin{aligned}\hat{u}(\hat{X}) &= \hat{u}(F_K^{-1}(X)) = u(X) \\ \frac{\partial\hat{u}}{\partial\hat{x}} &= \frac{\partial u}{\partial x}\frac{\partial x}{\partial\hat{x}} + \frac{\partial u}{\partial y}\frac{\partial y}{\partial\hat{x}}, \\ \frac{\partial\hat{u}}{\partial\hat{y}} &= \frac{\partial u}{\partial x}\frac{\partial x}{\partial\hat{y}} + \frac{\partial u}{\partial y}\frac{\partial y}{\partial\hat{y}}.\end{aligned}$$

Thus, we get

$$\begin{pmatrix} \dfrac{\partial\hat{u}}{\partial\hat{x}} \\[2ex] \dfrac{\partial\hat{u}}{\partial\hat{y}} \end{pmatrix} = \begin{bmatrix} (x_2 - x_1) & (y_2 - y_1) \\[2ex] (x_3 - x_1) & (y_3 - y_1) \end{bmatrix} \begin{pmatrix} \dfrac{\partial u}{\partial x} \\[2ex] \dfrac{\partial u}{\partial y} \end{pmatrix}.$$

Finally, we have

$$\begin{pmatrix} \dfrac{\partial u}{\partial x} \\ \\ \dfrac{\partial u}{\partial y} \end{pmatrix} = \frac{1}{\det B_K} \begin{bmatrix} (y_3 - y_1) & -(y_2 - y_1) \\ \\ -(x_3 - x_1) & (x_2 - x_1) \end{bmatrix} \begin{pmatrix} \dfrac{\partial \hat{u}}{\partial \hat{x}} \\ \\ \dfrac{\partial \hat{u}}{\partial \hat{y}} \end{pmatrix}.$$

3.1.4 Finite elements on triangles

We use the following inf-sup stable finite element pairs for the Navier-Stokes equation:

(i) Taylor-Hood (P_2/P_1), continuous, piecewise quadratic for the velocity and continuous, piecewise linear for the pressure [10].

(ii) Crouzeix-Raviart (P_2^{bubble}/P_1^{disc}), continuous, piecewise quadratic enriched with cubic bubble for the velocity and discontinuous, piecewise linear for the pressure [33].

Further, the energy and linear elasticity equations are spatially discretized using continuous P_2 and P_1 finite elements, respectively. Now, we present the basis functions and their nodal functionals for these elements.

Continuous finite element $P_k(\hat{K}),\ k \geq 1$

The space of local shape functions of these finite elements are the spaces $\mathbb{P}_k(\hat{K})$ of all polynomials of degree less than or equal to k. Furthermore,

$$N_{ij}^k(p) : C^0(\hat{K}) \to \mathbb{R}, \qquad p \mapsto p(i/k, j/k), \qquad 0 \leq i + j \leq k,$$

defines nodal functionals by point values. The set

$$\mathcal{N}_k := \{N_{ij}^k : 0 \leq i + j \leq k\},$$

gives a set of nodal functionals which is $\mathbb{P}_k(\hat{K})$-unisolvent. The triple $(\hat{K},\ \hat{\mathbb{P}}_k(\hat{K}),\ \hat{\mathcal{N}_k})$ is a finite element on $\hat{K}$. The finite element space constructed using this finite element will be conforming and continuous on the edges/faces of the triangulation, see Section 3.1.5. Thus, this class of finite elements, P_k, are called continuous finite elements.

Continuous $P_2^{bubble}(\hat{K})$ on triangles

The set of local shape functions for this quadratic element is the space $\mathbb{P}_2(\hat{K})$ of all polynomials of degree less than or equal to two enriched by a polynomial cubic bubble function $\mathbb{B}_3(\hat{K})$. We denote $\mathbb{P}_2^{bubble} := \mathbb{P}_2(\hat{K}) \oplus \mathbb{B}_3(\hat{K})$ as a space of local shape functions, which is spanned by

$$P_2^{bubble}(\hat{K}) = \text{Span } \{\lambda_1^2,\ \lambda_2^2,\ \lambda_3^2,\ \lambda_1\lambda_2,\ \lambda_2\lambda_3,\ \lambda_3\lambda_1,\ \lambda_1\lambda_2\lambda_3\}.$$

Now, we define the nodal functionals of the quadratic local shape functions by point values, *i.e.*, for integers i and j, we have

$$N_{ij}(p) : C^0(\hat{K}) \to \mathbb{R}, \qquad p \mapsto p(i/2, j/2), \qquad 0 \le i + j \le 2,$$

and the nodal functional of the cubic bubble function p^{bub} by the integral mean value of the reference cell $\hat{K}$, *i.e.*,

$$\hat{N}_7(p) = \frac{1}{|\hat{K}|} \int_{\hat{K}} p(\hat{X})\ d\hat{X}.$$

The above integral is evaluated with an appropriate quadrature formula, which is exact for polynomial of order three on triangles. We denote

$$\hat{\mathcal{N}} = \{N_{ij},\ \hat{N}_7\}, \qquad 0 \le i + j \le 2,$$

and the elements in $\hat{\mathcal{N}}$ form a set of nodal functionals which are $\mathbb{P}_2^{bubble}$-unisolvent. Note that the weights of the local basis functions except ϕ_7 are chosen in such a way that the nodal functionals $\hat{\mathcal{N}}_j,\ j = 1, 2, ..., 6$ satisfy the condition (3.1). We use a cubic bubble function for ϕ_7. Hence, the basis functions $\phi_i(\hat{x})$, $i = 1, 2, ..., 7$, are given by

$$\begin{array}{lcllcl}
\phi_1 &=& (1-\hat{x}-\hat{y})(1-2\hat{x}-2\hat{y}), & \phi_2 &=& 4\hat{x}(1-\hat{x}-\hat{y}) - 20\hat{x}\hat{y}(1-\hat{x}-\hat{y}),\\
\phi_3 &=& \hat{x}(2\hat{x}-1), & \phi_4 &=& 4\hat{y}(1-\hat{x}-\hat{y}) - 20\hat{x}\hat{y}(1-\hat{x}-\hat{y}),\\
\phi_5 &=& 4\hat{x}\ \hat{y} - 20\ \hat{x}\ \hat{y}(1-\hat{x}-\hat{y}), & \phi_6 &=& \hat{y}(2\hat{y}-1),\\
\phi_7 &=& 20\hat{x}\ \hat{y}(1-\hat{x}-\hat{y}). & & &
\end{array}$$

Finally, we denote the finite element $(\hat{K},\ \hat{\mathbb{P}}_2^{bubble}(\hat{K}),\ \hat{\mathcal{N}})$ shortly by $P_2^{bubble}(\hat{K})$.

Remark: Note that the nodal functional, $\hat{N}_7$, in the P_2^{bubble} element is defined by weighted integral values, whereas all other nodal functionals in P_2^{bubble} are defined by point values.

Discontinuous P_1^{disc} on triangles

The set of local shape functions of this linear finite element is the space $\mathbb{P}_1(\hat{K})$ of polynomial of degree less than or equal to 1 which is spanned by the barycentric coordinates

$$\{\lambda_1,\ \lambda_2,\ \lambda_3\}.$$

The nodal functionals P_1^{disc} are defined by linear combination of the moments

$$\frac{1}{|\hat{K}|}\int_{\hat{K}}(1,\hat{x},\hat{y})\ p(\hat{X})\ d\hat{X}.$$

In particular, we define the nodal functionals as follows

$$\begin{aligned}
\hat{N}_1^{disc}(p) &= \frac{1}{|\hat{K}|}\int_{\hat{K}} p(\hat{X})\ d\hat{X},\\
\hat{N}_2^{disc}(p) &= \frac{1}{|\hat{K}|}\int_{\hat{K}}\left(\hat{x}-\frac{1}{3}\right)\ p(\hat{X})\ d\hat{X},\\
\hat{N}_3^{disc}(p) &= \frac{1}{|\hat{K}|}\int_{\hat{K}}\left(\hat{y}-\frac{1}{3}\right)\ p(\hat{X})\ d\hat{X}.
\end{aligned} \tag{3.2}$$

Note that as a consequence of this choice we can guarantee that the first of the local basis functions satisfying (3.1) is equal to 1. This property is used in the implementation and allows to work with a basis not belonging to $L_0^2(\Omega)$. The above integrals are evaluated with an appropriate quadrature formula, which is exact for polynomials of order two on triangles. Now, the set of nodal functionals

$$\hat{\mathcal{N}}^{disc} = \{\hat{N}_1^{disc}, \hat{N}_2^{disc}, \hat{N}_3^{disc}\}$$

is $\mathbb{P}_1(\hat{K})$-unisolvent. Furthermore, we choose the local shape functions in such a way that the condition (3.1) is satisfied. Hence, we obtained the following local shape functions

$$\{1,\ \hat{x}+\hat{y}/2-1/2,\ \hat{x}/2+\hat{y}-1/2\}.$$

The triplet $(\hat{K},\ \mathbb{P}_1(\hat{K}),\ \hat{\mathcal{N}}^{disc})$ is a finite element of $\hat{K}$, and we denote it by $P_1^{disc}(\hat{K})$.

3.1.5 Discontinuous and Continuous finite element spaces

Let $K \in \mathcal{T}_h$ be an original cell and $(K, P_K, \mathcal{N})$ be their corresponding finite element. Then, a discontinuous finite element space V_h is defined by

$$V_h = \{v_h \in L^2(\Omega) : \quad v_h\Big|_K \in P_K\}.$$

In general, a finite element space consists of a collection of same class of finite elements instead of arbitrary class of finite elements. The next lemma give a sufficient condition such that our finite element space V_h is a subspace of our solution space $H^1(\Omega)$.

Lemma 3.1.1 (H^1-conformity of finite elements) *Let V_h be a finite element space. Assume that $P_K \subset H^1(K)$, $K \in \mathcal{T}_h$ and $V_h \subset C^0(\Omega)$. Then, $V_h \subset H^1(\Omega)$.*

Proof. Let $v_h \in V_h$, then we obviously have $v_h \in L^2(\Omega)$. Now, we have to show that v_h admits first derivatives $w_h \in L^2(\Omega)$, that is,

$$\int_\Omega v_h Dz \; dx = -\int_\Omega w_h z \; dx, \qquad \forall \; z \in C_0^\infty(\Omega).$$

Since $v_h|_K \subset H^1(K)$, we apply the Green's identity element-wise and obtain

$$\begin{aligned}\int_\Omega v_h Dz \; dx &= \sum_{K\in\mathcal{T}_h} \int_K v_h Dz \; dX \\ &= -\sum_{K\in\mathcal{T}_h} \int_K Dv_h z \; dX + \sum_{K\in\mathcal{T}_h} \int_{\partial K} v_h n z \; ds \\ &= -\sum_{K\in\mathcal{T}_h} \int_K Dv_h z \; dX + \sum_{E\in E_h(\Omega_h)} \int_E [v_h] n z \; ds.\end{aligned}$$

Here, $[v_h]$ denotes the jump $[v_h] := v_h|_{K_1} - v_h|_{K_2}$ across the edge $E := K_1 \cap K_2$, $K_i \in \mathcal{T}_h$, E_h is a set of all edges in $\mathcal{T}_h$. Since $V_h \subset C^0(\Omega)$, we have $[v_h] = 0$, which proves the lemma with $w_h|_K := Dv_h|_K, \; K \in \mathcal{T}_h$. ∎

Remark: Finite element spaces which satisfy the Lemma 3.1.1 are called continuous piecewise P_K elements.

3.2 Stable finite element discretization of Stokes equations

For simplicity of presentation we restrict to Stokes problem. The extension to Navier–Stokes equation is straight forward in case of small data. Let us consider the stationary Stokes problem in a fixed domain $\Omega \subset \mathbb{R}^2$ with inhomogeneous Dirichlet boundary condition

$$\begin{aligned} -\Delta \mathbf{u} + \nabla p &= \mathbf{f} \quad \text{in } \Omega, \\ \nabla \cdot \mathbf{u} &= 0 \quad \text{in } \Omega, \\ \mathbf{u} &= \mathbf{u}_D \quad \text{on } \partial\Omega, \end{aligned} \tag{3.3}$$

where $\mathbf{u}$ is the velocity, p is the pressure and f is the external force. Let

$$V := H^1(\Omega)^2, \quad V_0 := H_0^1(\Omega)^2 = \{v \in H^1(\Omega)^2 \ : \ v = 0 \text{ on } \partial\Omega\},$$

$$Q := L_0^2(\Omega) = \{q \in L^2(\Omega) \ : \ (q, 1) = 0\}.$$

Now, the variational form of the Stokes equations (3.3) is derived in the usual way by multiplying it with test functions $(\mathbf{v},\ q) \in V_0 \times Q$ and applying integration by parts to get:

Find $(\mathbf{u},\ p) \in V \times Q$ with $\mathbf{u}|_{\partial\Omega} = \mathbf{u}_D$ for all $(\mathbf{v},\ q) \in V_0 \times Q$ such that

$$a(\mathbf{u}, \mathbf{v}) - b(p, \mathbf{v}) + b(q, \mathbf{u}) = (\mathbf{f}, \mathbf{v}). \tag{3.4}$$

Here, the vector and scalar bilinear forms are defined as

$$a(\mathbf{u}, \mathbf{v}) := \int_\Omega \nabla \mathbf{u} : \nabla \mathbf{v} \ dx, \quad b(q, \mathbf{v}) := \int_\Omega q \ \nabla \cdot \mathbf{v} \ dx, \quad (f, \mathbf{v}) := \int_\Omega f \mathbf{v} \ dx.$$

Now, to show the existence and uniqueness of the solution of the Stokes problem (3.4), the *inf-sup* or "Babuska-Brezzi" condition: there exists a constant $\beta_0 > 0$ such that

$$\sup_{\mathbf{v} \in V_0} \frac{b(q, \mathbf{v})}{|\mathbf{v}|_{1,\Omega}} \geq \beta_0 ||q||_{0,\Omega} \qquad \forall\ q \in Q, \tag{3.5}$$

has to be fulfilled. The following lemma shows the existence and uniqueness of the solution of the Stokes problem (3.4).

Lemma 3.2.1 (see, Theorem 5.1 in [33]) *Let Ω be a bounded domain in $\mathbb{R}^2$ with a Lipschitz-continuous boundary $\partial\Omega$. Given $\mathbf{f} \in \mathbf{H^{-1}(\Omega)^2}$ and $\mathbf{u}_D \in H^{1/2}(\partial\Omega)^2$ such that*

$$\int_{\partial\Omega} \mathbf{u}_D \cdot \boldsymbol{\nu}\ ds = 0.$$

Then there exist a unique pair $(\mathbf{u}, p) \in V \times Q$ as a solution of the Stokes equations.

Proof. The proof follows from the elliptic property of the bilinear form $a(\cdot,\cdot)$ and the *inf-sup* condition (3.5). ∎

Discrete form

Now, let us derive the discrete form of the Stokes equations (3.3). Let V_h, $V_{h,0}$ and Q_h be the discrete analog of the spaces V, V_0 and Q, respectively. Then, the discrete form of (3.4) reads:

Find $(\mathbf{u}_h, p_h) \in V_h \times Q_h$ with $\mathbf{u}_h|_{\partial\Omega} = \mathbf{u}_{D,h}$ and $\int_{\partial\Omega} \mathbf{u}_{D,h} \cdot \boldsymbol{n}\ d\gamma = 0$, such that

$$a_h(\mathbf{u}_h, \mathbf{v}_h) - b_h(p_h, \mathbf{v}_h) + b_h(q_h, \mathbf{u}_h) = (\mathbf{f}, \mathbf{v_h}) \tag{3.6}$$

for all $(\mathbf{v}_h, q_h) \in V_{h,0} \times Q_h$. Here, the discrete bilinear forms are defined as

$$a_h(\mathbf{u}_h, \mathbf{v}_h) := \sum_{K \in \mathcal{T}_h} \int_K \nabla \mathbf{u}_h : \nabla \mathbf{v}_h\ dK, \quad b_h(p_h, \mathbf{v}_h) := \sum_{K \in \mathcal{T}_h} \int_K q_h\ \nabla \cdot \mathbf{v}_h\ dK.$$

Next, in order to show the unique solvability of the discrete problem (3.6), we define the following hypotheses:

Hypothesis H1 (Approximation property of V_h). There exist an interpolation operator

$$I_h \in \mathcal{L}(H^2(\Omega)^2; V_h) \cap \mathcal{L}((H^2(\Omega) \cap H_0^1(\Omega))^2; V_{h,0})$$

and an integer m such that:

$$||\mathbf{v} - I_h\mathbf{v}||_{1,\Omega} \leq Ch^l ||\mathbf{v}||_{l+1,\Omega} \qquad \forall\ \mathbf{v} \in H^{m+1}(\Omega)^2, \quad 1 \leq l \leq m.$$

Here, $\mathcal{L}(X; Y)$ denotes the set of linear and continuous mappings from X to Y.

Hypothesis H2 (Approximation property of Q_h). There exists an interpolation operator

$$J_h \in \mathcal{L}(L_0^2(\Omega); Q_h)$$

such that:

$$||q - J_h q||_{0,\Omega} \leq C h^l ||q||_{l,\Omega} \qquad \forall\, q \in H^m(\Omega), \quad 1 \leq l \leq m.$$

Hypothesis H3 (Discrete *inf-sup* condition) There exists a positive constant β_1 independent of the mesh parameter h such that

$$\inf_{q_h \in Q_h} \sup_{v_h \in V_{h,0}} \frac{b_h(q_h, v_h)}{\|q_h\|_0 \, |v_h|_{1,h}} \geq \beta_1 > 0. \tag{3.7}$$

The following theorem provides the unique solvability of the discrete problem (3.6).

Lemma 3.2.2 (see Theorem 1.8 in [33]) *Let the hypotheses* H1*,* H2 *and* H3 *be fulfilled. Then, the discrete problem* (3.6) *has a unique solution* $(\mathbf{u}_h, p_h) \in V_h \times Q_h$*, which is also a weak solution of* (3.3)*. Furthermore, if the solution of* (3.4) *is* $(\mathbf{u}, p) \in \left(H_0^1(\Omega) \cap H^{m+1}(\Omega)\right)^2 \times (L_0^2(\Omega) \cap H^m(\Omega))$ *for some positive integer* m*, then we have the error bound:*

$$|\mathbf{u} - \mathbf{u}_h|_{1,\Omega} + ||p - p_h||_{0,\Omega} \leq C h^m \left(||\mathbf{u}||_{m+1,\Omega} + ||p||_{m,\Omega} \right).$$

The following finite element pairs

(i) Taylor-Hood (P_2/P_1), continuous, piecewise quadratic for the velocity and continuous, piecewise linear for the pressure,

(ii) Crouzeix-Raviart $(P_2^{bubble}/P_1^{disc})$, continuous, piecewise quadratic enriched with cubic bubble for the velocity and discontinuous, piecewise linear for the pressure,

satisfy the Hypothesis H1 and H2 for $m = 2$ and also H3, see [10, 33]. For on overview of other finite element pairs which satisfy the *inf-sup* condition, we refer to [11, 22, 48, 49].

3.3 Temporal discretization

The first order forward and backward Euler schemes, the second order Crank-Nicolson and the fractional-step θ-schemes are presented in this section. Further, a linearization of the nonlinear Navier-Stokes system is presented.

One-step-ϑ scheme

Let $0 = t_1 < t_2 <, ..., < t_n = I$ be the decomposition of the given time interval $[0, I]$. Further, let $\delta t = t_n - t_{n-1}, i = 1, ..., n$, be an uniform time-step. Then, the generalized one-step ϑ-scheme for the variational form of the Navier-Stokes equations (2.22) read:

For given $\Omega_F(t_n)$, $\mathbf{u}^n \in V(\Omega_F(t_n))$ and $\mathbf{w}^n \in H^1(\Omega_F(t_n))$, find $\mathbf{u} = \hat{\mathbf{u}}^{n+1} \in V(\hat{\Omega}_F)$, $\mathbf{w} = \mathbf{w}^{n+1}$ and $p = \hat{p}^{n+1} \in Q(\hat{\Omega}_F)$ such that

$$\begin{aligned}\left(\frac{\mathbf{u}-\mathbf{u}^n}{\delta t}, \mathbf{v}\right)_{\hat{\Omega}_F} &+ \vartheta a(\mathbf{u}-\mathbf{w}; \mathbf{u}, \mathbf{v})_{\hat{\Omega}_F} - b(p, \mathbf{v})_{\hat{\Omega}_F} + b(q, \mathbf{u})_{\hat{\Omega}_F} \\ &= f(\mathcal{K}^{n+1}, \mathbf{v})_{\hat{\Omega}_F} - (1-\vartheta) a(\mathbf{u}^n - \mathbf{w}^n; \mathbf{u}^n, \mathbf{v}), \qquad (3.8)\end{aligned}$$

for all $\mathbf{v} \in V(\hat{\Omega}_F)$ and $q \in Q(\hat{\Omega}_F)$. Here, $\hat{\Omega}_F$ is the reference domain and we use the previous time step domain as the reference domain, that is $\hat{\Omega}_F = \Omega_F(t_n)$ and we choose $\Omega_F(t_n)$ as reference domain in computations. Note that we have treated the right hand side implicitly.

Next, the generalized one-step ϑ-scheme for the variational form of the energy equation (2.23) reads:

For given $\Omega(t_n)$, $T^n \in H^1(\Omega(t_n))$, $\mathbf{u}_T^n \in V(\Omega(t_n))$, $\mathbf{w}_T^n \in H^1(\Omega(t_n))$, $\hat{\mathbf{u}}_T^{n+1}$ and $\hat{\mathbf{w}}_T^{n+1}$, find $\hat{T}^{n+1} \in H^1(\hat{\Omega})$ such that

$$\begin{aligned}\left(\frac{\hat{T}^{n+1}-T^n}{\delta t}, g\psi\right)_{\hat{\Omega}} &+ \vartheta \left[a_T(\hat{\mathbf{u}}_T^{n+1} - \hat{\mathbf{w}}_T^{n+1}, \hat{T}^{n+1}, \phi)_{\hat{\Omega}} + b_T(\hat{T}^{n+1}, \phi)_{\hat{\Omega}}\right] \\ &= -(1-\vartheta)\left[a_T(\mathbf{u}_T^n - \mathbf{w}_T^n, \hat{T}^{n+1}, \phi)_{\hat{\Omega}} + b_T(T^n, \phi)_{\hat{\Omega}}\right], \qquad (3.9)\end{aligned}$$

for all $\psi \in H^1(\hat{\Omega})$. Here, $\hat{\Omega}$ is the reference domain and again it is chosen as $\hat{\Omega} = \Omega(t_n)$. Now, by choosing different values for ϑ in the above generalized one-step ϑ-scheme, we get the following schemes

- $\vartheta = 0$
  The forward-Euler method, which is explicit and first order accurate. In general, there will be a restriction on the time step to have stability.

- $\vartheta = 1$
  The backward-Euler method, which is implicit, first order accurate and strongly A-stable. It is mostly preferred because of its stability property.

- $\vartheta = 0.5$
  The Crank-Nicolson method, which is second order. Occasionally it may suffer from unexpected instabilities, since this method is not strongly A-stable.

In the implicit schemes (backward-Euler and Crank-Nicolson), the convection term in the semi-discrete (in time) Navier-Stokes equation (3.8) will remains nonlinear, and a linearization technique is necessary in order to solve the nonlinear algebraic system of equations. Thus, we use as in [26], a fixed point iteration. At time t^{n+1}, we start with $\mathbf{u}_0^{n+1} := \mathbf{u}^n$ and $\mathbf{w}_0^{n+1} := \mathbf{w}^n$, then replacing $a(\mathbf{u}^{n+1} - \mathbf{w}^{n+1}, \mathbf{u}^{n+1}, \mathbf{v})$ by $a(\mathbf{u}_{i-1}^{n+1} - \mathbf{w}_{i-1}^{n+1}, \mathbf{u}_i^{n+1}, \mathbf{v})$, $i = 1, 2, \ldots,$. Note that in each step of the fixed point iteration, the linear elasticity problem has to be solved to determine the mesh velocity $\mathbf{w}_i^n$, $i = 1, 2, \ldots$, 'virtually' without moving the mesh.

Next, the curvature in the semi-discrete (in time) Navier-Stokes equation (3.8) can be treat as explicit. However, it leads to a restriction on the time step [1, 5]. Also, the implicit treatment of the curvature is too complicated. Therefore, for the curvature integral (2.26) in (3.8) we use a semi-implicit form

$$
\begin{aligned}
&-\frac{1}{We}\int_{\hat{\Gamma}_F^{n+1}} \underline{\nabla} id_{\Gamma_F(t_{n+1})} : [M_{T_F^{n+1}} \underline{\nabla}\mathbf{v} + \mathbf{v} \otimes \underline{\nabla} M_{T_F^{n+1}}]\, d\gamma_F \\
&\approx -\frac{1}{We}\int_{\hat{\Gamma}_F^{n}} \underline{\nabla}(id_{\Gamma_F(t_n)} + \delta t \hat{\mathbf{u}}^{n+1}) : [M_{T_F^{n+1}} \underline{\nabla}\mathbf{v} + \mathbf{v} \otimes \underline{\nabla} M_{T_F^{n+1}}]\, d\gamma_F, \quad (3.10)
\end{aligned}
$$

as in [1]. The additional term

$$
d(\mathbf{u}^{n+1}, \mathbf{v}) := -\frac{\delta t}{We}\int_{\hat{\Gamma}_F^{n}} \underline{\nabla}\hat{\mathbf{u}}^{n+1} : [M_{T_F^{n+1}} \underline{\nabla}\mathbf{v} + \mathbf{v} \otimes \underline{\nabla} M_{T_F^{n+1}}]\, d\gamma_F, \quad (3.11)
$$

which would be symmetric and positive semi-definite in case of constant

surface tension, adds stability to the equation (3.8). Recall that

$$M_{T_F^{n+1}} = \left(1 - \frac{\mathcal{C}_1}{\sigma_{sa}}(T_F^{n+1} - 1)\right).$$

Due to the semi-implicit choice of the curvature integral, equations (3.10) and (3.11) require the unknown temperature T_F^{n+1} at time $t = t_{n+1}$. Similarly, the semi-discrete (in time) energy equation (3.9) requires the unknown fluid velocity for their convection term. One of the efficient ways to handle this coupled system is to solve the energy equation within the fixed point iteration step of the Navier-Stokes equation. However, this leads to huge computational costs. In our implementation, we first solve the Navier-Stokes equations by treating the temperature explicitly,

$$\begin{aligned} -\frac{1}{We}\int_{\hat{\Gamma}_F^n} \underline{\nabla}(id_{\Gamma_F(t_n)} + \delta t\hat{\mathbf{u}}^{n+1}) : [M_{T_F^{n+1}}\underline{\nabla}\mathbf{v} + \mathbf{v}\otimes\underline{\nabla}M_{T_F^{n+1}}]\, d\gamma_F \\ \approx -\frac{1}{We}\int_{\hat{\Gamma}_F^n} \underline{\nabla}(id_{\Gamma_F(t_n)} + \delta t\hat{\mathbf{u}}^{n+1}) : [M_{T_F^{n}}\underline{\nabla}\mathbf{v} + \mathbf{v}\otimes\underline{\nabla}M_{T_F^{n}}]\, d\gamma_F \end{aligned}$$

that is, we take the previous time step temperature value. Once the fluid velocity is computed, then the energy equation (3.9) is solved by considering the new velocity value in the convection term.

Fractional-step-ϑ scheme

The forward Euler scheme is first order and explicit, and requires very small time steps to guarantee stability. The backward Euler scheme is implicit but only first order. We prefer second order accurate temporal discretisation schemes, since we use second order finite element for spatial discretisation of the fluid velocity and the temperature. Thus, we could use the Crank-Nicolson scheme, which is second order but it is not strongly A-stable, *i.e*, it induces oscillations in the numerical solution when there is some noise in the data. Alternatively, the fractional-step-θ scheme for incompressible Navier-Stokes equations has been proposed in [7] as an operator-splitting scheme to split the nonlinear convection term and the incompressibility constrain. The fractional-step-θ scheme is strongly A-stable and of second order convergent – on fixed domains –, see [75, Chapter 3.2.1] for more details. It is a clever combination of three one-step ϑ schemes in each time step. Further, our experience with the Navier-Stokes solvers on fixed domains suggests to use the fractional-step-θ scheme which has nice properties. Also, we should note that the computational cost of

the fractional-step-ϑ scheme will increase three times in comparison to the Crank-Nicolson scheme.

In the following we present the fractional-step-ϑ scheme for the Navier-Stokes and energy equations. Let

$$\vartheta = 1 - \frac{\sqrt{2}}{2}, \quad \tilde{\vartheta} = 1 - 2\vartheta, \quad \eta = \frac{\tilde{\vartheta}}{1-\vartheta}, \quad \tilde{\eta} = 1 - \eta.$$

Further, we split the time interval (t_n, t_{n+1}) into three sub-intervals as (t_n, t_{n_1}), (t_{n_1}, t_{n_2}) and (t_{n_2}, t_{n+1}), where $t_{n_1} = t_n + k_n\vartheta$, and $t_{n_2} = t_{n+1} - k_n\vartheta$. Applying the fractional-step ϑ-scheme, the semi-discrete (time) form of the variational form of the Navier-Stokes equation (2.22) and the energy equation (2.23) read:

Step 1.
For given $\Omega_F(t_n)$, $T^n \in H^1(\Omega(t_n))$, $\mathbf{u}^n \in V(\Omega_F(t_n))$ and $\mathbf{w}^n \in H^1(\Omega_F(t_n))$, find $\mathbf{u} = \hat{\mathbf{u}}^{n_1} \in V(\hat{\Omega}_F)$, $\mathbf{w} = \hat{\mathbf{w}}^{n_1} \in H^1(\hat{\Omega}_F)$ and $p = \hat{p}^{n_1} \in Q(\hat{\Omega}_F)$ such that

$$\left(\frac{\mathbf{u}-\mathbf{u}^n}{\vartheta\delta t}, \mathbf{v}\right)_{\hat{\Omega}_F} + \eta a(\mathbf{u}-\mathbf{w}; \mathbf{u}, \mathbf{v})_{\hat{\Omega}_F} - b(p, \mathbf{v})_n + b(q, \mathbf{u})_{\hat{\Omega}_F} = f(\mathcal{K}^{n_1}, \mathbf{v})_{\hat{\Omega}_F} - \tilde{\eta} a(\mathbf{u}^n - \mathbf{w}^n; \mathbf{u}^n, \mathbf{v}), \quad (3.12)$$

for all $\mathbf{v} \in V(\hat{\Omega}_F)$ and $q \in Q(\hat{\Omega}_F)$. Next, for given $\Omega(t_n)$, $T^n \in H^1(\Omega(t_n))$, $\mathbf{u}_T^n \in V(\Omega(t_n))$, $\mathbf{w}_T^n \in H^1(\Omega(t_n))$, $\mathbf{u}_T = \hat{\mathbf{u}}_T^{n_1}$ and $\mathbf{w}_T = \hat{\mathbf{w}}_T^{n_1}$, find $T = \hat{T}^{n_1} \in H^1(\hat{\Omega})$ such that

$$\left(\frac{T-T^n}{\vartheta\delta t}, g\psi\right)_{\hat{\Omega}} + \eta[a_T(\mathbf{u}_T - \mathbf{w}_T; T, \psi)_{\hat{\Omega}} + b_T(T, \psi)_{\hat{\Omega}}] = -\tilde{\eta}[a_T(\mathbf{u}_T^n; T^n, \psi) + b_T(T^n, \psi)]$$

for all $\phi \in H^1(\hat{\Omega})$. After solving the above equations, we move the boundary and the inner points to define the new domain $\Omega(t_{n_1})$.

Step 2.
For given $\Omega_F(t_{n_1})$, $T^{n_1} \in H^1(\Omega(t_{n_1}))$, $\mathbf{u}^{n_1} \in V(\Omega_F(t_{n_1}))$, $\mathbf{w}^{n_1} \in H^1(\Omega_F(t_{n_1}))$, find $\mathbf{u} = \hat{\mathbf{u}}^{n_2} \in V(\hat{\Omega}_F)$, $\mathbf{w} = \hat{\mathbf{w}}^{n_2} \in H^1(\hat{\Omega}_F)$and $p = \hat{p}^{n_2} \in Q(\hat{\Omega}_F)$ such that

$$\left(\frac{\mathbf{u}-\mathbf{u}^{n_1}}{\tilde{\vartheta}\delta t},\mathbf{v}\right)_{\hat{\Omega}_F} +\tilde{\eta}a(\mathbf{u}-\mathbf{w};\mathbf{u},\mathbf{v})_{\hat{\Omega}_F} - b(p,\mathbf{v})_{n_1} + b(q,\mathbf{u})_{\hat{\Omega}_F} = f(\mathcal{K}^{n_2},\mathbf{v})_{\hat{\Omega}_F} - \eta a(\mathbf{u}^{n_1}-\mathbf{w}^{n_1};\mathbf{u}^{n_1},\mathbf{v}), \tag{3.13}$$

for all $\mathbf{v} \in V(\hat{\Omega}_F)$ and $q \in Q(\hat{\Omega}_F)$. Similarly, as in step 1, for given $\Omega(t_{n_1})$, $T^{n_1} \in H^1(\Omega(t_{n_1}))$, $\mathbf{u}_T^{n_1} \in V(\Omega(t_{n_1}))$, $\mathbf{w}_T^{n_1} \in H^1(\Omega(t_{n_1}))$, $\mathbf{u}_T = \hat{\mathbf{u}}_T^{n_2}$ and $\mathbf{w}_T = \hat{\mathbf{w}}_T^{n_2}$, find $T = \hat{T}^{n_2} \in H^1(\hat{\Omega})$ such that

$$\left(\frac{T-T^{n_1}}{\vartheta\delta t},g\psi\right)_{\hat{\Omega}} + \tilde{\eta}[a_T(\mathbf{u}_T-\mathbf{w}_T;T,\psi)_{\hat{\Omega}} + b_T(T,\psi)_{\hat{\Omega}}] = -\eta[a_T(\mathbf{u}_T^{n_1};T^{n_1},\psi) + b_T(T^{n_1},\psi)]$$

for all $\psi \in H^1(\hat{\Omega})$. Here, $\hat{\Omega}$ is the ALE reference domain for the unknown domain $\Omega(t_{n_2})$.

Step 3.
For given $\Omega_F(t_{n_2})$, $T^{n_1} \in H^1(\Omega(t_{n_2}))$, $\mathbf{u}^{n_2} \in V(\Omega_F(t_{n_2}))$, $\mathbf{w}^{n_2} \in H^1(\Omega_F(t_{n_2}))$, find $\mathbf{u} = \hat{\mathbf{u}}^{n+1} \in V(\hat{\Omega}_F)$, $\mathbf{w} = \hat{\mathbf{w}}^{n+1} \in H^1(\hat{\Omega}_F)$and $p = \hat{p}^{n+1} \in Q(\hat{\Omega}_F)$ such that

$$\left(\frac{\mathbf{u}-\mathbf{u}^{n_2}}{\vartheta\delta t},\mathbf{v}\right)_{\hat{\Omega}_F} +\eta a(\mathbf{u}-\mathbf{w};\mathbf{u},\mathbf{v})_{\hat{\Omega}_F} - b(p,\mathbf{v})_{n_2} + b(q,\mathbf{u})_{n_2} = f(\mathcal{K}^{n_2},\mathbf{v})_{\hat{\Omega}_F} - \tilde{\eta} a(\mathbf{u}^{n_2}-\mathbf{w}^{n_2};\mathbf{u}^{n_2},\mathbf{v}), \tag{3.14}$$

for all $\mathbf{v} \in V(\hat{\Omega}_F)$ and $q \in Q(\hat{\Omega}_F)$. Finally, for given $\Omega(t_{n_2})$, $T^{n_2} \in H^1(\Omega(t_{n_2}))$, $\mathbf{u}_T^{n_2} \in V(\Omega(t_{n_2}))$, $\mathbf{w}_T^{n_2} \in H^1(\Omega(t_{n_2}))$, $\mathbf{u}_T = \hat{\mathbf{u}}_T^{n+1}$ and $\mathbf{w}_T = \hat{\mathbf{w}}_T^{n+1}$, find $T = \hat{T}^{n+1} \in H^1(\hat{\Omega})$ such that

$$\left(\frac{T-T^{n_2}}{\vartheta\delta t},g\psi\right)_{\hat{\Omega}} + \eta[a_T(\mathbf{u}_T-\mathbf{w}_T;T,\psi)_{\hat{\Omega}} + b_T(T,\psi)_{\hat{\Omega}}] = -\tilde{\eta}[a_T(\mathbf{u}_T^{n_2};T^{n_2},\psi) + b_T(T^{n_2},\psi)]$$

for all $\psi \in H^1(\hat{\Omega})$.

Remark: Note that, we treat the temperature in the Navier-Stokes equations explicitly. However, in the entire time interval (t^n, t^{n+1}) the temperature is not treated fully explicitly due to the splitting of the time step into sub-steps.

3.4 Axisymmetric formulation

We next derive the 3D-axisymmetric form of the variational form of the Navier-Stokes and energy equations. Since we derive the axisymmetric form from the variational form in 3D Cartesian coordinate, the boundary conditions are already incorporated in the axisymmetric form. The computational cost of 3D-axisymmetric model is significantly less in comparison with the 3D model, since a 2D geometric domain is used for 3D-axisymmetric computations.

Let $\Phi = \Phi_F \cup \Phi_S \cup \Gamma_{S_\Phi}$ be the meridian domain of Ω in 3D-axisymmetric configuration, see Figure 3.2. Here, Φ_F and Φ_S denote the meridian domain of the liquid and solid phases, respectively. Further, the liquid phase boundary is denoted by $\partial\Phi_F := \Gamma_{F_\Phi} \cup \Gamma_{S_\Phi} \cup \Gamma_{A_\Phi}$, where Γ_{F_Φ}, Γ_{S_Φ} and Γ_{A_Φ} denote the free surface, liquid-solid and axial boundaries, respectively. The solid phase boundary is denoted by $\partial\Phi_S = \Gamma_{S_\Phi} \cup \Gamma_{N_\Phi} \cup \Gamma_{A_\Phi}$.

Let $\mathbf{u}(x, y, z) = (u_1, u_2, u_3)$ and $\mathbf{u}_c(r, z, \phi) = (u_r, u_\phi, u_z)$ be the representation of velocity vector in the Cartesian and cylindrical coordinates, respectively, and

$$u_1 = u_r \cos\phi - u_\phi \sin\phi, \qquad u_2 = u_r \sin\phi - u_\phi \cos\phi, \qquad u_3 = u_z.$$

Here,

$$r(x, y) = \sqrt{x^2 + y^2} \quad \text{and} \quad \phi(x, y) = \arctan(y/x), \quad 0 \le \phi(x, y) < 2\pi.$$

We assume that the cylindrical velocity components u_r, u_ϕ, u_z are independent of ϕ and u_ϕ=0. Therefore, we have

$$\begin{aligned} u_1(x, y, z) &= u_r(r(x, y), z) \cos\phi(x, y), \\ u_2(x, y, z) &= u_r(r(x, y), z) \sin\phi(x, y), \\ u_3(x, y, z) &= u_z(r(x, y), z). \end{aligned} \tag{3.15}$$

Also, the scalar quantities (pressure and temperature) are not depend on ϕ, *i.e*, $p = p(r, z, t)$ and $T = T(r, z, t)$. Similarly for the test function $\mathbf{v} = (v_1, v_2, v_3)$, $\psi = \psi(x, y, z)$ and $q = q(x, y, z)$ we have

$$\begin{aligned} v_1(x, y, z) &= v_r \cos\phi, \qquad v_2(x, y, z) = v_r \sin\phi, \qquad v_3(x, y, z) = v_z, \\ q(x, y, z) &= q(r(x, y), z), \quad \psi(x, y, z) = \psi(r(x, y), z). \end{aligned} \tag{3.16}$$

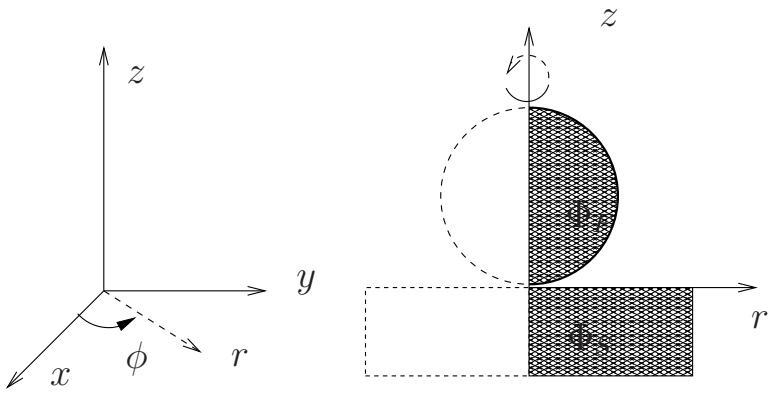

Figure 3.2: Initial computational meridian domain (shaded area) in 3D-axisymmetric configuration.

3.4.1 Axisymmetric form of the Navier–Stokes Equations

We consider the fully discrete form of the Navier–Stokes equations (3.8) with $\vartheta = 1$. Since the integral terms in the left-hand side of the Navier–Stokes equations are same in all temporal discretizations, it is enough to consider the case $\vartheta = 1$. The fully discrete form of the Navier–Stokes equations read:

For given $\Omega_F(t_n)$, $\mathbf{u}^n \in V(\Omega_F(t_n))$, $\mathbf{w}^n \in H^1(\Omega_F(t_n))$ and $\mathbf{w} = \mathbf{w}^{n+1}$, find $\mathbf{u} = \hat{\mathbf{u}}^{n+1} \in V(\hat{\Omega}_F)$, and $p = \hat{p}^{n+1} \in Q(\hat{\Omega}_F)$ such that

$$\left(\frac{\mathbf{u}-\mathbf{u}^n}{\delta t}, \mathbf{v}\right)_{\hat{\Omega}_F} + a(\mathbf{u}-\mathbf{w}; \mathbf{u}, \mathbf{v})_{\hat{\Omega}_F} - b(p, \mathbf{v})_{\hat{\Omega}_F} + b(q, \mathbf{u})_{\hat{\Omega}_F} = f(\mathcal{K}^{n+1}, \mathbf{v})_{\hat{\Omega}_F} \quad (3.17)$$

for all $\mathbf{v} \in V(\hat{\Omega}_F)$ and $q \in Q(\hat{\Omega}_F)$. Using (3.15) and (3.16), the 3D-axisymmetric form of the first integral term $(\mathbf{u}, \mathbf{v})$ in the above equation (3.17) can be written as

$$\begin{aligned}\iiint_{\hat{\Omega}_F} \mathbf{u}\cdot\mathbf{v}\ dx &= \int_0^{2\pi}\iint_{\Phi_F} (u_r v_r \cos^2\phi + u_r v_r \sin^2\phi + u_z v_z) r\, dr\, dz\, d\phi \\ &= 2\pi \iint_{\Phi_F} (u_r v_r + u_z v_z) r\, dr\, dz. \end{aligned} \quad (3.18)$$

Next, we consider

$$a(\hat{\mathbf{u}};\mathbf{u},\mathbf{v}) = \frac{2}{Re}\int_{\hat{\Omega}_F}\mathbb{D}(\mathbf{u}):\mathbb{D}(\mathbf{v})\;dx + \int_{\hat{\Omega}_F}(\hat{\mathbf{u}}\cdot\nabla)\mathbf{u}\cdot\mathbf{v}\;dx, \\ + \frac{1}{\beta_\epsilon}\int_{\Gamma_S}(\mathbf{u}\cdot\boldsymbol{\tau}_{i,S})(\mathbf{v}\cdot\boldsymbol{\tau}_{i,S})\;d\gamma_S$$

To derive the 3D-axisymmetric form of the velocity deformation tensor term in the above integral term, we first derive the 3D-axisymmetric form the velocity deformation tensor

$$\mathbb{D}(\mathbf{u}) = \frac{1}{2}\left(\frac{\partial u_i}{\partial x_j} + \frac{\partial u_j}{\partial x_i}\right), \qquad i,j = 1,2,3,$$

with $x_1 = x,\ x_2 = y,\ x_3 = z$. Using (3.15) and (3.16), the 3D-axisymmetric form of the partial derivatives of the velocity components become

$$\begin{aligned}
\frac{\partial u_1}{\partial x_1} &= \frac{\partial u_r}{\partial r}\frac{\partial r}{\partial x}\cos\phi - u_r\frac{\partial \phi}{\partial x}\sin\phi = \frac{\partial u_r}{\partial r}\cos^2\phi + u_r\frac{\sin^2\phi}{r},\\
\frac{\partial u_1}{\partial x_2} &= \frac{\partial u_r}{\partial r}\frac{y}{r}\cos\phi - u_r\frac{x}{r^2}\sin\phi = \left(\frac{\partial u_r}{\partial r} - \frac{u_r}{r}\right)\sin\phi\cos\phi,\\
\frac{\partial u_1}{\partial x_3} &= \frac{\partial u_r}{\partial z}\cos\phi,\\
\frac{\partial u_2}{\partial x_1} &= \frac{\partial u_r}{\partial r}\frac{x}{r}\sin\phi - u_r\frac{y}{r^2}\cos\phi = \left(\frac{\partial u_r}{\partial r} - \frac{u_r}{r}\right)\sin\phi\cos\phi,\\
\frac{\partial u_2}{\partial x_2} &= \frac{\partial u_r}{\partial r}\frac{y}{r}\sin\phi + u_r\frac{x}{r^2}\cos\phi = \frac{\partial u_r}{\partial r}\sin^2\phi + u_r\frac{\cos^2\phi}{r},\\
\frac{\partial u_2}{\partial x_3} &= \frac{\partial u_r}{\partial z}\sin\phi,\\
\frac{\partial u_3}{\partial x_1} &= \frac{\partial u_z}{\partial r}\frac{x}{r} = \frac{\partial u_z}{\partial r}\cos\phi,\\
\frac{\partial u_3}{\partial x_2} &= \frac{\partial u_z}{\partial r}\frac{y}{r} = \frac{\partial u_z}{\partial r}\sin\phi,\\
\frac{\partial u_3}{\partial x_3} &= \frac{\partial u_z}{\partial z}.
\end{aligned} \tag{3.19}$$

Therefore, we have

$$\mathbb{D}(\mathbf{u}) =$$

$$\begin{bmatrix} \dfrac{\partial u_r}{\partial r}\cos^2\phi + u_r\dfrac{\sin^2\phi}{r}, & \left(\dfrac{\partial u_r}{\partial r} - \dfrac{u_r}{r}\right)\sin\phi\cos\phi, & \left(\dfrac{\partial u_r}{\partial z} + \dfrac{\partial u_z}{\partial r}\right)\dfrac{\cos\phi}{2} \\ \left(\dfrac{\partial u_r}{\partial r} - \dfrac{u_r}{r}\right)\sin\phi\cos\phi, & \dfrac{\partial u_r}{\partial r}\sin^2\phi + u_r\dfrac{\cos^2\phi}{r}, & \left(\dfrac{\partial u_r}{\partial z} + \dfrac{\partial u_z}{\partial r}\right)\dfrac{\sin\phi}{2} \\ \left(\dfrac{\partial u_r}{\partial z} + \dfrac{\partial u_z}{\partial r}\right)\dfrac{\cos\phi}{2} & \left(\dfrac{\partial u_r}{\partial z} + \dfrac{\partial u_z}{\partial r}\right)\dfrac{\sin\phi}{2} & \dfrac{\partial u_z}{\partial z} \end{bmatrix},$$

Thus, the 3D-axisymmetric tensor product of the velocity deformation tensor becomes,

$$\begin{aligned} \mathbb{D}(\mathbf{u}) : \mathbb{D}(\mathbf{v}) = \; & \frac{\partial u_r}{\partial r}\frac{\partial v_r}{\partial r}\left(\cos^4\phi + 2\sin^2\phi\cos^2\phi + \sin^4\phi\right) \\ & + \frac{\partial u_r}{\partial r}\frac{v_r}{r}\left(\sin^2\phi\cos^2\phi - 2\sin^2\phi\cos^2\phi + \sin^2\phi\cos^2\phi\right) \\ & + \frac{\partial v_r}{\partial r}\frac{u_r}{r}\left(\sin^2\phi\cos^2\phi - 2\sin^2\phi\cos^2\phi + \sin^2\phi\cos^2\phi\right) \\ & + \frac{u_r v_r}{r^2}\left(+\sin^4\phi + 2\sin^2\phi\cos^2\phi\cos^4\phi\right) \\ & + \frac{1}{2}\left(\frac{\partial u_r}{\partial z} + \frac{\partial u_z}{\partial r}\right)\left(\frac{\partial v_r}{\partial z} + \frac{\partial v_z}{\partial r}\right)\left(\cos^2\phi + \sin^2\right) + \frac{\partial u_z}{\partial z}\frac{\partial v_z}{\partial z} \\ = \; & \frac{\partial u_r}{\partial r}\frac{\partial v_r}{\partial r} + \frac{u_r v_r}{r^2} + \frac{1}{2}\left(\frac{\partial u_r}{\partial z} + \frac{\partial u_z}{\partial r}\right)\left(\frac{\partial v_r}{\partial z} + \frac{\partial v_z}{\partial r}\right) + \frac{\partial u_z}{\partial z}\frac{\partial v_z}{\partial z}. \end{aligned}$$

Hence, the 3D-axisymmetric form of the tensor product $(\mathbb{D}(\mathbf{u}) : \mathbb{D}(\mathbf{v}))$ becomes:

$$\iiint_{\hat{\Omega}_F} \mathbb{D}(\mathbf{u}) : \mathbb{D}(\mathbf{v}) \; dx$$

$$\begin{aligned} = 2\pi \iint_{\Phi_F} \Bigg[& \frac{\partial u_r}{\partial r}\frac{\partial v_r}{\partial r} + \frac{u_r v_r}{r^2} + \frac{1}{2}\left(\frac{\partial u_r}{\partial z} + \frac{\partial u_z}{\partial r}\right)\left(\frac{\partial v_r}{\partial z} + \frac{\partial v_z}{\partial r}\right) \\ & + \frac{\partial u_z}{\partial z}\frac{\partial v_z}{\partial z}\Bigg] r \, dr \, dz. \end{aligned} \tag{3.20}$$

Next, the nonlinear term in the Navier-Stokes equation can be written as

$$\sum_{i,j=1}^{3} u_i \frac{\partial u_j}{\partial x_i} v_j$$

$$\begin{aligned}
&= u_r \cos\phi \left(\frac{\partial u_r}{\partial r} \cos^2\phi + u_r \frac{\sin^2\phi}{r} \right) v_r \cos\phi \\
&\quad + u_r \cos\phi \left(\frac{\partial u_r}{\partial r} - \frac{u_r}{r} \right) \sin\phi\cos\phi \; v_r \sin\phi \\
&\quad + u_r \cos\phi \frac{\partial u_z}{\partial r} \cos\phi \; v_z + u_r \sin\phi \left(\frac{\partial u_r}{\partial r} - \frac{u_r}{r} \right) \sin\phi\cos\phi \; v_r \cos\phi \\
&\quad + u_r \sin\phi \left(\frac{\partial u_r}{\partial r} \sin^2\phi + u_r \frac{\cos^2\phi}{r} \right) v_r \sin\phi + u_r \sin\phi \frac{\partial u_z}{\partial r} \sin\phi \; v_z \\
&\quad + u_z \frac{\partial u_r}{\partial z} \cos\phi \; v_r \cos\phi + u_z \frac{\partial u_r}{\partial z} \sin\phi \; v_r \sin\phi + u_z \frac{\partial u_z}{\partial z} v_z \\
&= u_r \frac{\partial u_r}{\partial r} v_r \left(\cos^4\phi + 2\sin^2\phi\cos^2\phi + \sin^4\phi \right) \\
&\quad + \frac{u_r^2 v_r}{r} \left(2\sin^2\phi\cos^2\phi - 2\cos^2\phi\sin^2\phi \right) + u_r \frac{\partial u_z}{\partial r} v_z \left(\cos^2\phi + \sin^2 \right) \\
&\quad + u_z \frac{\partial u_r}{\partial z} v_r \left(\cos^2\phi + \sin^2 \right) + u_z \frac{\partial u_z}{\partial z} v_z \\
&= u_r \frac{\partial u_r}{\partial r} v_r + u_r \frac{\partial u_z}{\partial r} v_z + u_z \frac{\partial u_r}{\partial z} v_r + u_z \frac{\partial u_z}{\partial z} v_z .
\end{aligned}$$

Hence, the 3D-axisymmetric form of the convective term in (3.17) becomes

$$\begin{aligned}
&\iiint_{\hat{\Omega}_F} ((\mathbf{u} - \mathbf{w}) \cdot \nabla \mathbf{u}) \cdot \mathbf{v} \, dx \\
&\qquad = 2\pi \iint_{\Phi_F} \Bigg[\left((u_r - w_r) \frac{\partial u_r}{\partial r} + (u_z - w_z) \frac{\partial u_r}{\partial z} \right) v_r \\
&\qquad\quad + \left((u_r - w_r) \frac{\partial u_z}{\partial r} + (u_z - w_z) \frac{\partial u_z}{\partial z} \right) v_z \Bigg] r \, dr \, dz .
\end{aligned}$$

Here, w_r, w_z are the mesh velocity components in Φ_F. Next, we derive the 3D-axisymmetric form of the liquid-solid interface integral term. We have the two tangential vectors

$$\boldsymbol{\tau}_1 = (\cos\phi, \ \sin\phi, \ 0) \qquad \boldsymbol{\tau}_2 = (-\sin\phi, \ \cos\phi, \ 0)$$

on the liquid-solid interface Γ_S. Further, we have

$$\begin{aligned}
&\mathbf{u}\cdot\boldsymbol{\tau}_1 = u_r\cos^2\phi + u_r\sin^2\phi, \qquad \mathbf{v}\cdot\boldsymbol{\tau}_1 = v_r,\\
&\mathbf{u}\cdot\boldsymbol{\tau}_2 = u_r(-\sin\phi\cos\phi + \cos\phi\sin\phi), \qquad \mathbf{v}\cdot\boldsymbol{\tau}_2 = 0.
\end{aligned}$$

Hence,

$$\int_{\Gamma_S}(\mathbf{u}\cdot\boldsymbol{\tau}_{i,S})(\mathbf{v}\cdot\boldsymbol{\tau}_{i,S})\,d\gamma_= \int\!\!\int_{\Gamma_S}(\mathbf{u}\cdot\boldsymbol{\tau}_1\,\mathbf{v}\cdot\boldsymbol{\tau}_1+\mathbf{u}\cdot\boldsymbol{\tau}_2\,\mathbf{v}\cdot\boldsymbol{\tau}_2)\;ds = 2\pi\int_{\Gamma_{S_\Phi}} u_r v_r r\,dr.$$

For the bilinear form $b(p,\nabla\cdot\mathbf{v})_{\hat{\Omega}_F}$ in (3.17), we have

$$\begin{aligned}
b(p,\nabla\cdot\mathbf{v})_{\hat{\Omega}_F} &= \int\!\!\int\!\!\int_{\hat{\Omega}_F}\left(p,\frac{\partial v_1}{\partial x_1}+\frac{\partial v_2}{\partial x_2}+\frac{\partial v_3}{\partial x_3}\right)dx\\
&= 2\pi\int\!\!\int_{\Phi_F}\left[p\left(\frac{\partial v_r}{\partial r}+\frac{1}{r}v_r+\frac{\partial v_z}{\partial z}\right)\right]r\,dr\,dz.
\end{aligned}$$

We now consider the right hand side term in (3.17)

$$\begin{aligned}
f(\mathcal{K},\mathbf{v}) \;&= \frac{1}{Fr}\int_{\hat{\Omega}_F}\mathbf{e}\cdot\mathbf{v}\;dx - \frac{1}{We}\int_{\Gamma_{F_t}}\underline{\nabla}id_{\Gamma_{F_t}} : [M_{T_F}\underline{\nabla}\mathbf{v}+\mathbf{v}\otimes\underline{\nabla}M_{T_F}]\,d\gamma_F\\
&+\frac{1}{We}\int_{\zeta_t}\cos(\theta)\;M_{T_F}\mathbf{v}\cdot\boldsymbol{\tau}_S\;d\zeta\\
&-\frac{\mathcal{C}_1}{\sigma_{sa}We}\int_{\Gamma_F}(\mathbf{v}\cdot\boldsymbol{\tau}_{i,F})(\boldsymbol{\tau}_{i,F}\cdot\nabla T_F)\;d\gamma_F.
\end{aligned} \tag{3.21}$$

Now, let us derive the 3D-axisymmetric form for each of the above integral terms. Since $\mathbf{e}=(0,0,-1)$, the first integral term becomes

$$\int\!\!\int\!\!\int_{\hat{\Omega}_F}\mathbf{e}\cdot\mathbf{v}\;dx = -2\pi\int\!\!\int_{\Phi_F} v_z r\,dr\,dz.$$

We now derive the 3D-axisymmetric form for the second integral term in (3.21)

$$\begin{aligned}
&\int_{\Gamma_{F_t}}\underline{\nabla}id_{\Gamma_{F_t}} : [M_{T_F}\underline{\nabla}\mathbf{v}+\mathbf{v}\otimes\underline{\nabla}M_{T_F}]\,d\gamma_F\\
&\quad= \int_{\Gamma_{F_t}} M_{T_F}\;\underline{\nabla}id_{\Gamma_{F_t}} : \underline{\nabla}\mathbf{v}\,d\gamma_F + \int_{\Gamma_{F_t}}\underline{\nabla}id_{\Gamma_{F_t}} : \mathbf{v}\otimes\underline{\nabla}M_{T_F}\,d\gamma_F
\end{aligned} \tag{3.22}$$

Let $\boldsymbol{\nu}_F = n_j$ be the outward normal in the cross section Φ_F. The normal on the surface generated by rotation of the curve around the $z - axis$ has the representation

$$\boldsymbol{\nu}_F = (n_1 \cos\phi,\ n_1 \sin\phi,\ n_2).$$

We know that from (2.24)

$$\underline{\nabla} id = \delta_{i,j} - n_i n_j, \qquad \underline{\nabla}\mathbf{v} = \frac{\partial v_i}{\partial x_j} - \frac{\partial v_i}{\partial \boldsymbol{n}} n_j, \qquad \text{for, } i,j = 1,2,3.$$

Therefore, we have

$$\begin{aligned}
\underline{\nabla} id_{\Gamma_F} : \underline{\nabla}\mathbf{v} &= (\delta_{i,j} - n_i n_j)\left(\frac{\partial v_i}{\partial x_j} - \frac{\partial v_i}{\partial \boldsymbol{n}} n_j\right) \\
&= \sum_{i,j=1}^{3} \left\{ \delta_{i,j}\frac{\partial v_i}{\partial x_j} - \delta_{i,j}\frac{\partial v_i}{\partial \boldsymbol{n}} n_j - \frac{\partial v_i}{\partial x_j} n_i n_j + \frac{\partial v_i}{\partial \boldsymbol{n}} n_j n_i n_j \right\} \\
&= \nabla \cdot \mathbf{v} - \sum_{i=1}^{3} \frac{\partial v_i}{\partial \boldsymbol{n}} n_i.
\end{aligned}$$

We know that $\nabla \cdot \mathbf{v} = \dfrac{\partial v_r}{\partial r} + \dfrac{v_r}{r} + \dfrac{\partial v_z}{\partial z}$. Further, we have

$$\sum_{i,j=1}^{3} n_j \frac{\partial v_i}{\partial x_j} n_i = (n_1 \cos\phi, n_1 \sin\phi, n_2)\ A\ \ (n_1 \cos\phi, n_1 \sin\phi, n_2)^T,$$

where

$$A = \sum_{i,j=1}^{3} \frac{\partial v_i}{\partial x_j} = \begin{bmatrix}
\dfrac{\partial v_r}{\partial r}\cos^2\phi + v_r\dfrac{\sin^2\phi}{r}, & \left(\dfrac{\partial v_r}{\partial r} - \dfrac{v_r}{r}\right)\sin\phi\cos\phi, & \dfrac{\partial v_r}{\partial z}\cos\phi \\
\left(\dfrac{\partial v_r}{\partial r} - \dfrac{v_r}{r}\right)\sin\phi\cos\phi, & \dfrac{\partial v_r}{\partial z}\sin^2\phi + v_r\dfrac{\cos^2\phi}{r}, & \dfrac{\partial v_r}{\partial z}\sin\phi \\
\dfrac{\partial v_r}{\partial z}\cos\phi, & \dfrac{\partial v_r}{\partial z}\sin\phi, & \dfrac{\partial v_z}{\partial z}
\end{bmatrix}.$$

Therefore, we have

$$\begin{aligned}\sum_{i,j=1}^{3} n_j \frac{\partial v_i}{\partial x_j} n_i =& n_1 \cos^2\phi \left[n_1 \frac{\partial v_r}{\partial r} + n_2 \frac{\partial v_r}{\partial z} \right] + n_1 \sin^2\phi \left[n_1 \frac{\partial v_r}{\partial r} + n_2 \frac{\partial v_r}{\partial z} \right] \\ &+ n_2 \left[n_1 \frac{\partial v_z}{\partial r} + n_2 \frac{\partial v_z}{\partial z} \right] \\ =& n_1 \left[n_1 \frac{\partial v_r}{\partial r} + n_2 \frac{\partial v_r}{\partial z} \right] + n_2 \left[n_1 \frac{\partial v_z}{\partial r} + n_2 \frac{\partial v_z}{\partial z} \right].\end{aligned}$$

Using (3.19) the first term in (3.22) becomes

$$\begin{aligned}&\int\int_{\Gamma_{F_t}} M_{T_F}\, \underline{\nabla} id_{\Gamma_{F_t}} : \underline{\nabla}\mathbf{v}\, d\gamma_F \\ &= 2\pi \int_{\Gamma_{F_\Phi}} M_{T_F} \left(\frac{\partial v_r}{\partial r} + \frac{v_r}{r} + \frac{\partial v_z}{\partial z} - n_1 \left[n_1 \frac{\partial v_r}{\partial r} + n_2 \frac{\partial v_r}{\partial z} \right] \right. \\ &\qquad \left. - n_2 \left[n_1 \frac{\partial v_z}{\partial r} + n_2 \frac{\partial v_z}{\partial z} \right] \right)\, r\, ds.\end{aligned}$$

Next, let us consider the second integral term on the right hand side of the equation (3.22). We first define

$$\mathbf{v} \otimes \underline{\nabla} M_{T_F} = -\frac{\mathcal{C}_1}{\sigma_{sa}} \left[\mathbf{v} \otimes (\nabla T_F - (\boldsymbol{n} \cdot \nabla T_F)\boldsymbol{n}) \right]$$

Using the above derivations, the second integral term on the right hand side of the equation (3.22) becomes

$$\begin{aligned}&\int\int_{\Gamma_{F_t}} \underline{\nabla} id_{\Gamma_{F_t}} : \mathbf{v} \otimes \underline{\nabla} M_{T_F}\, d\gamma_F \\ &= \frac{\mathcal{C}_1}{\sigma_{sa}} 2\pi \int_{\Gamma_{F_\Phi}} \left\{ [(1 - n_1 n_1)\mathbf{I}_1 - n_1 n_2 \mathbf{I}_2] v_r + [(1 - n_2 n_2)\mathbf{I}_2 - n_1 n_2 \mathbf{I}_1] v_z \right\} r\, ds,\end{aligned}$$

where

$$\mathbf{I}_1 = \frac{\partial T}{\partial r} - n_1 \left[n_1 \frac{\partial T}{\partial r} + n_2 \frac{\partial T}{\partial z} \right], \qquad \mathbf{I}_2 = \frac{\partial T}{\partial z} - n_2 \left[n_1 \frac{\partial T}{\partial r} + n_2 \frac{\partial T}{\partial z} \right]$$

Next, we consider the contact angle integral term

$$\int_{\zeta} M_{T_f} \mathbf{v} \cdot \tau_S \cos\theta\, d\zeta$$

in (3.21). Here, ζ denotes the contact line, θ the contact angle, and τ_S the scaled projection of the surface normal ν_F onto the plane Γ_S

$$\tau_S = \frac{\nu_F - (\nu_F \cdot \nu_S)\nu_S}{|\nu_F - (\nu_F \cdot \nu_S)\nu_S|}.$$

Consider the axisymmetric case and a plane surface Γ_S with $\nu_S = (0, 0, 1)$. The parametrization of the contact line ζ can be written in the form

$$x = r_0 \cos\varphi, \quad y = r_0 \sin\varphi, \quad z = 0, \qquad 0 \le \varphi \le 2\pi.$$

Let in the (r, z) cross section the unit normal to Γ_S and Γ_F, respectively, be denoted by $n_S = (0, 1)$ and $n_F = (n_r, n_z)$. Then, $\nu_F = (n_r \cos\varphi, n_r \sin\varphi, n_z)$ A short computation gives

$$\nu_F - (\nu_F \cdot \nu_S)\nu_S = (n_r \cos\varphi, n_r \sin\varphi, 0) \quad \Rightarrow \quad \tau_S = (\cos\varphi, \sin\varphi, 0).$$

Taking into consideration that $\mathbf{v} = (v_r \cos\varphi, v_r \sin\varphi, v_z)$ we obtain

$$\int_\zeta M_{T_f} \mathbf{v} \cdot \tau_S \cos\theta \, d\zeta = \left(2\pi r M_{T_f} \cos\theta\right) \; v_r\Big|_{\zeta_{cp}},$$

where ζ_{cp} denotes the moving contact point. Note that all terms in the 3D axisymmetric formulation contain the factor 2π, i.e. we could devide through 2π and implement the term above without this factor. Further, the axial boundary, *i.e.*, at $r = 0$, is an artificial boundary, and we require a boundary condition to solve this problem in axisymmetric configuration. It can be derived as

$$\left.\frac{\partial u_z}{\partial r}\right|_{r=0} = 0, \quad u_r = 0,$$

and it leads to different spaces for the two velocity components, see [26] for more details. For the wellposedness of the axisymmetric form using the weighted Sobolev spaces see [3, 63].

3.4.2 Axisymmetric form of the energy equation

To derive the axisymmetric form of the energy equation, we consider the fully discrete form (3.9) with $\vartheta = 1$. It reads:

For given $\Omega(t_n)$, $T^n \in H^1(\Omega(t_n))$, $\mathbf{u}_T^n \in V(\Omega(t_n))$, $\mathbf{w}_T^n \in H^1(\Omega(t_n))$, $\hat{\mathbf{u}}_T^{n+1}$ and $\hat{\mathbf{w}}_T^{n+1}$, find $\hat{T}^{n+1} \in H^1(\hat{\Omega})$ such that

$$\left(\frac{\hat{T}^{n+1}-T^n}{\delta t}, g\psi\right)_{\hat{\Omega}} + a_T(\hat{\mathbf{u}}_T^{n+1}-\hat{\mathbf{w}}_T^{n+1},\hat{T}^{n+1},\phi)_{\hat{\Omega}} + b_T(\hat{T}^{n+1},\phi)_{\hat{\Omega}} = 0 \qquad (3.23)$$

We have

$$T(x,y,z) = T(r(x,y),z), \quad \frac{\partial T}{\partial x} = \frac{\partial T}{\partial r}\cos\phi, \quad \frac{\partial T}{\partial y} = \frac{\partial T}{\partial r}\sin\phi, \quad \frac{\partial T}{\partial z} = \frac{\partial T}{\partial z},$$

$$\psi(x,y,z) = \psi(r(x,y),z), \quad \frac{\partial \psi}{\partial x} = \frac{\partial \psi}{\partial r}\cos\phi, \quad \frac{\partial \psi}{\partial y} = \frac{\partial \psi}{\partial r}\sin\phi, \quad \frac{\partial \psi}{\partial z} = \frac{\partial \psi}{\partial z}.$$

Using the above relation, the axisymmetric form of the the bilinear form $(T, g\psi)$ (3.23) becomes

$$\iiint_\Omega gT\psi \; dx = 2\pi \iint_\Phi gT\psi \; r \; dr \; dz.$$

Next, We first consider

$$a_T(\mathbf{u}_T - \mathbf{w}_T, T, \psi) = \int_\Omega \frac{1}{Pe} \; \nabla T \cdot \nabla \psi \; dx + \int_\Omega (\mathbf{u}_T - \mathbf{w}_T) \cdot \nabla T \; \psi \; dx.$$

in (3.23). The axisymmetric form of the diffusion term becomes

$$\iiint_\Omega \frac{1}{Pe} \nabla T \cdot \nabla \psi \; dx = 2\pi \iint_\Phi \frac{1}{Pe} \left(\frac{\partial T}{\partial r}\frac{\partial \psi}{\partial r} + \frac{\partial T}{\partial z}\frac{\partial \psi}{\partial z}\right) \; r \; dr \; dz.$$

and the convective term becomes

$$\iiint_\Omega (\mathbf{u}_T - \mathbf{w}_T) \cdot \nabla T \psi \; dx = 2\pi \iint_\Phi \left[(u_{r,T} - w_{r,T})\frac{\partial T}{\partial r} + (u_{z,T} - w_{z,T})\frac{\partial T}{\partial z}\right] \; \psi \; r \; dr \; dz,$$

where $u_{r,T}$, $u_{z,T}$ and $w_{r,T}$, $w_{z,T}$ are the fluid and mesh velocity components in Φ. Finally, the axisymmetric form of the bilinear form b_T in (3.23) becomes

$$b_T(T,\psi) = Bi \int_{\Gamma_F} \frac{1}{Pe} \; T \; \psi \; dx = 2\pi Bi \int_{\Gamma_{F_\Phi}} \frac{1}{Pe} \; T \; \psi \; r \; ds.$$

Also for the energy equation the axial boundary, *i.e.*, at $r = 0$, is an artificial boundary, and it can be derived as

$$\left.\frac{\partial T}{\partial \boldsymbol{n}}\right|_{r=0} = 0.$$

4 Numerical methods for moving meshes

The impinging droplet changes its shape over time. Its boundary consists of a free surface and the liquid-solid interface. Both parts of the boundary are changing with time. Thus, a given fixed mesh in the solid domain does not fit to the changing mesh along the liquid-solid interface. In section 4.1 we discuss methods to overcome this difficulty. The Mortar finite element method as a tool to handle non-matching grids has not been used, instead the already for the fluid domain applied ALE-approach has been favorite. In the ALE approach the mesh points on the free surface are moved with the fluid velocity. The displacement of the inner mesh points can be arbitrary, and one could also use the fluid velocity. However, this often leads to quick distortions of the mesh and a remeshing becomes necessary to preserve the mesh quality. Thus, we are interested to move the inner mesh points in a prescribed way which guarantees a certain mesh quality. In section 4.2 we explain two different techniques: the harmonic extension and the elastic mesh update. The displacement of the inner points can be prescribed using either the harmonic extension or the linear elastic solid technique.

4.1 Mesh handling at the liquid-solid interface

In the droplet deformation problem, the free surface vertices adjacent to the contact line may reach the solid surface during the droplet spreading. Further, the vertices on the liquid-solid interface can move in the tangential direction due to the slip with friction boundary condition. If the mesh in the solid domain is fixed this leads to non-matching grid along the liquid-solid interface. The liquid-solid interface can be handled by either a non-matching or a matching grid. In the non-matching grid, it is enough to find the displacement of the liquid domain and the mesh velocity in the solid phase will be zero. In the matching grid, the displacement of the solid mesh also has to be calculated due to the movement of the vertices on the liquid-solid interface. Thus, the mesh velocity will be non-zero in

solid phase which will induce the mesh velocity convection term in the energy equation of the solid phase. To handle the non-matching grid at the liquid-solid interface, the mortar finite element method can be used, whereas no special method is needed in the case of matching grid.

4.1.1 Mortar finite element method

Mortar finite element method is a discretization method for partial differential equations on nonmatching grids and it has been first introduced in [4]. The mortar finite element discretization is a discontinuous Galerkin approximation. The functions in the approximation subspaces have jumps across subdomain interfaces and are standard finite element functions when restricted to the subdomains. The mortar finite element method is classified as a nonconforming finite element method due to the discontinuity on the interface. In the non-overlapping subdomains, the subdomain meshes do not match at the interface, and the continuity of the solution is enforced weakly by Lagrange multipliers.

As mentioned early, the vertices on the liquid-solid interface of the impinging droplet problem move in the tangential direction due to the slip with friction boundary condition. Thus, the pattern of the unfitted mesh at the liquid-solid interface changes at every time step. Therefore, the matrix structure changes at every time step and it is very challenging. Hence, we prefer the mesh adaptive method to handle the liquid-solid interface.

4.1.2 Mesh adaptive method

We present the implemented mesh manipulation when a free surface vertex reaches the solid surface. At every time step, after moving the mesh we calculate the distance between solid surface and the free surface vertex adjacent to the solid surface. If the distance is less than 10^{-8} or if the free surface vertex is penetrated into the solid surface, we do the following steps before proceeding to the next time step:

- Move the free surface vertex perpendicularly to the solid surface and change its type to a contact line (point) vertex. Here, we could move the free surface vertex using the fluid velocity but the vertex is already very close (10^{-8}) to the solid surface and for simplicity we move it perpendicularly to the solid surface.

- Delete the free surface edge and the solid edge on which the free surface vertex incident.

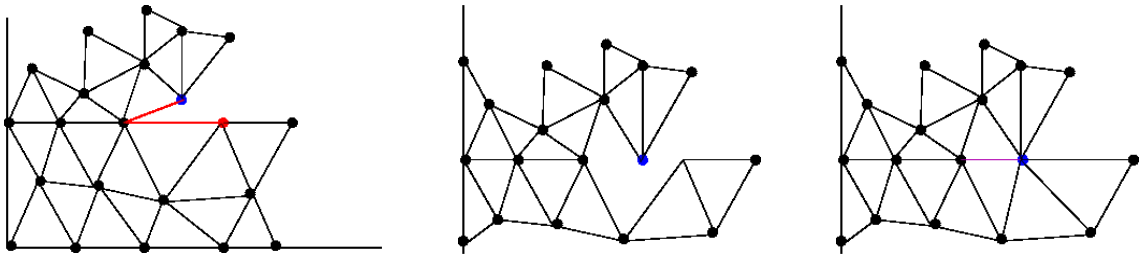

Figure 4.1: Mesh adaptive method.

- Reconnect all edged associated with the right side vertex of the solid edge to the moving contact line vertex.

- Generate a new liquid-solid interface joint with the old and the new contact line vertices.

- Construct new finite element spaces for the velocity, pressure and temperature on the manipulated mesh.

- Map the solution from the old finite element functions to the new functions without interpolation.

- Set the normal component of the velocity to zero for the degrees of freedom associated with the newly generated liquid-solid interface joint (imposing the no penetration condition).

- For the temperature degrees of freedom on the newly generated liquid-solid interface joint, we take the average value from the free surface values and the solid surface values.

The above steps are presented in Figure 4.1. Due to the above mesh manipulation approach, the mesh at the liquid-solid interface remains fitted and thus no mortar technique is needed. But, due to the tangential movement of the liquid-solid vertices, the displacement of inner points in the solid phase has to be calculated and this induces a mesh velocity convection term in the energy equation of the solid phase. Next, we describe the harmonic extension and the linear elastic solid techniques in detail for computing the inner mesh displacement in both liquid and solid phases.

4.2 Free surface and interface tracking

We track the free surface using the arbitrary Lagrangian-Eulerian approach, see Section 2.3. In the ALE approach, the free surface is tracked explicitly using the fluid velocity. This can be done by using the fluid velocity directly or the normal component of it in the normal direction. For given $\mathbf{X}^n$ and $\mathbf{u}(\mathbf{X}, s),\ s \in (t_n, t_{n+1})$, find $\mathbf{X}(t_{n+1})$ such that

$$\frac{d\mathbf{X}}{ds} = \mathbf{u}(\mathbf{X}, s). \tag{4.1}$$

Here, $\mathbf{u}$ is the fluid velocity. Alternatively, we can also use the equation

$$\frac{d\mathbf{X}^*}{ds} = (\mathbf{u}(\mathbf{X}, s) \cdot \boldsymbol{\nu}) \cdot \boldsymbol{\nu} \tag{4.2}$$

to obtain the new position of the boundary/free surface. The following lemma shows that both are equivalent.

Lemma 4.2.1 (see, Lemma 5.2.1 in [22]) *Let $\mathbf{u} = \mathbf{u}(\mathbf{X}, s)$ be the divergence free velocity, that is, $\nabla \cdot \mathbf{u} = 0$, in a moving time-dependent domain $\Omega_F(s) \in \mathbb{R}^2$ and $\Gamma(s) = \partial\Omega_F(s)$. Let $\boldsymbol{\nu}$ be the outward unit normal vector on $\Gamma(s)$ Then,*

$$\frac{d\mathbf{X}}{ds} = \mathbf{u}(\mathbf{X}, s), \quad \mathbf{X}(0, \gamma) = \mathbf{X}_0(\gamma),\ \gamma \in P \tag{4.3}$$

and

$$\frac{d\mathbf{X}^*}{ds} = (\mathbf{u}(\mathbf{X}^*, s) \cdot \boldsymbol{\nu}) \cdot \boldsymbol{\nu}, \quad \mathbf{X}^*(0, \gamma) = \mathbf{X}_0(\gamma),\ \gamma \in P \tag{4.4}$$

are equivalent and both preserve volume of $\Omega_F(s)$.

We note that even though the equations (4.1) and (4.2) are equivalent and both preserve volume in the continuous form, the discrete form of these equations will provide different positions of the boundary/free surface points. In [1, 48], the free surface in the oscillation droplet has been updated using (4.2), that is, the new position of the free surface is obtained by applying the backward Euler scheme to (4.2)

$$\mathbf{X}^{n+1} = \mathbf{X}^n + \delta t \left(\mathbf{u}^{n+1} \cdot \boldsymbol{\nu}\right) \boldsymbol{\nu}. \tag{4.5}$$

Update of this type avoids the tangential movement of the boundary points, and therefore the accumulation of the boundary points at certain regions

of the boundary is avoided. However, the update only in the normal direction may not be applicable to all cases. Thus, we prefer to move the boundary/free surface with full velocity approximating (4.1) as follows

$$\mathbf{X}^{n+1} = \mathbf{X}^n + \delta t \mathbf{u}^{n+1}. \tag{4.6}$$

After updating the boundary points, the position of the inner points are updated according to the displacement of the boundary mesh points.

Remark: The mesh points on the liquid-solid interface will also get updated while using the relation (4.1). Since we use the adaptive mesh at the liquid-solid interface between the liquid and solid phases, the solid phase mesh calls adjacent to the liquid-solid interface get distorted due to the movement of mesh points on the liquid-solid interface. In order to avoid quick distortion, we update also the inner points of the solid phase according the displacement of the liquid-solid interface mesh points. It eventually induce a mesh velocity convection term in the energy equation of the solid phase.

4.2.1 Harmonic extension

At each time step, the new position of the moving mesh in the harmonic extension is obtained by solving the following Laplace problem. Let Υ^n be the displacement of the boundary $\partial\hat{\Omega}(t_n)$ at time $t = t_n$. Then, the displacement Ψ^n of the mesh $\hat{\Omega}(t_n)$ at $t = t_n$ is obtained by solving

$$\Delta\Psi^{n+1} = 0 \text{ in } \hat{\Omega}(t_n), \qquad \Psi^{n+1} = \Upsilon^n \text{ on } \partial\hat{\Omega}(t_n). \tag{4.7}$$

Let $W^n := H^1(\hat{\Omega}(t_n))^2$ and $W_0^n := \{\varphi \in W \ : \ \varphi = 0 \text{ on } \partial\hat{\Omega}(t_n)\}$ be the usual Sobolev spaces. Then, the discrete form of (4.7) reads:

Find $\Psi_h^{n+1} \in W_h^n$ such that

$$\int_{\hat{\Omega}_h(t_n)} \nabla\Psi_h^{n+1} \ \nabla\varphi_h = 0 \quad \text{for all } \varphi_h \ \in W_{h,0}^n, \tag{4.8}$$
$$\Psi_h^{n+1}(\mathbf{x}) = \Upsilon^n(\mathbf{x}) \quad \text{for all } \mathbf{x} \in \partial\hat{\Omega}_h(t_n).$$

Since it is enough to find the displacement of the vertices, linear finite elements are sufficient to solve the above equation on the existing mesh in the original domain $\Omega_h(t_n)$. Note that, if we use a fixed reference domain

(may be the initial domain $\Omega(0)$) in the entire computation, then the matrix of the discrete problem (4.8) does not change in time, and thus the matrix has to be assembled only once in an entire computation. However, the boundary values in (4.7) will be different in each time step, and thus the system has to be solved in each time step.

The harmonic extension is well suitable for those domains, which remain convex in all times or the deviation from the convex is not too large. Next, we discuss the linear elasticity technique, which preserves the mesh quality better than the harmonic extension.

4.2.2 Elastic mesh update

In the elastic mesh update, we calculate the displacement vectors subject to the displacement of the boundary in each time step. The displacement vector Ψ^n in the domain $\hat{\Omega}(t_n)$ is obtained by solving linear elasticity equations. For a given boundary displacement Υ^n, find the displacement $\Psi^n \in W_h^n$ such that

$$\begin{aligned} \nabla \cdot \mathbb{S}(\Psi^n) &= 0 \quad \text{in } \hat{\Omega}(t_n) \\ \Psi^n &= \Upsilon^n \quad \text{on } \partial\hat{\Omega}(t_n) \end{aligned} \tag{4.9}$$

where

$$\mathbb{S}(\phi) = \lambda_1(\nabla \cdot \phi)\mathbb{I} + 2\lambda_2\mathbb{D}(\phi).$$

Here, λ_1 and λ_2 are Lame constants. To solve problem (4.9) by a finite element method, we use the same triangulation $\mathcal{T}_h$ of the domain which has been used for the flow variables. The discrete form of the equation (4.9) is derived in an usual way, and it reads:

Find $\Psi_h^n \in W_h^n$ such that $\Psi_h^n = \Upsilon_h^n$ on $\partial\hat{\Omega}_h(t_n)$ and

$$\int_{\hat{\Omega}_h(t_n)} \mathbb{D}(\Psi_h^n) : \mathbb{D}(\phi) + C_1 \int_{\hat{\Omega}_h(t_n)} \nabla \cdot \Psi_h^n \; \nabla \cdot \phi = 0, \quad \forall\, \phi \in W_{h,0}^n(\hat{\Omega}_h(t_n)). \tag{4.10}$$

Here $C_1 = \lambda_1/\lambda_2$ is a positive constant, which in all our calculations $C_1 = 1$. The solution of (4.10) is approximated by the continuous piecewise linear P_1 triangular finite element as it is enough to find the displacement of the vertices. We refer to [48] for a-priori bounds and the regularity requirements of mappings in (4.10).

4.2.3 Mesh velocity

The mesh velocity **w** on the boundaries will be equal to the fluid velocity, since we use the relation (4.6) to move the boundary mesh points. Therefore, the convection term in the Navier-Stokes and energy equations will become zero on the boundaries. The mesh velocity in the inner mesh is calculated using the displacement vector, which is obtained from either (4.7) or (4.9).

4.2.4 Remeshing and re-parametrization

The quality of the moving finite element mesh may become poor at some point during the computations and a remeshing is needed. Therefore, an automatic remeshing algorithm has been implemented to remesh the domain, when the quality of the mesh becomes very poor, say if the minimum angle in the triangulation is less than 10°. During the remeshing the boundary mesh points are provided to the mesh generator, Triangle [67], which outputs a new mesh. Then we construct new finite element spaces and interpolate the current solution from the old mesh to the new mesh. After that we continue our computations.

Over a period of time, the mesh points on the free surface and other boundary parts may accumulate or become coarse at some regions. This cannot be averted even by remeshing, since during the remeshing the boundary mesh points are provided to the mesh generator as the input and it is not altered during mesh generation. Therefore, a special technique is needed to redistribute these boundary points. We achieve the redistribution by a re-parametrization technique. In our approach, we check the minimum and maximum arc length between boundary mesh points while moving the mesh at each time step. If the minimum or the maximum arc length exceeds the prescribed limit, we uniformly redistribute the boundary mesh points using interpolated cubic splines.

4.3 Calculating the heat flow across Liquid-Solid interface

In this section, we present an algorithm for calculating the heat flow from the solid phase to the liquid phase based on the ideas given in [32] for calculating the lift and drag coefficients in viscous flows. We explain the

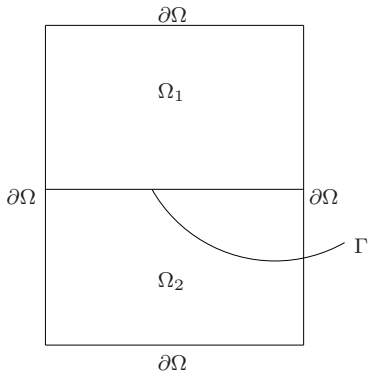

Figure 4.2: .

method for a simple fixed domain situation indicated in Figure 4.2. Assume that Ω_1 and Ω_2 are open and bounded, and denote $\Gamma = \partial\Omega_1 \cap \partial\Omega_2$. Then $\Omega := \Omega_1 \cup \Omega_2 \cup \Gamma$ is also open and bounded, and $\partial\Omega \cap \Gamma = \emptyset$. We consider the following problem:

$$\begin{aligned}
\frac{\partial u_i}{\partial t} - \nabla \cdot (\lambda_i \nabla u) &= f_i && \text{in } \Omega_i, \qquad i = 1, 2, \\
u_1 &= u_2 && \text{on } \Gamma \\
\lambda_1 \frac{\partial u_1}{\partial n} &= \lambda_2 \frac{\partial u_2}{\partial n} && \text{on } \Gamma \\
\lambda_i \frac{\partial u_i}{\partial n} &= 0 && \text{on } \partial\Omega_i \setminus \Gamma \\
u_i(0) &= u_{i,0} && \text{in } \Omega_i.
\end{aligned} \tag{4.11}$$

For this model, we want to compute the heat flow from Ω_2 to Ω_1 the weak form of (4.11) reads:

Find $u : (0, T] \to H^1(\Omega)$ such that

$$\begin{aligned}
(u_t, v) + (\lambda \nabla u(t), \nabla v) &= (f(t), v) \quad \forall\ v \in H^1(\Omega) \\
(u(0), v) &= (u_0, v) \quad \forall\ v \in L^2(\Omega).
\end{aligned} \tag{4.12}$$

Here the brackets $(\cdot, \cdot)$ denote the inner product in $L^2(\Omega)$ and $u_t = \dfrac{\partial u}{\partial t}$. In the following we show under additional regularity assumption that (4.12) follows from (4.13). Testing first by functions from $C_0^\infty(\Omega_1)$ and applying integration by parts (which is possible if the solution u is smooth enough) we get

$$(u_t, v)_{\Omega_1} - \operatorname{div}(\lambda \nabla u(t), v)_{\Omega_1} = (f(t), v) \quad \forall\ v \in C_0^\infty(\Omega_1).$$

Since $C_0^\infty(\Omega_1)$ is dense in $L^2(\Omega_1)$ we conclude

$$u_t - \operatorname{div}(\lambda \nabla u(t)) = f(t) \quad \text{in} \quad \Omega_1.$$

Similarly by testing with $v \in C_0^\infty(\Omega_2)$ we have

$$u_t - \operatorname{div}(\lambda \nabla u(t)) = f(t) \quad \text{in} \quad \Omega_2.$$

Further, let $v \in H^1(\Omega)$ and applying integration by parts on each subdomain separately, we obtain

$$\begin{aligned}(u_t, v)_{\Omega_1} + (u_t, v)_{\Omega_2} - (\lambda \nabla u(t), \nabla v)_{\Omega_1} - (\lambda \nabla u(t), \nabla v)_{\Omega_2} \\ + \int_{\partial\Omega_1 \setminus \Gamma} \lambda_1 \frac{\partial u_1}{\partial n}\ v\ d\gamma + \int_{\partial\Omega_2 \setminus \Gamma} \lambda_2 \frac{\partial u_2}{\partial n}\ v\ d\gamma + \int_\Gamma \left(\lambda_1 \frac{\partial u_1}{\partial n_\Gamma} - \lambda_2 \frac{\partial u_2}{\partial n_\Gamma}\right)\ v\ d\gamma \\ = (f(t), v)_{\Omega_1} + (f(t), v)_{\Omega_2}.\end{aligned}$$

Because $u = u_i$ in Ω_i satisfies the partial differential equation in each subdomain Ω_i, the equation simplifies to

$$\int_{\partial\Omega_1 \setminus \Gamma} \lambda_1 \frac{\partial u_1}{\partial n}\ v\ d\gamma + \int_{\partial\Omega_2 \setminus \Gamma} \lambda_2 \frac{\partial u_2}{\partial n}\ v\ d\gamma + \int_\Gamma \left(\lambda_1 \frac{\partial u_1}{\partial n_\Gamma} - \lambda_2 \frac{\partial u_2}{\partial n_\Gamma}\right)\ v\ d\gamma = 0$$

for all $v \in H^1(\Omega)$. Now, restricting to H^1- functions

(i) with $v\Big|_{\partial\Omega} = 0$ we get $\quad \lambda_1 \dfrac{\partial u_1}{\partial n_\Gamma} = \lambda_2 \dfrac{\partial u_2}{\partial n_\Gamma}$ along Γ,

(ii) with $v\Big|_{\partial\Omega_2} = 0$ we get $\quad \lambda_1 \dfrac{\partial u_1}{\partial n} = 0$ along $\partial\Omega_1 \setminus \Gamma$,

(iii) with $v\Big|_{\partial\Omega_1} = 0$ we get $\quad \lambda_2 \dfrac{\partial u_2}{\partial n} = 0$ along $\partial\Omega_2 \setminus \Gamma$,

the weak formulation of (4.12) results into the equivalent form of the strong formulation.

$$\begin{aligned}\frac{\partial u_i}{\partial t} - \operatorname{div}(\lambda_i \nabla u_i) &= f_i \text{ in } \Omega_i \\ \lambda_i \frac{\partial u_i}{\partial n} &= 0 \text{ on } \partial\Omega_i \setminus \Gamma \\ u_i(0) &= u_{0i} \text{ in } \Omega_i\end{aligned} \tag{4.13}$$

with the coupling condition $u_1 = u_2,\ \lambda_1 \dfrac{\partial u_1}{\partial n_\Gamma} = \lambda_2 \dfrac{\partial u_2}{\partial n_\Gamma}$ on Γ.
Note that $u_1 = u_2$ follows from the assumption that $u \in H^1(\Omega)$ and for the restrictions $u_i = u\Big|_{\Omega_i}$ have the same trace on Γ. In case $f \equiv 0$ we have no heat sources or heat sinks, i.e. energy is conserved (since no heat flow over the boundary of Ω). Mathematically, we see this by setting $v = 1$ such that

$$\begin{aligned}(u_t, 1) &= \frac{d}{dt}\int_\Omega u dx = 0\\ (u(0), 1) &= (u_0, 1).\end{aligned}$$

Now, we compute the heat flow over Γ in (t^n, t^{n+1})

$$Q := \int_{t^n}^{t^{n+1}} \int_\Gamma \lambda_1 \frac{\partial u_1}{\partial n_\Gamma}\, d\gamma = \int_{t^n}^{t^{n+1}} \int_{\partial\Omega_1} \lambda_1 \frac{\partial u_1}{\partial n}\, d\gamma \tag{4.14}$$

since $\dfrac{\partial u_1}{\partial n}\Big|_{\partial\Omega_1\setminus\Gamma} = 0$. Then, u_1 can be considered to be the solution of the Dirichlet problem in Ω_1

$$\begin{aligned}\frac{\partial u}{\partial t} - \mathrm{div}\lambda_1 \nabla u &= f \text{ in } \Omega_1\\ u(0) &= u_0 \text{ in } \Omega_1\\ u &= u_1 \text{ on } \partial\Omega_1.\end{aligned} \tag{4.15}$$

Note that u_1 on $\partial\Omega_1$ is known as the trace of the solution of problem (4.12). Now, multiplying (4.15) by $v \in H^1(\Omega_1)$ and integrating by parts we get

$$\left(\frac{\partial u_1}{\partial t}, v\right)_{\Omega_1} + (\lambda_1 \nabla u_1, \nabla v)_{\Omega_1} - \int_{\partial\Omega_1} \lambda_1 \frac{\partial u_1}{\partial n} v\, d\gamma = (f, v)_{\Omega_1}.$$

Thus, the quantity

$$\int_{\partial\Omega_1} \lambda_1 \frac{\partial u_1}{\partial n}\, d\gamma = \left(\frac{\partial u_1}{\partial t}, v\right)_{\Omega_1} + (\lambda_1 \nabla u_1, \nabla v)_{\Omega_1} - (f, v)_{\Omega_1}$$

is independent of the special choice of $v \in \{w \in H^1(\Omega_1) : w = 1 \text{ on } \partial\Omega_1\}$. Now integrating over (t^n, t^{n+1}), we get

$$\begin{aligned}Q &:= \int_{t^n}^{t^{n+1}} \int_{\partial\Omega_1} \lambda_1 \frac{\partial u_1}{\partial n} \gamma\, dt\\ &= (u_1^{n+1} - u_1^n, v)_{\Omega_1} + \int_{t^n}^{t^{n+1}} \left[(\lambda_1 \nabla u_1, \nabla v)_{\Omega_1} - (f, v)_{\Omega_1}\right] dt.\end{aligned}$$

In order to simplify the computation one chooses in the discrete case a function v_h with small support and $v_h \equiv 1$ on $\partial\Omega_1$

$$Q := (u_{1h}^{n+1} - u_{1h}^{n}, v_h)_{\Omega_1} + \delta t \left[(\lambda_1 \nabla u_{1h}^{n+1}, \nabla v_h)_{\Omega_1} - (f^{n+1}, v_h)_{\Omega_1} \right].$$

Let $\varphi_1, \varphi_2, ..., \varphi_N$ be the basis function associated with the inner nodes of Ω_1 and indices from N+1 to N+M be the basis functions associated with the boundary $\partial\Omega_1$ nodes. Then, with v_h as above and

$$u_{1h} = \sum_{j=1}^{N+M} u_j \varphi_j \qquad v_h = \sum_{i=N+1}^{N+M} \varphi_i.$$

Note that $v_h \equiv 1$ at all boundary nodes on $\partial\Omega_1$ and $v_h \equiv 0$ at all inner nodes in Ω_1. Thus, we get

$$Q_h = \sum_{i=N+1}^{N+M} \sum_{j=1}^{N+M} \{(u_j^{n+1} - u_j^n)(\varphi_j, \varphi_i)_{\Omega_1} + \delta t u_j^{n+1} (\lambda_1 \nabla \varphi_j, \nabla \varphi_i)_{\Omega_1}\} - \sum_{i=N+1}^{N+M} \delta t (f^{n+1}, \varphi_i)_{\Omega_1}.$$

As we can see that to calculate the heat flow we only need the mass matrix, the stiffness matrix and the right hand side which have been generated already in the assembling process. From the generated matrices $M = (\varphi_j, \varphi_i)_{\Omega_1}$, $A = (\lambda_1 \nabla \varphi_j, \nabla \varphi_i)_{\Omega_1}$ and the right hand side $F = (f, \varphi_i)_{\Omega_1}$, we compute the row vectors

$$m = \left(\varphi_j, \sum_{i=N+1}^{N+M} \varphi_i \right)_{\Omega_1} = \sum_{i=N+1}^{N+M} (\varphi_j, \varphi_i)_{\Omega_1}$$

$$a = \left(\lambda \nabla \varphi_j, \nabla \sum_{i=N+1}^{N+M} \varphi_i \right)_{\Omega_1} = \sum_{i=N+1}^{N+M} (\lambda \nabla \varphi_j, \nabla \varphi_i)_{\Omega_1}$$

$$s = \left(f, \sum_{i=N+1}^{N+M} \varphi_i \right)_{\Omega_1} = \sum_{i=N+1}^{N+M} (f, \varphi_i)_{\Omega_1}$$

by summing the corresponding columns in the matrices M, A and F. Note that the row vectors have to be calculated before doing any manipulation

for imposing boundary conditions. Finally, we compute the heat flow as

$$Q_h = (u^{n+1} - u^n) \cdot m + \delta t u^{n+1} \cdot a + s. \tag{4.16}$$

Note that the basis functions on the liquid-solid interface have support on both the liquid and the solid phases. However, to evaluate Q_h we need the contribution only from one side, and thus we always take the support of the basis functions from the solid phase.

5 Numerical results

In this section we study the heat transfer in the droplet and the influence of the heat transfer on the fluid flow. The main focus of this study is to illustrate that our numerical scheme captures the behavior of heat transfer effects on the flow dynamics. In our model, the surface tension is considered as a function of temperature. Further the Marangoni convection is included in the model.

All computations in this Chapter are performed until the dimensionless end time $T = 25$ with the time step 1×10^{-4}. Further, the initial liquid and solid computational domains contains 1716 and 705 cells, respectively. The number of degrees of freedom (unknowns) for the velocity, the pressure and the temperature in the initial domain are 7474, 1011, and 5234, respectively. Note that these numbers may change during the remeshing. Finally, in each time step we stop the fixed point iteration of the Navier–Stokes equation when the residual of the system matrix becomes less than 10^{-7} or the number of fixed point iteration reaches ten. However, often the iteration converges within three or four iterations due to the choice of small time step.

5.1 Influence of Reynolds number

To study the influence of the Reynolds number on the flow dynamics of a liquid droplet impinging on a hot solid surface, we consider a droplet of diameter $d_0 = 2.7 \times 10^{-3}$ m. Further, the following material parameters are used: the density $\rho = 1000\,\mathrm{kg/m^3}$, the dynamic viscosity $\mu = 0.001\,\mathrm{N\,s/m^2}$, the surface tension $\sigma_{ref} = 0.073$ N/m, the equilibrium contact angle $\theta_e = 30°$. Also, we assume that $u_{imp} = 1.54$ m/s, $T_{F,0} = 298°$K, $T_{S,0} = 328°$K, $T_\infty = 298°$K, $T_{ref} = 323°$K (temperature of the fluid surface, the solid surface, the atmospheric and the reference, respectively). Using L $= r_0$ and U $= u_{imp}$ as characteristic values, we get $Re = 2079$, $We = 43$, $Fr = 179$, $Pe_F = 10$, $Pe_S = 100$, $Bi = 0.000058$ for the considered material parameters. In order to study the influence of the Reynolds number, we considered four variants: (i) $Re = 260$, (ii) $Re = 520$, (iii) $Re = 1040$ and

(iv) $Re = 2079$ by varying the viscosity μ.

Re	$W_{d_{max}}$	t at $W_{d_{max}}$	$M_{F_{max}}$
260	3.3345	7.5193	0.27
520	3.7197	7.6858	0.43
1040	4.1493	8.0056	0.27
2079	4.6282	8.3409	0.42

Table 5.1: Maximum dimensionless wetting diameter $W_{d_{max}}$ and time taken to attain it for different Reynolds number, $We = 43$ and $Fr = 179$.

The computationally obtained sequence of droplets in Var (i) and Var (iv) at difference instances (dimensionless time) $t = 0.1,\ 1.0,\ 8.0,\ 16,\ 25.$ are depicted in Figure 5.1. The colours in the pictures represent the temperature distribution during the droplet deformation over time. Initially, the dimensionless temperature in the droplet is zero, whereas the temperature in the solid is 1.2143. In the high Reynolds number case, Var (iv), the wetting diameter of the droplet is more, and thus it covers more solid surface and absorb more heat from the solid surface. The total heat from the solid phase to the liquid phase will be studies in the Sections 5.3 and 5.5.

Next, the obtained wetting diameter and the dynamic contact angle in all four variants over time are presented in Figure 5.2. As we expected, the wetting diameter increases with the Reynolds number. The maximum wetting diameter and the time taken to obtain it are presented in Figure 5.3. We can observe that the maximum wetting diameter is non-linear with respect to the Reynolds number. A similar behaviour is observed in the time taken to attain the maximum wetting diameter. The dynamic contact angle in all four variants reach the equilibrium value almost after the dimensionless time $t = 10$, see Figure 5.2. Further, the relative mass loss is calculated using

$$M_F = \frac{\left|\Omega_0 - \Omega_t\right|}{\left|\Omega_0\right|} \times 100\%$$

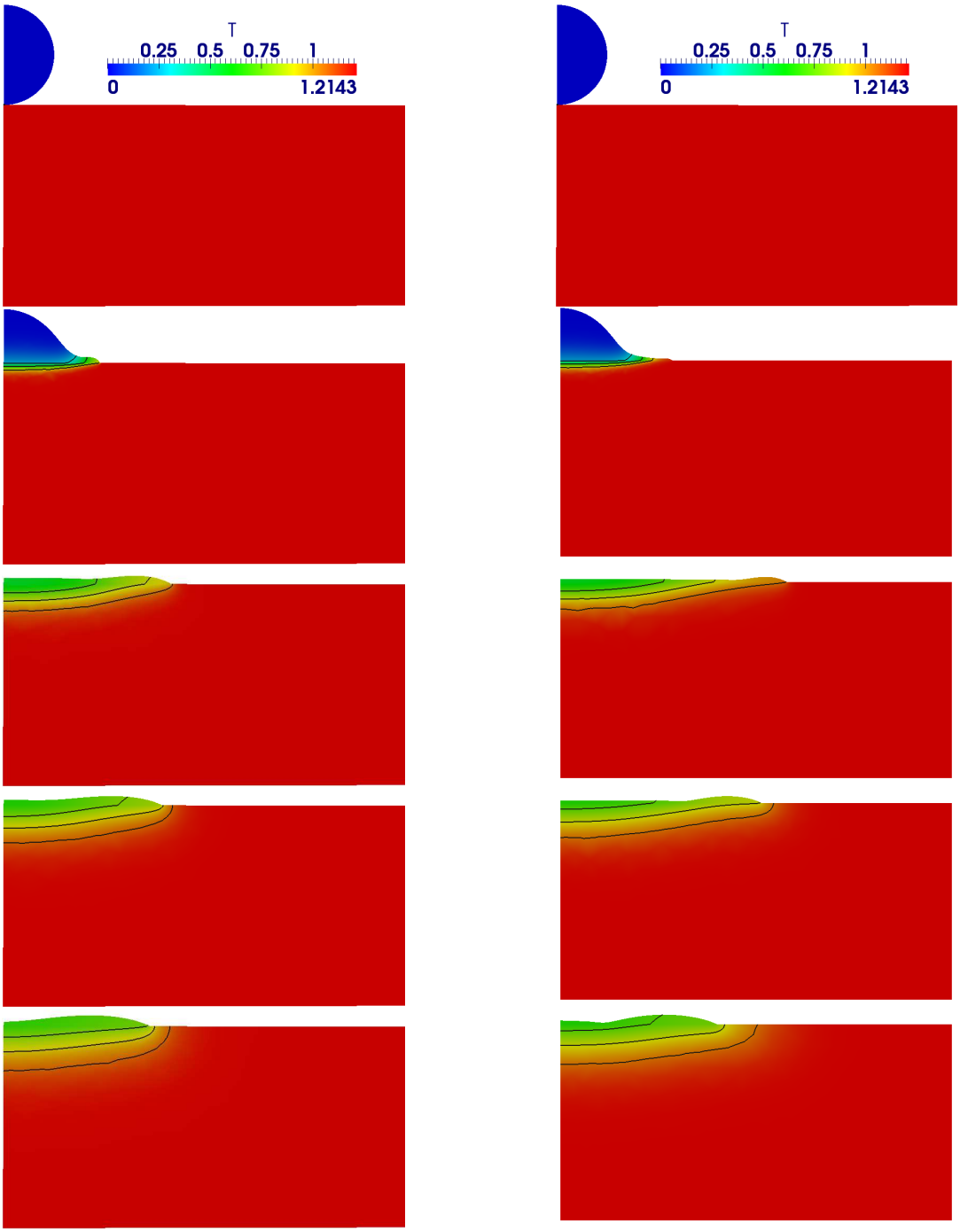

Var (i) Var (iv)

Figure 5.1: Sequence of images obtained in different simulations of a liquid droplet impinging on a hot solid surface with $\theta_e = 30°$, $We = 43$, $Fr = 179$. Var (i) $Re = 260$, Var (iv) $Re = 2079$. The dimensionless timing from the top: $t = 0.1,\ 1.0,\ 8.0,\ 16,\ 25$.

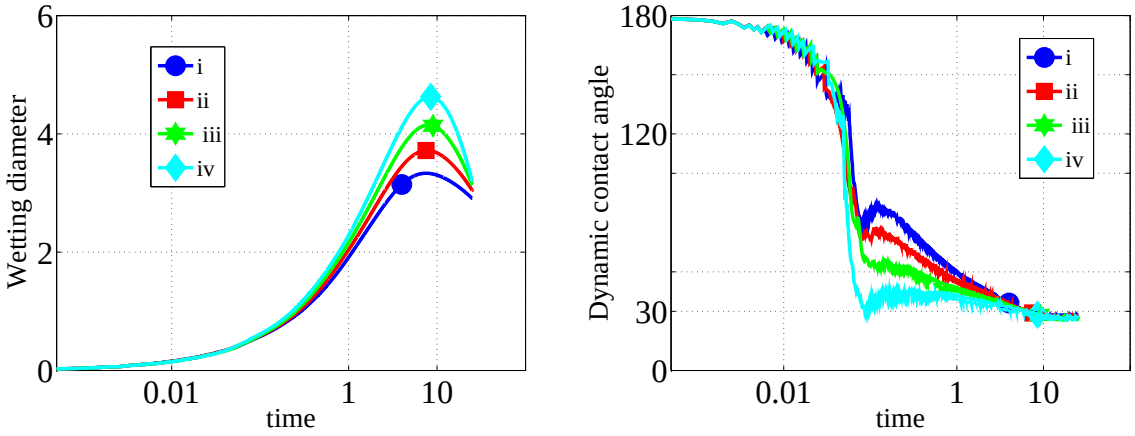

Figure 5.2: Wetting diameter (left) and the dynamic contact angle (right) of a liquid droplet with $\theta_e = 30°$, $We = 43$ and $Fr = 179$, impinging on a hot solid surface. (i) $Re = 260$, (ii) $Re = 520$, (iii) $Re = 1040$, (iv) $Re = 2079$.

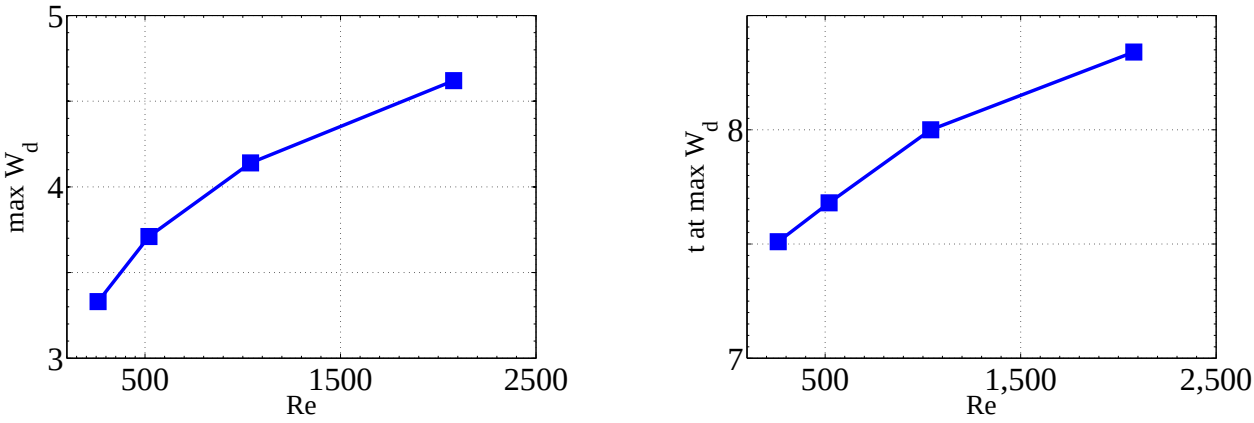

Figure 5.3: Maximal wetting diameter (left) and the time to attain it (right) for different Reynolds number with fixed $We = 43$ for a liquid droplet.

as a function of time, where $|\Omega_t|$ denotes the volume of Ω_t at time t. It is observed that the relative mass loss in the liquid droplet occurs in Var (iv), and it is 0.42%, see Table 5.1.

5.2 Influence of Weber number

To study the influence of the surface tension on the flow dynamics, we vary the Weber number and fix other dimensionless numbers. We consider the

following four variants: (i) $We = 43$, (ii) $We = 90$, (iii) $We = 140$, and (iv) $We = 190$ by varying the surface tension. Further, we used the fixed numbers $Re = 2079$, $Fr = 179$ and $Bi = 0.000058$ in all variants. Also, we set the equilibrium contact angle $\theta_e = 30°$, $T_F = 298°$K, $T_S = 328°$K, $T_\infty = 298°$K, $T_{ref} = 323°$K. The Sequence of images obtained for the variants (i) and (ii) at difference instances are depicted in Figure 5.4. The colours represent the temperature distribution in both the liquid and solid phases.

Next, the computationally obtained wetting diameter and dynamic contact angle over time for all four variants are presented in Figure 5.5. Since the surface tension will be large in the var (i), the maximum wetting diameter is expected to be small. As we expected, the maximum wetting diameter increases when the Weber number increase. The dynamic contact angle in all four variants reach the equilibrium value almost after the dimensionless time $t = 1$. However, more oscillations have been observed in the variant (iv). Since the surface tension coefficient is very small (less rigid) in variant (iv), more rolling motion is observed while spreading.

Next, the maximum wetting diameter and the time taken to obtain it are presented in Figure 5.6. As in the Reynolds number case, the maximum wetting diameter is non-linear with respect to the Weber number also, see Figure 5.6. Further, the maximum relative mass loss in the liquid droplet is 0.4% and it occurred in Var (iv).

We	$W_{d_{max}}$	t at $W_{d_{max}}$	$M_{F_{max}}$
43	4.6273	8.3962	0.27
90	4.7638	9.8043	0.43
140	4.8371	10.6426	0.27
190	4.8776	11.2594	0.42

Table 5.2: Maximum dimensionless wetting diameter $W_{d_{max}}$ and time taken to attain it for different Weber number $Re = 2079$ and $Fr = 179$.

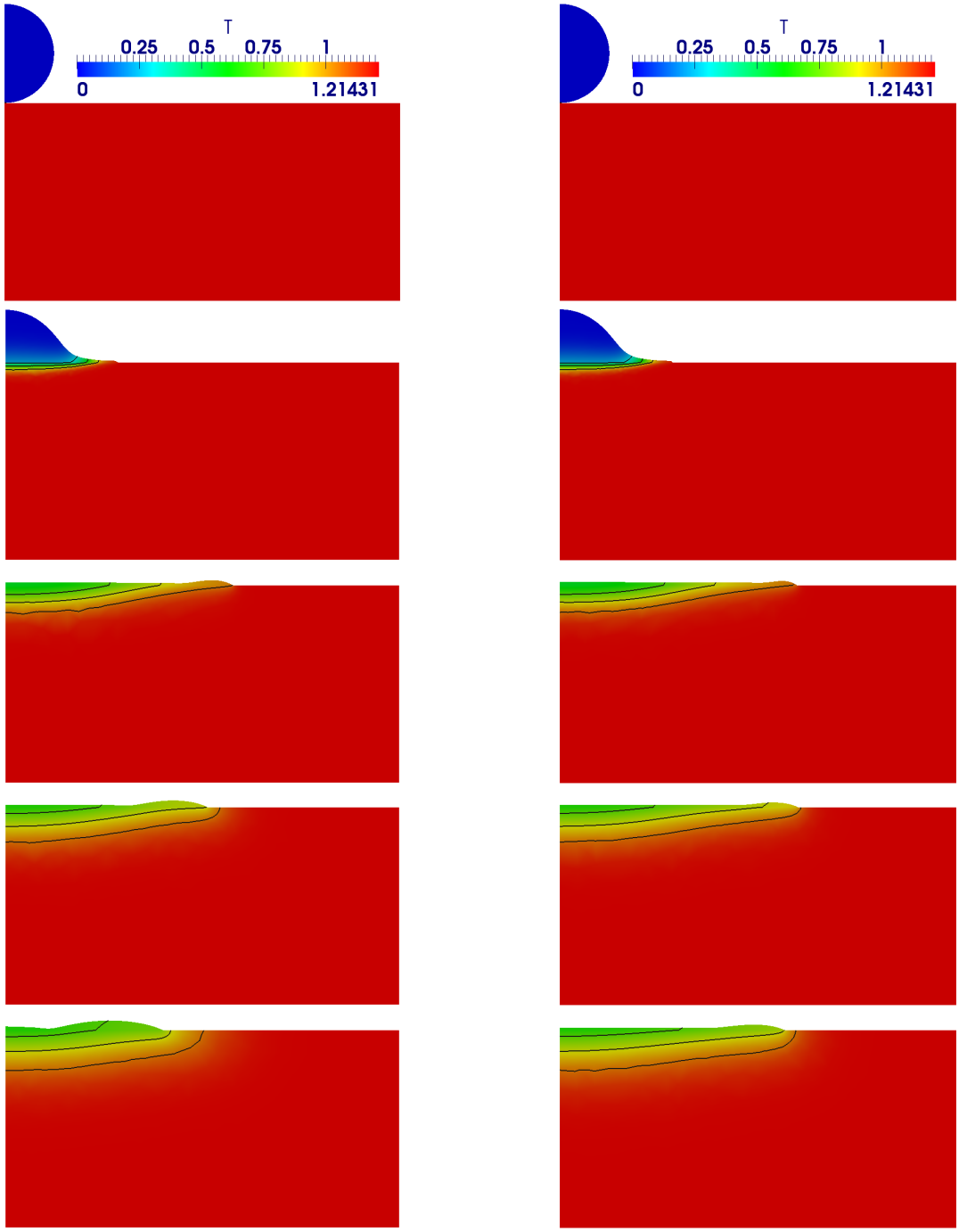

case (i) case (ii)

Figure 5.4: Sequence of images obtained in different simulations of a liquid droplet impinging on a hot solid surface with $\theta_e = 30°$, $Re = 2079$, $Fr = 179$ (i) $We = 43$, (ii) $We = 190$. Timing from the top: t = 0.1, 1.0, 8.0, 16, 25.

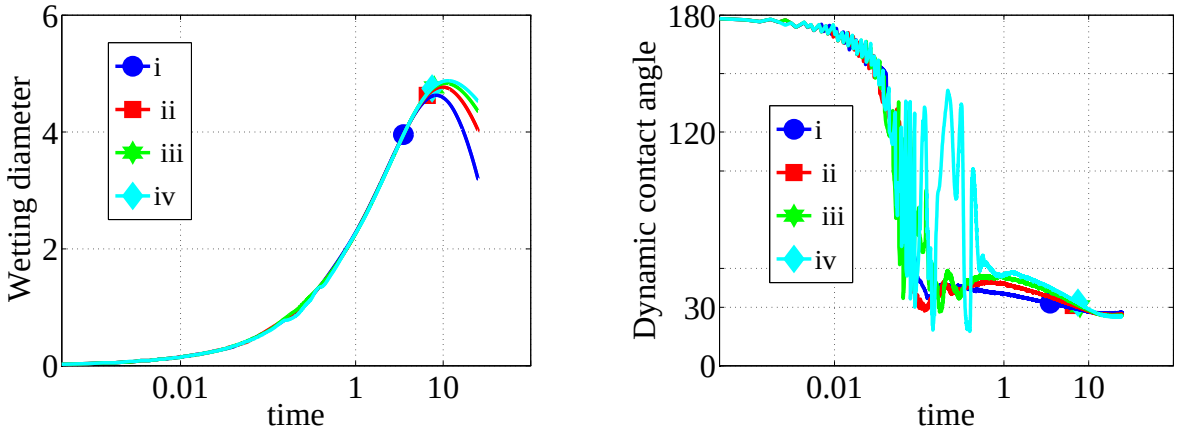

Figure 5.5: Wetting diameter (left) and the dynamic contact angle (right) of a liquid droplet with $\theta_e = 30°$, $Re = 2079$ and $Fr = 179$, impinging on a hot solid surface. (i) $We = 43$, (ii) $We = 90$, (iii) $We = 140$, (iv) $We = 190$.

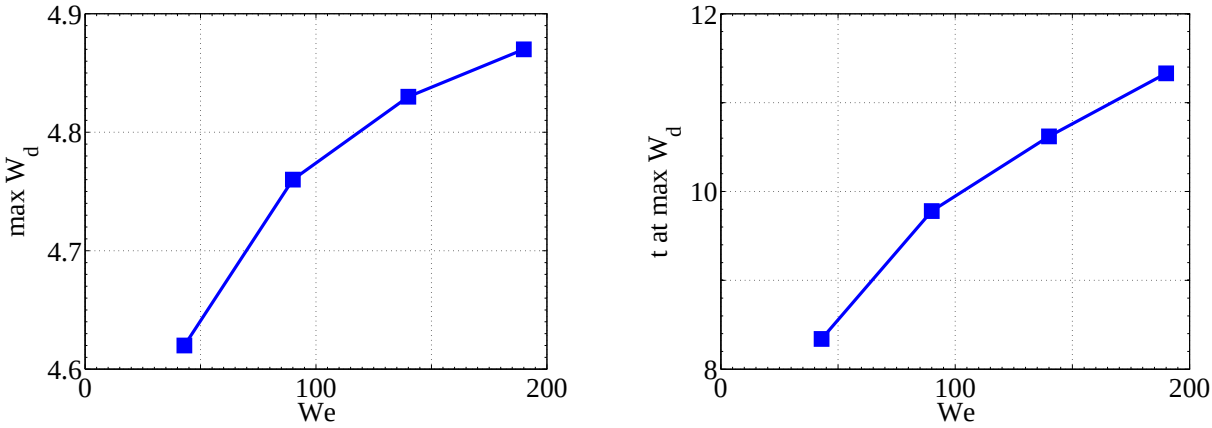

Figure 5.6: Maximal wetting diameter (left) and the time to attain it (right) for different Weber number with fixed $Re = 2079$ for a liquid droplet.

5.3 Influence of the solid Peclet number

In this section we study the influence of the solid Peclet number on the flow dynamics and on the heat transfer. We consider five variants (i) $Pe_S = 50$, (ii) $Pe_S = 100$, (iii) $Pe_S = 250$, (iv) $Pe_S = 350$ and (v) $Pe_S = 400$ by varying the heat conductivity of the solid. Further, we use fixed dimensionless numbers $Re = 2079$, $Fr = 179$, $We = 43$, $Bi = 0.000058$, $Pe_F = 10$. The fluid flow indirectly depends on the temperature thorough

the surface tension. A change in the local surface temperature T on the free surface induces Marangoni convection. However, the surface temperature variation is not high in all variants. Thus, the flow dynamics is very similar in all five variants of the solid Peclet number, see the wetting diameter and the dynamic contact angle over time in Figure 5.7.

Next, the computationally obtained heat flow (Q_h) and the total heat (sum over all time intervals) across the liquid-solid interface in all five variants over time are presented in Figure 5.8. Though, the wetting area is same in all variants, the heat flow varies. The heat flow is more in the small solid Peclet number case (Var i), whereas heat flow is less in the large solid Peclet number case (Var v). It is interesting to note that the heat flow is same in all five variants when the wetting diameter is large, say around the dimensionless time $t = 9$, see Figure 5.8. During the recoiling, we can see the reverse effect, that is, the heat flow is less in the small solid Peclet number case (Var i), and it approaches to zero faster than other variants. This behaviour can clearly be seen in the total heat, Figure 5.8 (right), where there is almost no variation in the total heat of Variant (i) after the dimensionless time $t = 10$.

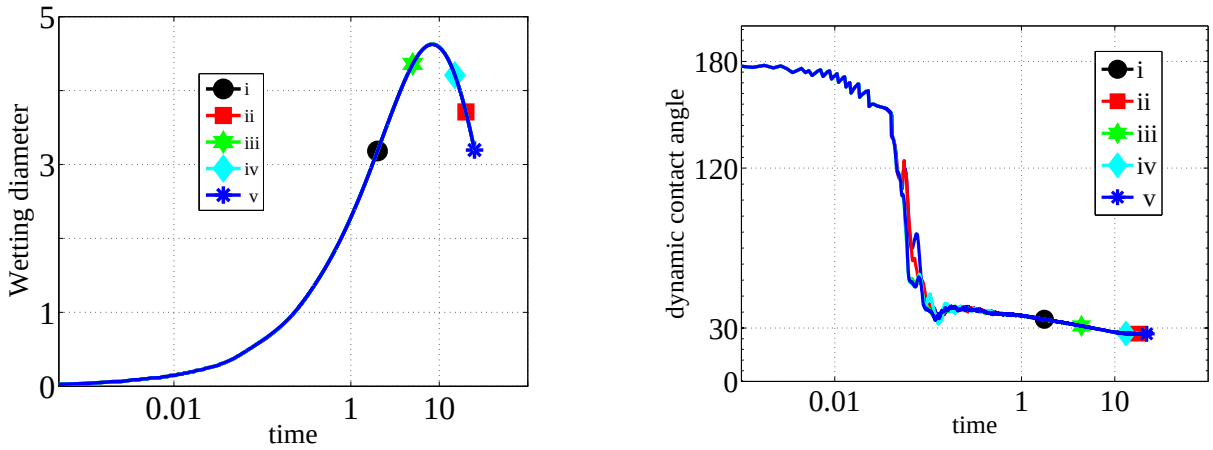

Figure 5.7: Wetting diameter (left) and the dynamic contact angle (right) of a liquid droplet with $\theta_e = 30°$, $Re = 2079$, $We = 43$ and $Fr = 179$ and different Peclet number (i) $Pe_S = 50$, (ii) $Pe_S = 100$, (iii) $Pe_S = 250$, (iv) $Pe_S = 350$, (v) $Pe_S = 400$.

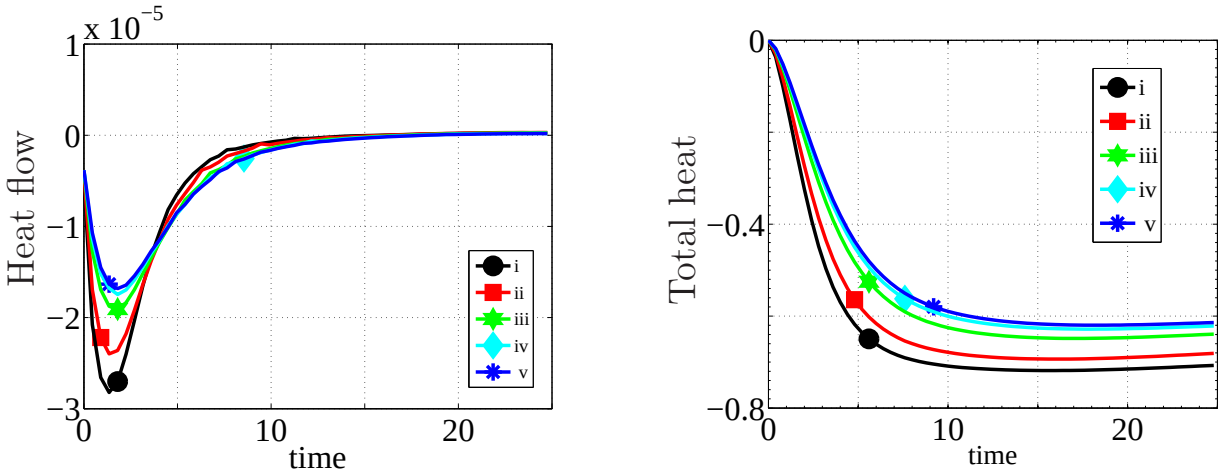

Figure 5.8: Heat flow (left) and total heat flow (right) of a liquid solid interface with $\theta_e = 30°$, $Re = 2079$, $We = 43$ and $Fr = 179$, and different Peclet number (i) $Pe_S = 50$, (ii) $Pe_S = 100$, (iii) $Pe_S = 250$, (iv) $Pe_S = 350$, (v) $Pe_S = 400$.

5.4 Influence of droplet diameter and the heat transfer

We next study the influence of the droplet diameter on the flow dynamics, and thus we consider an impinging droplet with three different diameters. A liquid droplet with (i) $d_0 = 3 \times 10^{-3}$m, (ii) $d_0 = 0.3 \times 10^{-3}$m, (iii) $d_0 = 0.03 \times 10^{-3}$m are considered. The droplet impact velocity is assumed to be $u_{imp} = 2.5$ m/s. We assume that $T_{F,0} = 300°$K, $T_{S,0} = 700°$K, $T_\infty = 298°$K, $T_{ref} = 323°$K in all test cases. Even though the considered initial temperature in the solid substrate may be above the Leidenfrost temperature, we have not incorporated the Leidenfrost effect in our model, and considered it only as a numerical test case. Using the characteristic length L $= r_0$, the following dimensionless numbers have been obtained:

- (i) $Re = 3750$, $We = 128$, $Fr = 425$, $Bi = 6.4 \times 10^{-7}$
- (ii) $Re = 375$, $We = 13$, $Fr = 4251$, $Bi = 6.4 \times 10^{-6}$
- (iii) $Re = 37$, $We = 1$, $Fr = 42517$, $Bi = 6.4 \times 10^{-5}$

The computationally obtained wetting diameter over time in all three cases are presented in Figure 5.9 (left). For a large value of droplet diameter, the maximal wetting diameter is expected to become larger. This behavior can clearly be seen in Figure 5.9. Due to small droplet diameter

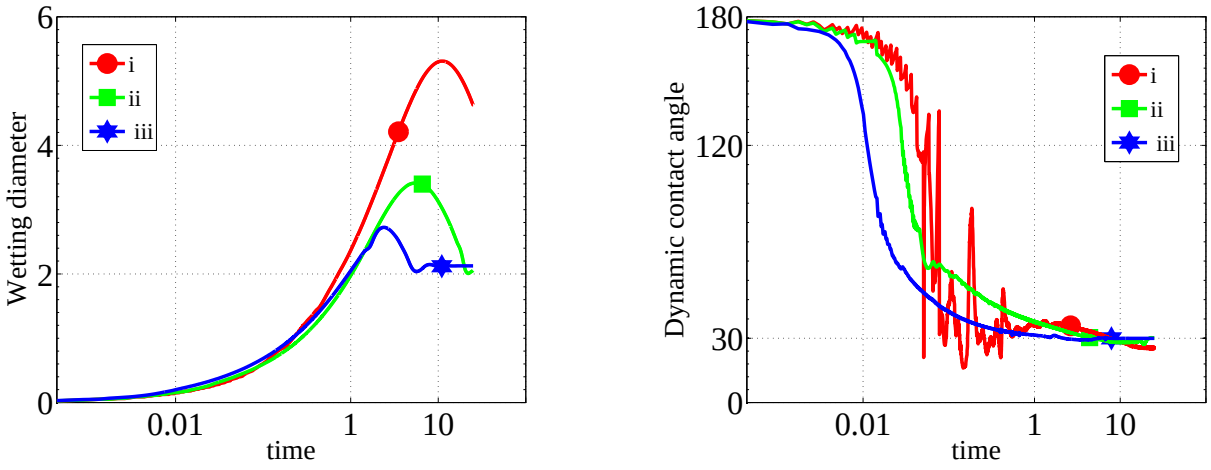

Figure 5.9: Wetting diameter (left) and the dynamic contact angle (right)of the droplet diameter (i) $d_0 = 3 \times 10^{-3}$m, (ii) $d_0 = 0.3 \times 10^{-3}$m, (iii) $d_0 = 0.03 \times 10^{-3}$ m.

in the case (iii), the deformation of the droplet is much smaller. The dynamic contact angle obtained in all three cases are presented in Figure 5.9 (right). The general behavior of the contact angle hysteresis is observed in all three cases.

Next, we present the heat flow

$$Q_n := \frac{1}{Pe_S} \int_{t^n}^{t^{n+1}} \int_{\partial\Omega_S} \frac{\partial T_S}{\partial \boldsymbol{\nu}_S} d\gamma \, dt$$

(see Section 4.3) and the total heat (sum of all Q_n) across the liquid-solid interface in Figure 5.10 for all three cases. As expected, the heat flow is large in the initial stage of the spreading. Since the wetting diameter is almost similar in all three cases at the initial stage (say until t=1), the heat flow is also similar in all cases at the initial stage of spreading. However, the heat flow is less in the smaller droplet diameter (case iii) during the recoiling stage (say after t=2) in comparison with the other two cases. Moreover, as expected the total heat is more when the droplet diameter is increased, see Figure 5.10 right.

We now compute the relative energy difference in the liquid and in the solid phases separately, by using the relation.

$$\text{energy difference in liquid} = \frac{\displaystyle\int_{\Omega_F(0)} T dx - \int_{\Omega_F(t)} T dx}{\displaystyle\int_{\Omega_F(0)} T dx}$$

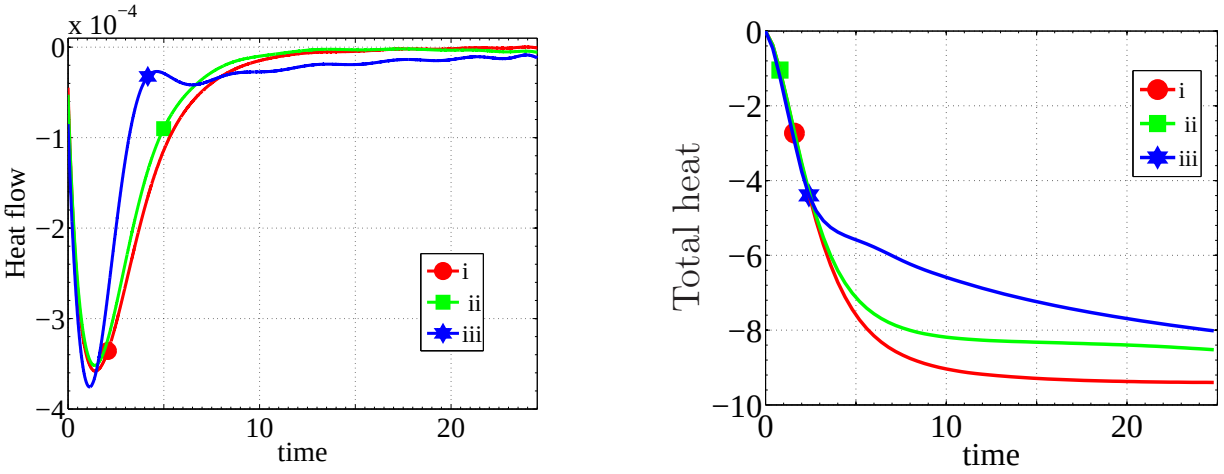

Figure 5.10: Heat flow (left) and the total heat (right) of a liquid droplet of size (i) $d_0 = 3 \times 10^{-3}$m, (ii) $d_0 = 0.3 \times 10^{-3}$ m, (iii) $d_0 = 0.03 \times 10^{-3}$ m.

$$\text{energy difference in solid} = \frac{\int_{\Omega_S(0)} T dx - \int_{\Omega_S(t)} T dx}{\int_{\Omega_S(0)} T dx}$$

The temperature in the droplet starts to increase when the droplet starts to spread, whereas the temperature in the solid phase starts to decrease, see Figure 5.11. Since the wetting diameter in the case (i) is large due to large droplet size, the droplet absorb more heat from the solid phase. It induces large relative heat differences in the solid phases, see Figure 5.11 (right). In the smaller droplet diameter case (iii), the total heat is less due to small wetting diameter, and thus the heat difference in both the liquid and the solid phases are small, see Figure 5.11.

5.5 Influence of Biot number

In this section we study the influence of the Biot number on the heat flow. We consider a droplet of diameter $d_0 = 3.0 \times 10^{-3}$ m. Further, the following material parameters are used: the density $\rho = 1000$ kg/m^3, the dynamic viscosity $\mu = 0.001$ N s/m^2, the surface tension $\sigma = 0.073$ N/m, the equilibrium contact angle $\theta_e = 30°$. Also, we assume that $u_{imp} = 2.5$ m/s, $T_F = 300°$K, $T_S = 700°$K, $T_\infty = 298°$K, $T_{ref} = 323°$K (temperature of the fluid surface, the solid surface, the atmospheric and the reference, respectively). Using L=r_0 as a characteristic length we get $Re = 3750$, Fr

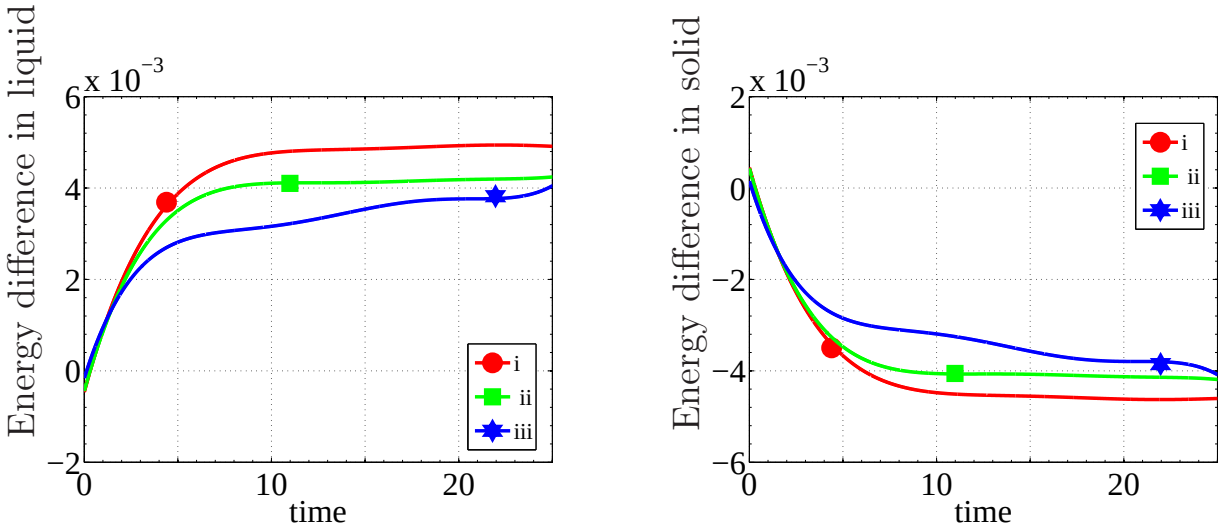

Figure 5.11: Energy difference in liquid (left) and solid (right) domain (i) $d_0 = 3\times10^{-3}$m, (ii) $d_0 = 0.3\times10^{-3}$ m, (iii) $d_0 = 0.03\times10^{-3}$ m.

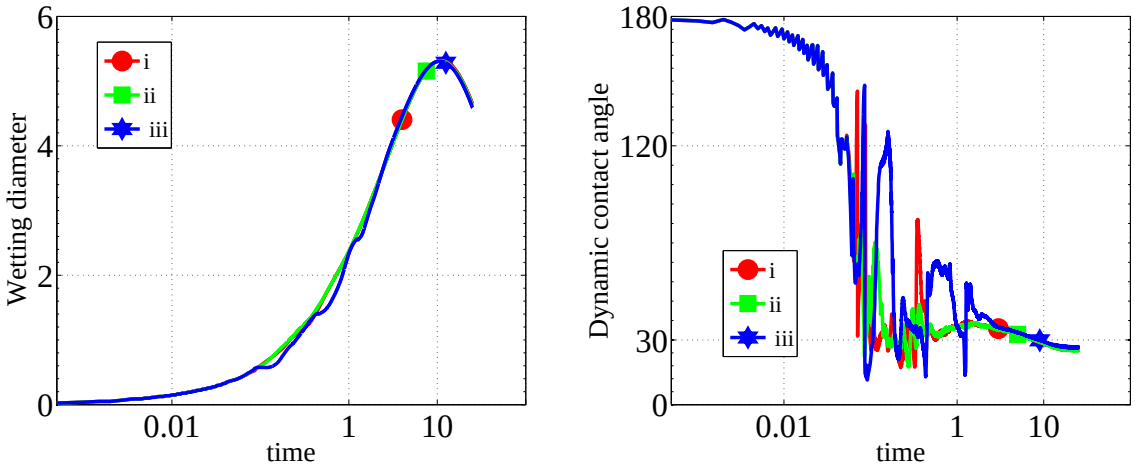

Figure 5.12: Wetting diameter (left) and the dynamic contact angle (right) of a liquid droplet with $\theta_e = 30°$, $Re = 3750$, $We = 128$, $Fr = 425$, impinging on a hot solid surface. Variants of Biot number (i) $Bi = 0.001$, (ii) $Bi = 0.1$, (iii) $Bi = 1$.

$= 425$, $We = 128$, $Pe_F = 10$, $Pe_S = 100$. In this study, we consider three variants: (i) $Bi = 0.001$, (ii) $Bi = 0.1$ and (iii) $Bi = 1$. The obtained wetting diameter and the dynamic contact angle over time for all three variants are presented in Figure 5.12. Though the flow dynamics is similar in first two variants, there are some oscillations in the dynamic contact angle of the Variant (iii). Recall that the Biot number controls the heat flow across the free surface, that is, a large value of Biot number induces

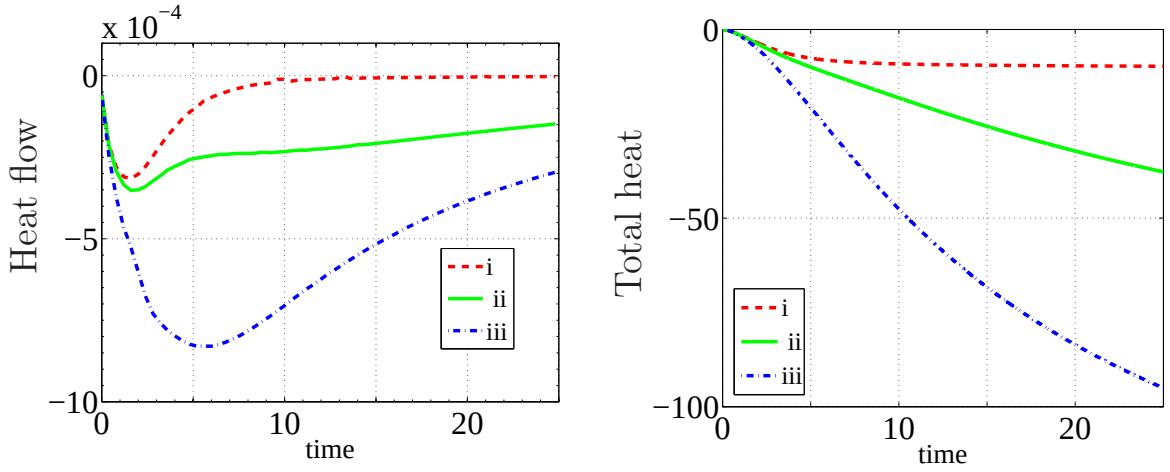

Figure 5.13: Influence of Biot number on the heat flow (left) and on the total heat (right) with $Re = 3750$, $We = 128$, $Fr = 425$ (i) $Bi = 0.001$, (ii) $Bi = 0.1$, (iii) $Bi = 1$.

more heat flow. Since we use the same liquid Peclet number in all three variants, the temperature on the free surface will be less in the large Biot number case (Var iii) in comparison with the Var (i). Therefore, the surface tension force will be large in Var (iii), see the relation 2.6, and it induces more rolling motion while spreading.

Next, the obtained heat flow and the total heat across the liquid-solid interface over time are presented in Figure 5.13. As expected, the heat flow is large in the high Biot number case (Var iii). The heat flow in the variant (i) approaches zero when the droplet attains it maximum wetting diameter, whereas the heat transfer from the solid phase to the liquid phase occurs even during the recoiling stage in the variant (iii), see Figure 5.13.

5.6 Influence of initial temperature on solid domain

In this study, we consider the following three variants (i) $T_{S,0} = 500°\text{K}$, (ii) $T_{S,0} = 600°\text{K}$, (iii) $T_{S,0} = 700°\text{K}$ for different Reynolds number. The computationally obtained wetting diameter and dynamic contact angle over time for all these variants are presented in Figure 5.14.

We now study the influence of the initial solid temperature for different droplet sizes as in the previous section. We consider the previous three cases: (A) $d_0 = 0.03 \times 10^{-3}$ m, (B) $d_0 = 0.3 \times 10^{-3}$ m and (C) $d_0 = 3 \times 10^{-3}$ m with $T_{S,0} = 500°\text{K}$, $T_{S,0} = 600°\text{K}$ and $T_{S,0} = 700°\text{K}$. Further,

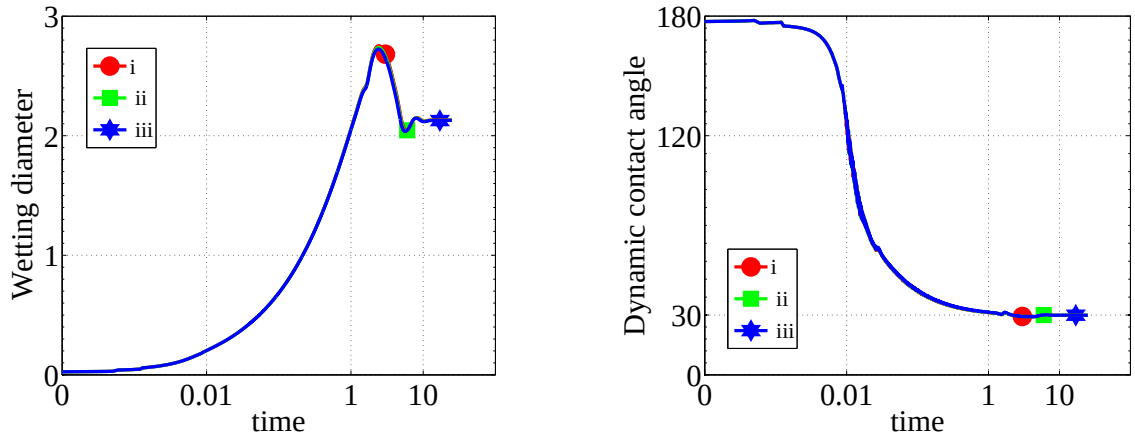

Figure 5.14: Wetting diameter (left) and dynamic contact angle(right) for $Re = 37$. (i) $T_{S,0} = 500°\text{K}$, (ii) $T_{S,0} = 600°\text{K}$, (iii) $T_{S,0} = 700°\text{K}$.

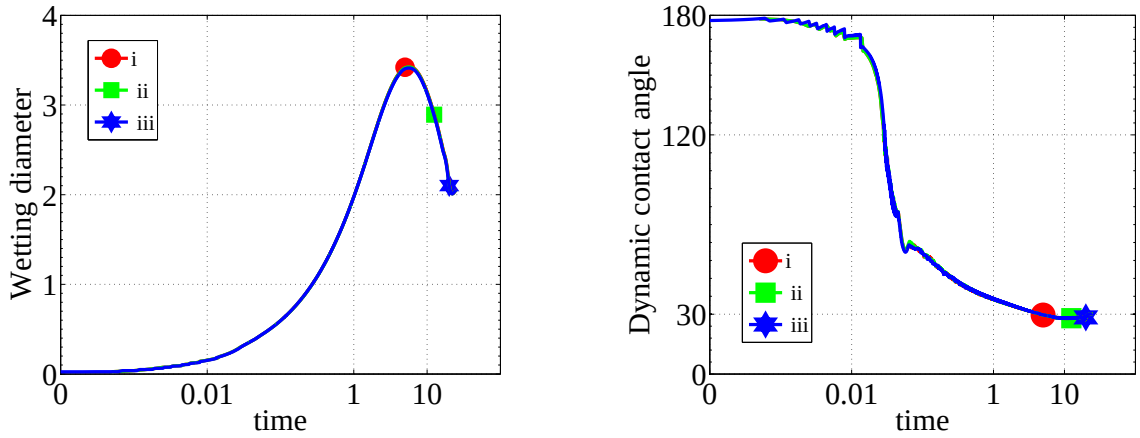

Figure 5.15: Wetting diameter (left) and dynamic contact angle(right) for $Re = 375$. (i) $T_{S,0} = 500°\text{K}$, (ii) $T_{S,0} = 600°\text{K}$, (iii) $T_{S,0} = 700°\text{K}$.

the equilibrium contact angle $\theta_e = 30°$ is used in all cases. The values of the material parameters such as the density, the dynamic viscosity and the surface tension are the same as in the previous section. Thus the dimensionless numbers are same as in the previous section.

The computationally obtained wetting diameter and the dynamic contact angle for the Case (A) ($d_0 = 0.03 \times 10^{-3}$ m) with different initial solid temperatures are presented in Figure 5.14. In this low Reynolds

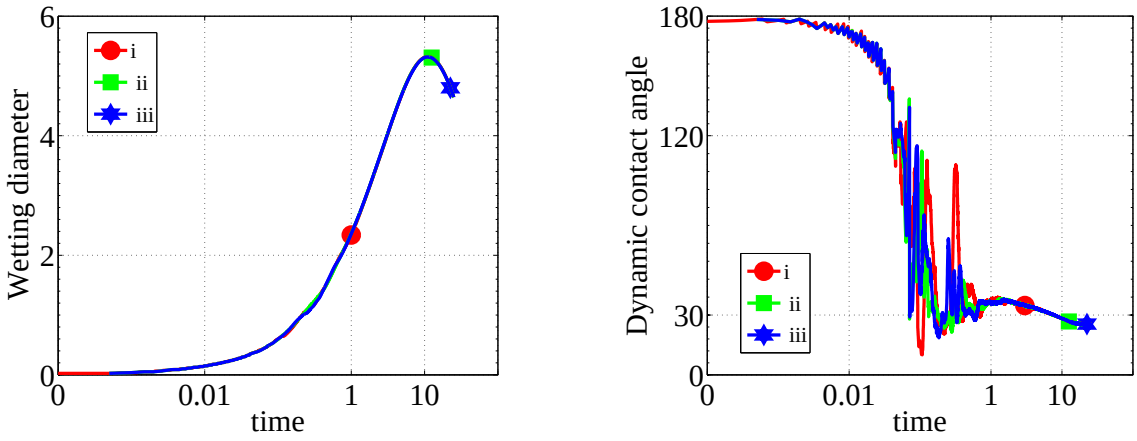

Figure 5.16: Wetting diameter (left) and dynamic contact angle(right) for $Re = 3750$. (i) $T_{S,0} = 500°\text{K}$, (ii) $T_{S,0} = 600°\text{K}$, (iii) $T_{S,0} = 700°\text{K}$.

number case, the initial solid temperature does not influence the flow dynamics. Also, there is no influence of the initial solid temperature on the flow dynamics of the droplet in the Case (B) ($d_0 = 0.3 \times 10^{-3}$ m), see Figure 5.15. However, the influence of the initial solid temperature on the dynamic contact angle can be seen in the high Reynolds number Case (C) ($d_0 = 3 \times 10^{-3}$ m), see Figure 5.16. Though there is no visible difference in the wetting diameter, there are oscillations in the dynamic contact angle even though the same equilibrium contact angle $\theta_e = 30°$ value is used in all variants in Figure 5.16. Since the droplet is very thin due to the large Reynolds number, the temperature gradient is large and thus the Marangoni effect could be a reason for this phenomenon. Next, the computationally obtained sequence of droplets at difference instances (dimensionless time) $t = 0.05,\ 0.5,\ 1.0,\ 7.5,\ 12.5$ for the Case (A) and Case (C) with $\theta_e = 30°$ are depicted in Figure 5.17. The colors in the images represent the temperature in the droplet and in the solid phase. The Reynolds number in the Case (A) is small and thus the wetting area is less in comparison with the Case (C), see Figure 5.17. Further the droplet is very thin in the high Reynolds number Case (C).

Finally, the heat flow from the solid surface to the liquid droplet

$$Q_n := \frac{1}{Pe_S} \int_{t^n}^{t^{n+1}} \int_{\partial\Omega_S} \frac{\partial T_S}{\partial \boldsymbol{\nu}_S} d\gamma \, dt$$

as a function of time is calculated to study the cooling effect. The detailed

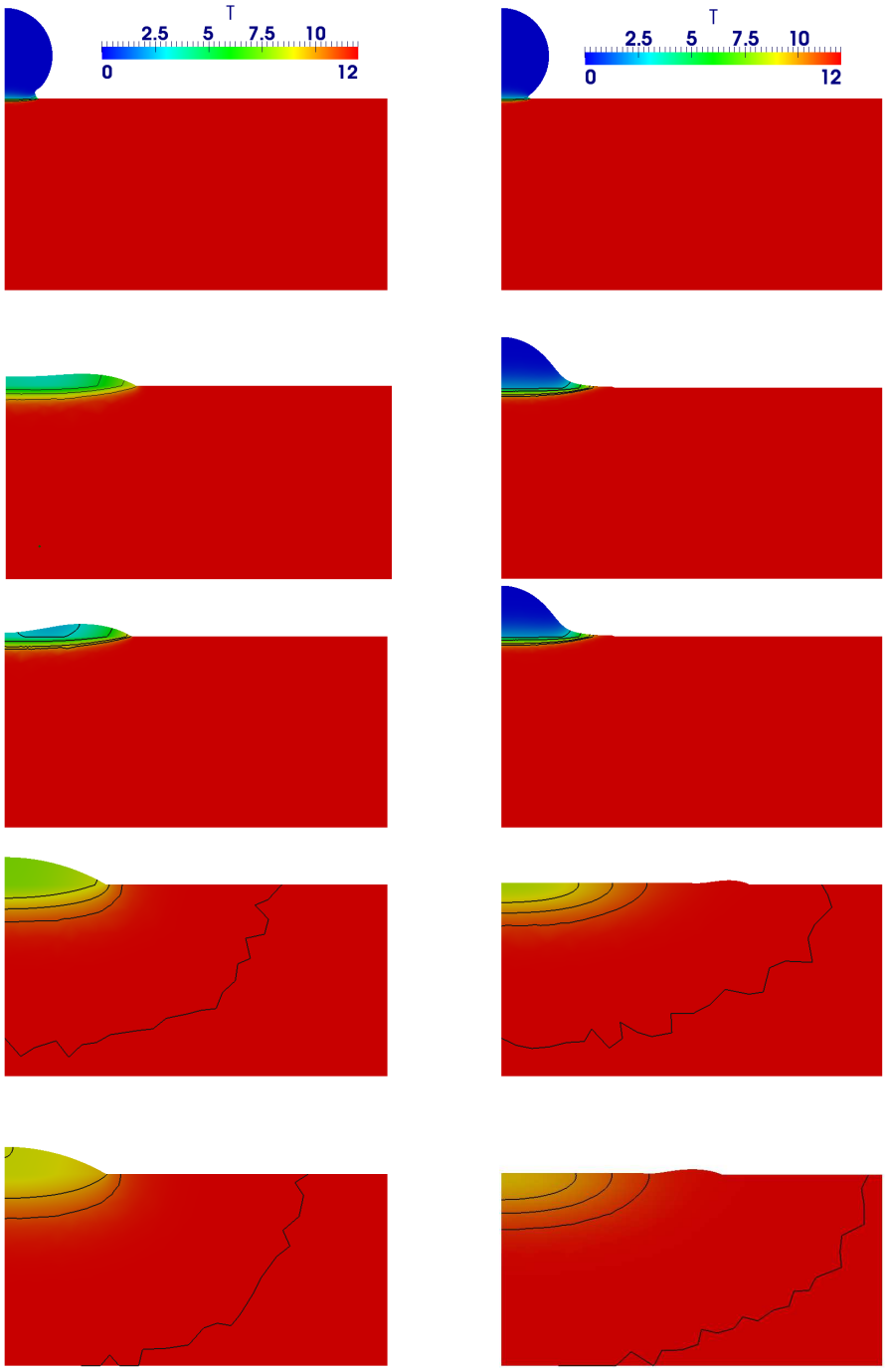

Figure 5.17: Sequence of images obtained in different simulations of a water droplet impinging on a hot solid surface with initial temperature $T_{S,0} = 600°\text{K}$, $Re = 37$ (left) and $Re = 3750$ (right). Timing from the top: $t = 0.05,\ 0.5,\ 1.0,\ 7.5,\ 12.5$.

description of the heat flow calculation has been provided in the Section 4.3. The obtained heat flow and the total heat (sum over all time intervals) across the liquid-solid interface over time for all three cases are presented

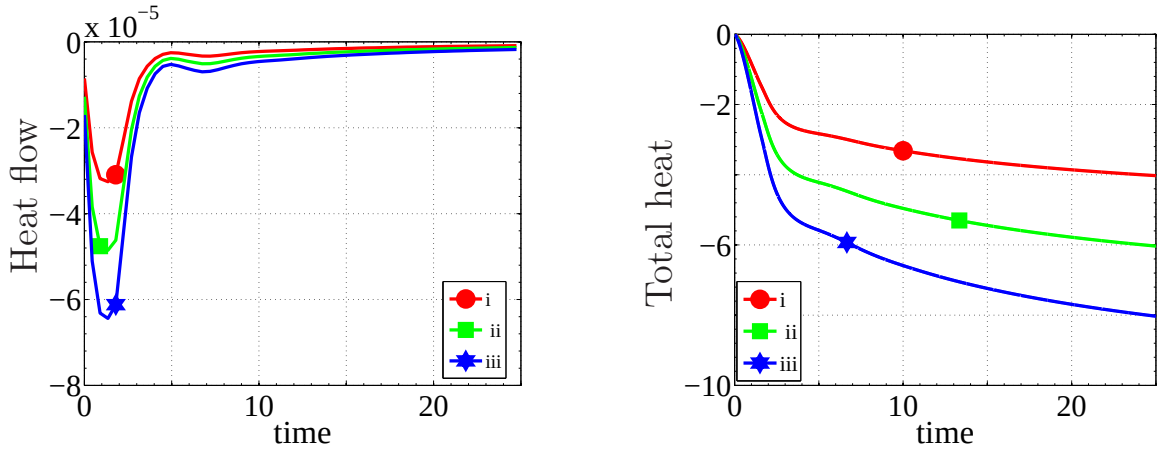

Figure 5.18: Heat flow (left) and the total heat (right) for $Re = 37$. (i) $T_{S,0}$ = 500°K, (ii) $T_{S,0}$ = 600°K, (iii) $T_{S,0}$ = 700°K.

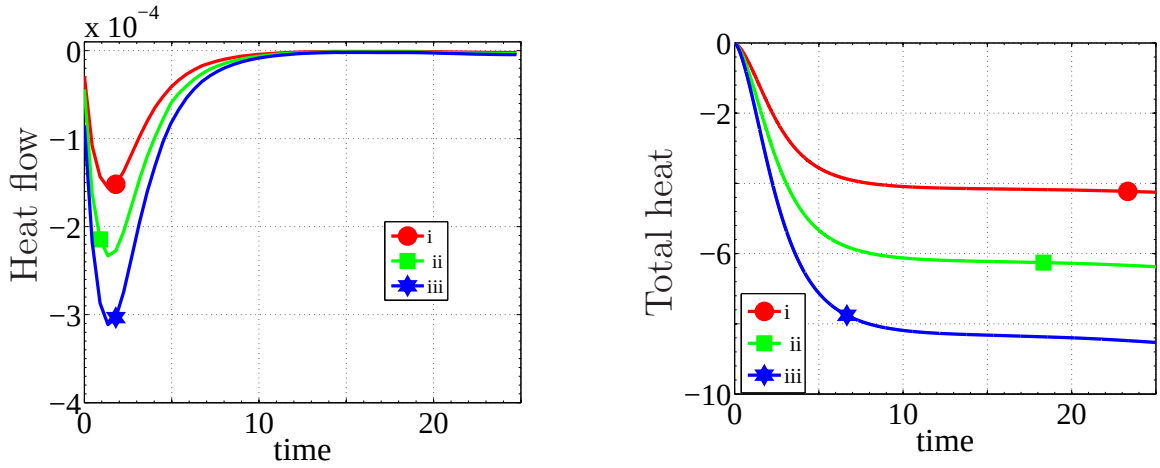

Figure 5.19: Heat flow (left) and the total heat (right) for $Re = 375$. (i) $T_{S,0}$ = 500°K, (ii) $T_{S,0}$ = 600°K, (iii) $T_{S,0}$ = 700°K.

in Figure 5.18, 5.19 and 5.20. As expected, the heat flow is less when the initial solid temperature is less and it is high in the large initial solid temperature variant. Overall the total heat is less in the small Reynalds number case, Figure 5.18 in comparison with the high Reynolds number case, Figure 5.20. This observation agrees with the physics that the larger droplet with maximum surface area cools the solid phase better than the smaller droplet with less wetting area.

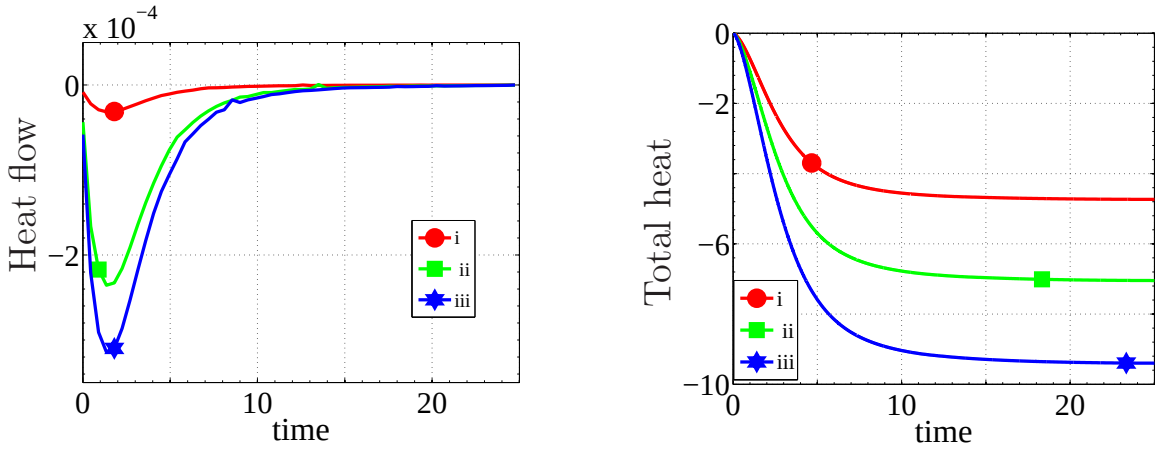

Figure 5.20: Heat flow (left) and the total heat (right) for $Re = 3750$. (i) $T_{S,0} = 500°\text{K}$, (ii) $T_{S,0} = 600°\text{K}$, (iii) $T_{S,0} = 700°\text{K}$.

5.7 Influence of contact angle

We study the influence of the Contact Angle for different droplet sizes on the flow dynamics of the droplet. In our study, we consider three droplet sizes: Case (A) $d_0 = 0.03 \times 10^{-3}$ m, Case (B) $d_0 = 0.3 \times 10^{-3}$ m and Case (C) $d_0 = 3 \times 10^{-3}$ m, and three contact angles $\theta_e = 30°$, $\theta_e = 60°$ and $\theta_e = 90°$. In all nine variants, the following material parameters are used: the density $\rho = 1000$ kg/m^3, the dynamic viscosity $\mu = 0.001$ N s/m^2 and the surface tension $\sigma = 0.073$ N/m. Also, we assume that $u_{imp} = 2.5$ m/s, $T_F = 298°\text{K}$, $T_S = 700°\text{K}$, $T_\infty = 298°\text{K}$, $T_{ref} = 323°\text{K}$ (temperature of the fluid surface, the solid surface, the atmospheric and the reference, respectively). Using L $= r_0$ and U $= u_{imp}$ as characteristic values, we get the following dimensionless numbers

- case (A) $Re = 37$, $We = 1$, $Fr = 42517$, $Bi = 6.4 \times 10^{-7}$
- case (B) $Re = 375$, $We = 13$, $Fr = 4251$, $Bi = 6.4 \times 10^{-6}$
- case (C) $Re = 3750$, $We = 128$, $Fr = 425$, $Bi = 6.4 \times 10^{-5}$

The computationally obtained wetting diameter and the dynamic contact angle from the Case (A) ($d_0 = 0.03 \times 10^{-3}$ m) for different equilibrium contact angle variants are presented in Figure 5.21. As expected, the maximum wetting diameter increases when the contact angle increases. Initially, the wetting diameter of all three contact angle variants are similar

for a short period of time. The wetting dynamics is completely different in the three variants in the later stage, say after time $t = 1$. For the large equilibrium contact angle, the droplet recoils quickly and oscillates around the equilibrium wetting length before reaching the steady state. However, the droplet reaches the steady state without much oscillation in the small equilibrium contact angle variant, see Figure 5.21. The dynamic contact angle in all three variants reach the equilibrium value almost after the dimensionless time $t = 1$, see Figure 5.21. It is clear from the picture that the prescribed equilibrium contact angle values in all three variants attain equilibrium value at the steady state after varying dynamically during the deformation. This shows the robustness of the proposed numerical scheme.

Next, the computationally obtained wetting diameter and the dynamic contact angle from the Case (B) $(d_0 = 0.3 \times 10^{-3}$ m) for different equilibrium contact angle variants are presented in Figure 5.22. Since the Reynolds number is large in this case, the obtained maximum wetting diameter in all variants of contact angle are large in comparison with the previous case (A). Also, the droplets did not attain the steady state till the end of the computation. Nevertheless, the influence of contact angle on the wetting diameter is similar as in the previous case. The dynamic contact angle in all three variants reaching the equilibrium value after a certain time, see Figure 5.22. Finally, the wetting diameter and the dynamic contact angle obtained for the Case (C) $(d_0 = 3\times10^{-3}$ m) for different equilibrium contact angle variants are presented in Figure 5.23. In this case, the maximum wetting diameter is even larger, as expected. Also, there is no oscillation of spreading and recoiling till the end of the computation.

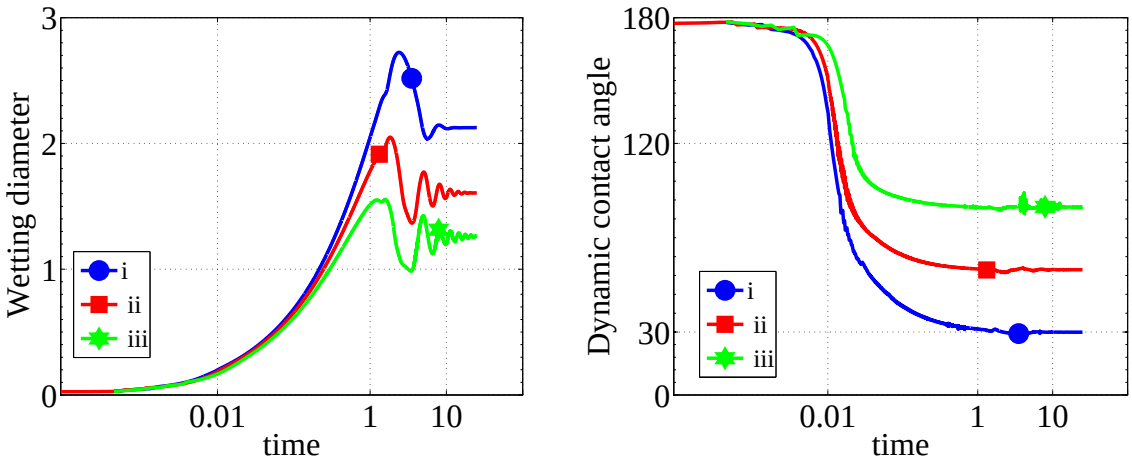

Figure 5.21: Wetting diameter (left) and the dynamic contact angle (right) for Re=37. (i) $\theta_e = 30°$, (ii) $\theta_e = 60°$, (iii) $\theta_e = 90°$.

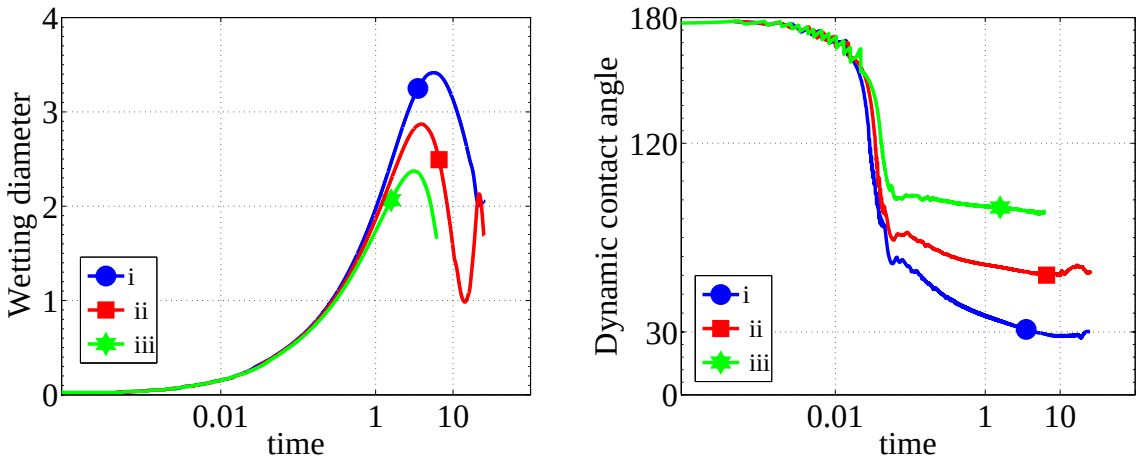

Figure 5.22: Wetting diameter (left) and the dynamic contact angle (right) for Re=375. (i) $\theta_e = 30°$, (ii) $\theta_e = 60°$, (iii) $\theta_e = 90°$.

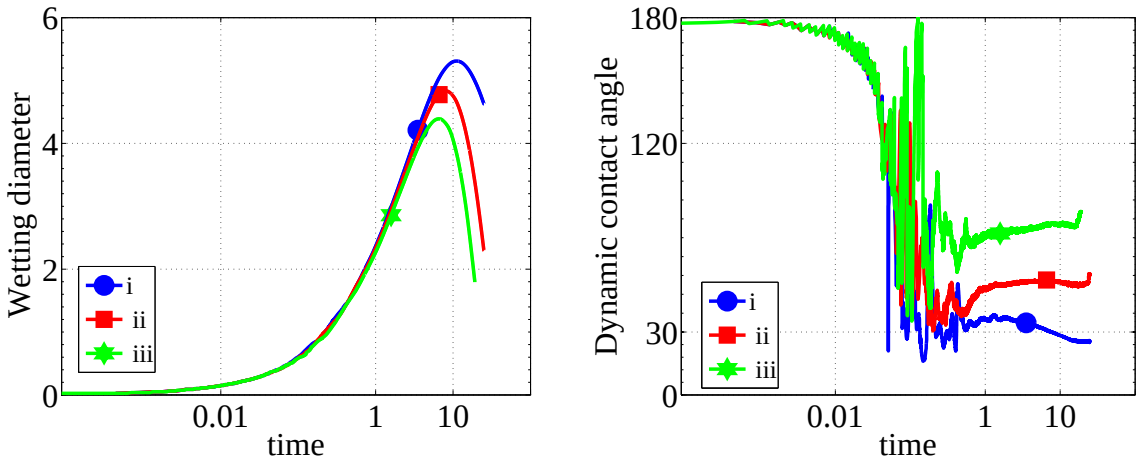

Figure 5.23: Wetting diameter (left) and the dynamic contact angle (right) for Re=3750. (i) $\theta_e = 30°$, (ii) $\theta_e = 60°$, (iii) $\theta_e = 90°$.

Further, more oscillations are observed in the obtained dynamic contact angles for different equilibrium contact angle variants in this case. However, the dynamic contact still reaching the prescribed equilibrium value in all three variants, see Figure 5.23.

Next, the computationally obtained sequence of droplets at difference instances (dimensionless time) $t = 0.05,\ 1.36,\ 6,\ 9,\ 12.5$ for the Case (A) with $\theta_e = 30°$ and $\theta_e = 90°$ are depicted in Figure 5.24. The colours in the images represent the temperature in the droplet and in the solid phase. In the $\theta_e = 30°$ variant (left), the entire droplet is almost hot at $t = 1.36$, however the droplet cools again at $t = 6$. This phenomenon is due to the fact that we allowed the heat flux from the free surface (non-zero Biot number) in all computations. As expected, the solid surface got more

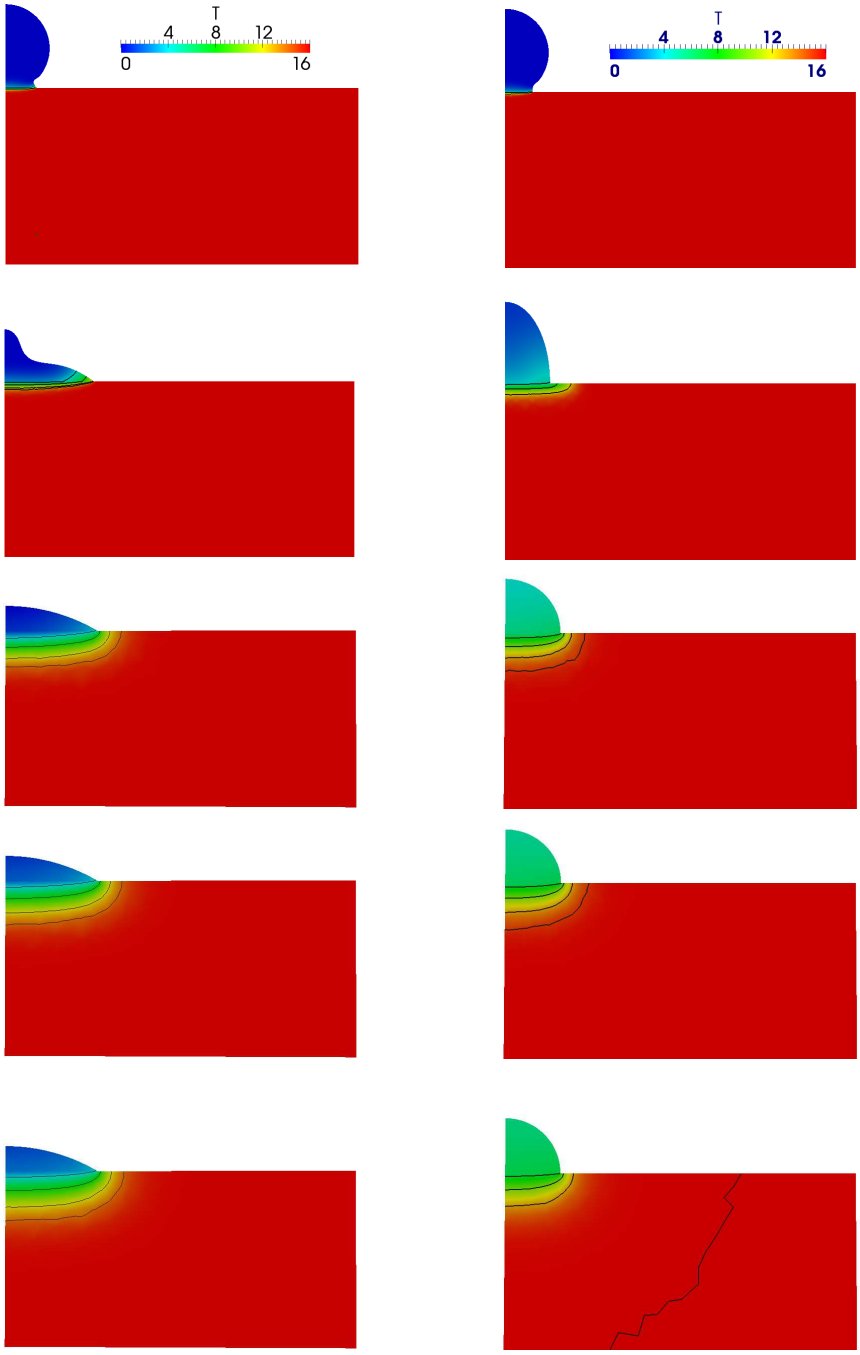

$\theta_e = 30°$ $\theta_e = 90°$

Figure 5.24: Sequence of images obtained in different simulations of a liquid droplet impinging on a hot solid surface with $Re = 37$, $We = 1$, $Fr = 42517$ (i) $\theta_e = 30°$, (ii) $\theta_e = 90°$. Timing from the top: $t = 0.05,\ 1.36,\ 6,\ 9,\ 12.5$.

cooled in $\theta_e = 30°$ variant (left) in comparison with the $\theta_e = 90°$ variant (right) as the wetting area is less in the later variant, see Figure 5.24 at the end time.

6 Summary

In this thesis, modeling and simulations of a non-isothermal liquid droplet impinging on a horizontal hot substrate are presented. The fluid flow in the droplet is described by the time dependent incompressible Navier–Stokes equations, whereas the temperature in the droplet and in the solid substrate is described by the energy equation.

The arbitrary Lagrangian–Eulerian (ALE) method is used to handle the time-dependent domain. In ALE approach, the jumps in the material properties are handled easily, since the computational mesh resolves the free surface and the liquid–solid interface. The contact angle at the moving contact line is included in the weak formulation of the model using the Laplace-Beltrami operator technique for the curvature term. Further, the curvature term is treated semi implicitly which is an advantage of using the Laplace-Beltrami operator technique. We used a second–order inf–sup stable finite element approximations for the velocity and pressure. In particular, we used the continuous, piecewise quadratic functions enriched with cubic bubble functions for the velocity and the discontinuous, piecewise linear functions for the pressure to obtain a good mass conservation. Further, an efficient algorithm is implemented to handle the rolling motion of the droplet during spreading. Moreover, a special algorithm for calculating the heat flow from the solid phase into the liquid phase is implemented. Also, the three–dimensional weak forms have been reformulated on a 3D-axisymmetric geometry with the assumption that the droplet deformation is axisymmetric. It allows to reduce the space dimension by one and also reduces the computational costs drastically.

Simulations of droplet impinging on a hot substrate for many test cases have been performed. In particular, the influence of different dimensionless (Reynolds, Weber, Peclet, and Biot) numbers on the flow dynamics and the heat transfer, the wetting diameter, the dynamics contact angle, the maximum wetting diameter and on the heat flow and total heat are studied. The maximum mass and energy fluctuations in all computations is less than 1 %, and this show the accuracy of the proposed numerical scheme.

Bibliography

[1] E. Bänsch. *Numerical methods for the instationary Navier-Stokes equations with a free capillary surface.* Habilitationsschrift, Albert-Ludwigs-Universität, Freiburg i. Br., 1998.

[2] M. Behr and F. Abraham. Free-surface flow simulations in the presence of inclined walls. *Comp. Meth. in App. Mech. and Engg*, 191(47-48):5467–5483, 2002.

[3] C. Bernardi, M. Dauge, Y. Maday, and M. Azaïez. *Spectral methods for axisymmetric domains.* Series in applied mathematics. Gauthier-Villars, 1999.

[4] C. Bernardi, Y. Maday, and A. T. Patera. A new nonconforming approach to domain decomposition: The mortar element method. *Nonlinear partial differential equations and their applications: Collège de France seminar*, 299:13–51, 1994.

[5] J. U. Brackbill, D. B. Kothe, and C. Zemach. A continuum method for modeling surface tension. *J. Comput. Phys.*, 100:335–354, 1992.

[6] A.M. Briones, J. S. Ervin, S. A. Putnam, L. W. Byrd, and L. Gschwender. Micrometer-sized water droplet impingement dynamics and evaporation on a flat dry surface. *Langmuir*, 26(16):13272–13286, 2010.

[7] M. O. Bristeau, R. Glowinski, and J. Periaux. Numerical methods for the Navier-Stokes equations. Application to the simulation of compressible and incompressible flows. *Comp. Phys.*, 6:73–188, 1987.

[8] P. G. Ciarlet. Basic error estimates for elliptic problems. In P. G. Ciarlet and J. L. Lions, editors, *Handbook of numerical analysis II*, pages 19–351. North-Holland, Amsterdam - New York - Oxford - Tokyo, 1991.

[9] R. G. Cox. The dynamics of the spreading of liquids on a solid surface. Part 1. Viscous flow. *Journal of Fluid Mechanics*, 168:169–194, 1986.

[10] M. Crouzeix and P.-A. Raviart. Conforming and nonconforming finite element methods for solving the stationary Stokes equations I. *R.A.I.R.O. Anal. Numér.*, 7:33–76, 1973.

[11] F.Brezzi D.Boffi and M.Fortin. *Mixed Finite Element Methods and applications*. Springer Series in Computational Mathematics. Springer, Berlin-Heidelberg, 2013.

[12] J. Donéa. Arbitrary Lagrangian-Eulerian finite element methods. In T. Belytschko and T. R. J. Hughes, editors, *Computational methods for transient analysis*, pages 473–516. Elsevier scientific publishing co., Amsterdam, 1983.

[13] V. Dugas, J. Broutin, and E. Souteyrand. Droplet evaporation study applied to dna chip manufacturing. *Langmuir*, 21(20):9130–9136, 2005.

[14] G. Dziuk. Finite elements for the Beltrami operator on arbitrary surfaces. In S. Hildebrandt and R. Leis, editors, *Partial differential equations and calculus of variations*, pages 142–155. Springer, Berlin, 1988.

[15] G. Dziuk. An algorithm for evolutionary surfaces. *Numer. Math.*, 58:603–611, 1991.

[16] G. Dziuk and Charles M. Elliott. Finite element methods for surface pdes. *Acta Numerica*, 22:289–396, 2013.

[17] J. Eggers and H. A. Stone. Characteristic lengths at moving contact lines for a perfectly wetting fluid: the influence of speed on the dynamic contact angle. *J. Fluid Mech.*, 505:309–321, 2004.

[18] H. Y. Erbil. Evaporation of pure liquid sessile and spherical suspended drops: a review. *Adv.Colloid Interface Science*, 170:67–86, 2012.

[19] M. Francois and W. Shyy. Computations of drop dynamics with the immersed boundary method, Part 1: Numerical algorithm and buoyancy-induced effect. *Numer. Heat Trans., Part B: Fund.*, 44(2):101–118, 2003.

[20] M. Francois and W. Shyy. Computations of drop dynamics with the immersed boundary method, Part 2: Drop impact and heat transfer. *Numer. Heat Trans., Part B: Fund.*, 44(2):119–143, 2003.

[21] H. Fujimoto and N. Hatta. Deformation and rebounding processes of a water droplet impinging on a flat surface above leidenfrost temperature. *J. Fluids Eng.*, 118:142–149, 1996.

[22] S. Ganesan. *Finite element methods on moving meshes for free surface and interface flows.* PhD Thesis, Otto-von-Guericke-Universität, Fakultät für Mathematik, Magdeburg, 2006. Published as book (ISBN 3-939665-06-1) by docupoint Verlag Magdeburg.

[23] S. Ganesan. On the dynamic contact angle in simulation of impinging droplets with sharp interface methods. *Microfluidics and Nanofluidics*, 14:615–625, 2013.

[24] S. Ganesan, G. Matthies, and L. Tobiska. On spurious velocities in incompressible flow problems with interfaces. *Comput. Methods Appl. Mech. Engrg.*, 196(7):1193–1202, 2007.

[25] S. Ganesan and L. Tobiska. Computations of flows with interfaces using arbitrary Lagrangian Eulerian method. *Proceedings of ECCOMAS CFD 2006, Egmond aan Zee, The Netherlands,*, ISBN 90-9020970-0, 2006.

[26] S. Ganesan and L. Tobiska. An accurate finite element scheme with moving meshes for computing 3D-axisymmetric interface flows. *Int. J. Numer. Methods Fluids*, 57(2):119–138, 2008.

[27] S. Ganesan and L. Tobiska. Modelling and simulation of moving contact line problems with wetting effects. *Comput. Visual. Sci.*, 12:329–336, 2009.

[28] S. Ganesan and L. Tobiska. Arbitrary Lagrangian–Eulerian finite-element method for computation of two-phase flows with soluble surfactants. *J. Comput. Phys.*, 231(9):3685–3702, 2012.

[29] S. V. Garimella. Advances in mesoscale thermal management technologies for microelectronics. *Microelectronics Journal*, 37:1165–1185, 2006.

[30] D. Gerlach, G. Tomar, G. Biswas, and F. Durst. Comparison of volume-of-fluid methods for surface tension-dominant two-phase flows. *Int. J. Heat and Mass Transfer*, 49(3-4):740–754, 2006.

[31] R. Ghafouri-Azar, S. Shakeri, S. Chandra, and J. Mostaghimi. Interactions between molten metal droplets impinging on a solid surface. *Int. J. Heat Mass Transfer*, 46(8):1395–1407, 2003.

[32] M. Giles, M. Larson, J. M. Levenstam, and E. Süli. Adaptive error control for finite element approximations of the lift and drag coefficients in viscous flow. Technical report na-76/06, Oxford University Computing Laboratory, 1997.

[33] V. Girault and P.-A. Raviart. *Finite Element Methods for Navier–Stokes equations*. Springer-Verlag, Berlin-Heidelberg-New York, 1986.

[34] S. Gross, V. Reichelt, and A. Reusken. A finite element based level set method for two-phase incompressible flows. IGPM Report 243, RWTH Aachen, 2004.

[35] S. Gross, V. Reichelt, and A. Reusken. A finite element based level set method for two-phase incompressible flows. *Comput. Visual. Sci.*, 9(4):239 – 257, 2006.

[36] S. Gross and A. Reusken. *Numerical methods for two–phase incompressible flows*. Springer-Verlag, Berlin Heidelberg, 2011.

[37] F. N. Hamada, M.Rosenzweig, K. Kang, S. R. Pulver, A. Ghezzi, T. J. Jegla, and P. A. Garrity. An internal thermal sensor controlling temperature preference in drosophila. *Nature*, 454:217–220, 2008.

[38] D. J. E. Harvie and D. F. Fletcher. A hydrodynamic and thermodynamic simulation of droplet impacts on hot surfaces. Part ii: validation and applications. *Int. J. Heat and Mass Transfer*, 44(14):2643–2659, 2001.

[39] C. W. Hirt, A. A. Amsden, and J. L. Cook. An arbitrary Lagrangian Eulerian computing method for all flow speeds. *J. Comput. Phys.*, 14(3):227–253. Reprinted in 135(2) (1997) 203–216., 1974.

[40] C.W. Hirt and B.D. Nichols. Volume of Fluid (VOF) method for the dynamics of free boundaries. *J. Comput. Phys.*, 39:201–225, 1981.

[41] L. M. Hocking. A moving fluid interface. Part 2. the removal of the force singularity by a slip flow. *Journal of Fluid Mechanics*, 79(2):209–229, 1977.

[42] C. Huh and L. E. Scriven. Hydrodynamic model of steady movement of a solid/liquid/fluid contact line. *J. Colloid Interface Sci.*, 35:85–101, 1971.

[43] D. Jacqmin. Calculation of two-phase navierstokes flows using phase-field modeling. *Journal of Computational Physics*, 155(1):96 – 127, 1999.

[44] V. John and A. Liakos. Time dependent flow across a step: the slip with friction boundary condition. *Int. J. Numer. Meth. Fluids*, 50:713–731, 2006.

[45] G. Karniadakis, A. Beskok, and N. Aluru. *Microflows and Nanoflows*. Springer, 2005.

[46] J. H. Kim, S. M. You, and S.U.S.Choi. Evaporative spray cooling of plain and microporous coated surfaces. *Int.J.Heat and mass transfer*, 47:3307–3315, 2004.

[47] E. Lauga, P.Brenner, and H. A. Stone. Microfluidics: The no-slip boundary condition. In J. Foss, C. Tropea, and A. Yarin, editors, *Handbook of experimental fluid dynamics*, page (to appear). Springer, New-York, 2005.

[48] G. Matthies. *Finite element methods for free boundary value problems with capillary surfaces*. Phd thesis, Otto-von-Guericke-Universität, Fakultät für Mathematik, Magdeburg, 2002.

[49] G. Matthies and L. Tobiska. The inf-sup condition for the mapped Q_k/P_{k-1}^{disc} element in arbitrary space dimensions. *Computing*, 69(2):119–139, 2002.

[50] M. Muradoglu and G. Tryggvason. A front-tracking method for computation of interfacial flows with soluble surfactants. *J. Comput. Phys.*, 227:2238–2262, 2008.

[51] P. Nithiarasu. An arbitrary Lagrangian Eulerian (ALE) formulation for free surface flows using the characteristic-based split (CBS) scheme. *Int. J. Numer. Methods Fluids*, 12:1415–1428, 2005.

[52] F. Nobile. *Numerical approximation of fluid-structure interaction problems with application to haemodynamics*. PhD thesis, École Polytechnique Fédérale de Lausanne, 2001.

[53] S. Osher and J. A. Sethian. Fronts propagating with curvature dependent speed: Algorithms based on Hamilton-Jacobi forumlations. *J. Comput. Phys.*, 79:12–49, 1988.

[54] J. Park and J. Moon. Control of colloidal particle deposit patterns within picoliter droplets ejected by ink-jet printing. *Langmuir*, 22(8):3506–3513, 2006.

[55] M. Pasandideh-Fard, R. Bhola, S. Chandra, and J. Mostaghimi. Deposition of tin droplets on a steel plate: simulations and experiments. *Int. J. Heat Mass Transfer*, 41:2929–2945, 1998.

[56] C. S. Peskin. Flow patterns around heart valves: A numerical method. *J. Comput. Phys.*, 10:252–271, 1972.

[57] C. S. Peskin. The immersed boundary method. *Acta Numerica*, pages 1–36, 2002.

[58] J. E. Pilliod and E. G. Puckett. Second-order accuarate volume-of-fluid algorithms for tracking material interfaces. *J. Comput. Phys.*, 169(2):708–759, 2001.

[59] J. E. Pilliod and E. G. Puckett. Second-order accuarate volume-of-fluid algorithms for tracking material interfaces. *J. Comput. Phys.*, 199(2):465–502, 2004.

[60] S. A. Putnam, A. M. Briones, L. W. Byrd, J. S. Ervin, M. S. Hanchak, A. White, and J. G. Jones. Microdroplet evaporation on superheated surfaces. *Int. J. Heat Mass Transfer*, 55(21–22):5793–5807, 2012.

[61] M. Renardy, Y. Renardy, and J. Li. Numerical simulation of moving contact line problems using a volume-of-fluid method. *J. Comput. Phys.*, 171:243–263, 2001.

[62] W.J. Rider and D.B. Kothe. Reconstructing volume tracking. *J. Comput. Phys.*, 141:112–152, 1998.

[63] V. Ruas. Mixed finite element methods with discontinuous pressures for axisymmetric stokes problem. *Z. Angew. Math. Mech.*, 83(4):249–264, 2003.

[64] M. Schena, D. Shalon, R. W. Davis, and P. O. Brown. Quantitative monitoring of gene expression pattern with a complementary dna microarray. *Science*, 270(5235):467–470, 1995.

[65] J. A. Sethian. *Level Set Methods*. Cambridge University Press, 1996.

[66] K. S. Sheth and C. Pozrikidis. Effects of inertia on the deformation of liquid drops in simple shear flow. *Comput. Fluids*, 24(2):101–119, 1995.

[67] Jonathan R. Shewchuk. Triangle: Engineering a 2D Quality Mesh Generator and Delaunay Triangulator. In Ming C. Lin and Dinesh Manocha, editors, *Applied Computational Geometry: Towards Geometric Engineering*, volume 1148 of *Lecture Notes in Computer Science*, pages 203–222. Springer-Verlag, May 1996. From the First ACM Workshop on Applied Computational Geometry.

[68] W. J. Silliman and L. E. Scriven. Separating flow near static contact line: Slip at wall and shape of a free surface. *J. Comput. Phys.*, 34:287–313, 1980.

[69] G. Strotos, M. Gavaises, A. Theodorakakos, and G. Bergeles. Numerical investigation of the cooling effectiveness of a droplet impinging on a heated surface. *Int. J. Heat Mass Transfer*, 51(19–20):4728–4742, 2008.

[70] G. Strotos, M. Gavaises, A. Theodorakakos, and G. Bergeles. Numerical investigation on the evaporation of droplets depositing on heated surfaces at low weber numbers. *Int. J. Heat Mass Transfer*, 51(7–8):1516–1529, 2008.

[71] M. Sussman and E. G. Puckett. A coupled level set and volume-of-fluid method for computing 3d axisymmetric incompressible two-phase flows. *J. Comput. Phys.*, 162:301–337, 2000.

[72] M. Sussman, P. Smereka, and S. Osher. A level set approach for computing solutions to incompressible two-phase flow. *J. Comput. Phys.*, 114(1):146–159, 1994.

[73] G. Tryggvason, B. Bunner, A. Esmaeeli, D. Juric, N. Al-Rawahi, W. Tauber, J. Han, S. Nas, and Y.-J. Jan. A front-tracking method for the computations of multiphase flow. *J. Comput. Phys.*, 169(2):708–759, 2001.

[74] Y. Tu, H Zhu, J. M. Frantz, M. E. Reding, K. C. Chan, and H. E. Ozkan. Evaporation and coverage area of pesticide droplets on hairy and waxy leaves. *Biosystems Engineering*, 104:324–334, 2009.

[75] S. Turek. *Efficient solvers for incompressible flow problems. An algorithmic and computational approach*. Springer-Verlag Berlin, 1999.

[76] S.O. Unverdi and G. Tryggvason. A front-tracking method for viscous, incompressible multi-fluid flows. *J. Comput. Phys.*, 100:25–37, 1992.

[77] E. B. Dussan V. The moving contact line: the slip boundary condition. *Journal of Fluid Mechanics*, 77(4):665–684, 1976.

[78] M. van Sint Annaland, N.G. Deen, and J.A.M. Kuipers. Numerical simulation of gas bubbles behaviour using a three-dimensional volume-of-fluid method. *Chem. Engg. Sci.*, 60(11):2999–3011, 2005.

[79] J. Wendelstorf, K.H.Spitzer, and R.Wendelstorf. Spray water cooling heat transfer at high temperature and liquid mass fluxes. *Int.J.Heat and mass transfer*, 51:4902–4910, 2008.

[80] F. Wilczek. Did the big bang boil? *Nature*, 443:637, 2006.

[81] L. S. Fan Y. Ge. Three-dimensional simulation of impingement of a liquid droplet on a flat surface in the leidenfrost regime. *Phys. Fluids*, 17:027104, 2005.

[82] L. S. Fan Y. Ge. 3-D modeling of the dynamics and heat transfer characteristics of subcooled droplet impact on a surface with film boiling. *Int. J. Heat Mass Transfer*, 49(21–22):4231–4249, 2006.

[83] J. Fukai Z. Zhao, D. Poulikakos. Heat transfer and fluid dynamics during the collision of a liquid droplet on a substrate. 1. Modeling. *Int. J. Heat Mass Transfer*, 39(13):2771–2789, 1996.